UNIVERSITY OF SOUTHERN QUEENSLAND

# Automatic non-destructive dimensional measurement of cotton plants in real-time by machine vision

A Dissertation submitted by

**Cheryl Louise McCarthy, B.Eng (Hons)**

for the award of

**Doctor of Philosophy**

March 2009

Copyright

by

Cheryl Louise McCarthy

2009

# Abstract

Pressure on water resources in Australia necessitates improved application of water to irrigated crops. Cotton is one of Australia's major crops, but is also a large water user. On-farm water savings can be achieved by irrigating via large mobile irrigation machines (LMIMs), which are capable of implementing deficit strategies and varying water application to 1 $m^2$ resolution. However, irrigation amounts are commonly held constant throughout a field despite differing water requirements for different areas of a crop due to spatial variability of soil, microclimate and crop properties.

This research has developed a non-destructive cotton plant dimensional measurement system, capable of mounting on a LMIM and streaming live crop measurement data to a variable-rate irrigation controller. The sensor is a vision system that measures the cotton plant attribute of internode length, i.e. the distance between main stem nodes (or branch junctions) on the plant's main stem, which is a significant indicator of plant water stress.

The vision system consisted of a Sony camcorder (deinterlaced image size 720 $\times$ 288 pixels) mounted behind a transparent panel that moved continuously through the crop canopy. The camera and transparent panel were embodied in a contoured fibreglass camera enclosure (dimensions 535 mm $\times$ 555 mm $\times$ 270 mm wide) that utilised the natural flexibility of the growing foliage to firstly contact the plant, such that the top five nodes of the plant were in front of the transparent panel, and then smoothly and non-destructively guide the plant under the curved bottom surface of the enclosure. By

forcing the plant into a fixed object plane (the transparent panel), reliable geometric measurement was possible without the use of stereo vision. Motorisation of the camera enclosure enabled conveyance both across and along the crop rows using an in-field chassis.

A custom image processing algorithm was developed to automatically extract internode distance from the images collected by the camera, and comprised both single frame and sequential-frame analyses. Single frame processing consisted of detecting lines corresponding to branches and calculating the intersection of the detected lines with the main stem to estimate candidate node positions. Calculation of the 'vesselness' function for each pixel using the Hessian matrix eigenvalues determined whether the pixel was likely to belong to a stem (i.e. a curvilinear structure). Large areas of connected high-vesselness pixels were identified as branches. For each branch area, centre points were determined by solving the second order Taylor polynomial in the direction perpendicular to the line direction. The main stem was estimated with a linear Hough transform on the branch centre points within the image. Lines were then fitted to the centre points of other branch segments using the hop-along line-fitting algorithm and these lines were selectively projected to the main stem to estimate candidate node positions. The automatically-identified node positions corresponded to manual position measurements made on the source images.

Within individual images, leaf edges were erroneously detected as candidate nodes ('false positives') and contributed up to 22% of the total number of detected candidate nodes. However, a grouping algorithm based on a Delaunay Triangulation mesh of the candidate node positions was used to remove the largely-random false positives and to create accurate candidate node trajectories. The internode distance measurement was then calculated as the maximum value between detected trajectories which corresponded to when the plant was closest to the transparent panel.

From 168 video sequences of fourteen plants, 95 internode lengths were automatically detected at an average rate of one internode length per 1.75 plants for across row measurement, and one internode length per 3.3 m for along row measurement. Comparison

with manually-measured internode lengths yielded a correlation coefficient of 0.86 for the automatic measurements and an average standard error in measurement of 3.0 mm with almost zero measurement bias.

The second and third internode distances were most commonly detected by the vision system. The most measurements were obtained with the camera facing north or south, on a partially cloudy day in which the sunlight was diffused. Heliotropic effects and overexposed image background reduced image quality when the camera faced east or west. Night time images, captured with 850 nm LED illumination, provided as many measurements as the corresponding daytime measurements. Along row camera enclosure speeds up to 0.20 m/s yielded internode lengths using the current image processing algorithms and hardware. Calculations based on field programmable gate array (FPGA) implementation indicated an overall algorithm run-time of 46 ms per frame which is suitable for real-time application.

It is concluded that field measurement of cotton plant internode length is possible using a moving, plant-contacting camera enclosure; that the presence of occlusions and other foliage edges can be overcome by analysing the sequence of images; and that real-time in-field operation is achievable.

# Certification of Thesis

I certify that the ideas, experimental work, results, analyses, software and conclusions reported in this dissertation are entirely my own effort, except where otherwise acknowledged. I also certify that the work is original and has not been previously submitted for any other award, except where otherwise acknowledged.

| | |
|---|---|
| Signature of Candidate | Date |

ENDORSEMENT

| | |
|---|---|
| Signature of Supervisors | Date |

# Acknowledgments

Thank you to my family for their support throughout my degree. The guidance of my project supervisors, Associate Professor Nigel Hancock and Professor Steven Raine, was invaluable.

I appreciate the support from FoES and NCEA staff including Professor John Billingsley, Mark Phythian and Associate Professor Armando Apan. Thank you to the Queensland cotton farms 'Macquarie Downs' and 'Adelong' for providing field trial sites and to agronomist Dr Simon White for assistance in collecting field data.

The experience of meeting mechatronic and machine vision researchers in the USA, at the University of Illinois at Urbana-Champaign, University of Nebraska-Lincoln, Iowa State University at Ames, and Ohio State University at Wooster, was invaluable to expanding my perspectives on global agriculture and machine vision systems.

Thank you to the Australian Research Council and to the Cooperative Research Centre for Irrigation Futures for funding support.

Cheryl McCarthy

# List of Publications

The following articles have been published or submitted for publication about the research contained within this dissertation.

1. MCCARTHY, C. L., Hancock, N. H. and Raine, S. R. (2006) A preliminary evaluation of machine vision sensing of cotton nodes for automated irrigation control. In: Irrigation Association of Australia National Conference, 9-11 May, Brisbane, pp. 81–82.

2. MCCARTHY, C. L. (2007a) When and where to water? Ask the plant, automatically. Irrigation Australia 23(3):30.

3. McCARTHY, C. L. (inventor) (2007b) Methods and apparatus for measuring geometrical parameters of foliage. IP Australia Patent 2007201452, filed 03 April 2007; published 18 October 2007; expiry 03 April 2027.

4. MCCARTHY, C. L., Hancock, N. H. and Raine, S. R. (2007a) On-the-go machine vision sensing of cotton plant geometric parameters: first results. In: Billingsley, J., and Bradbeer, R. (eds.) Mechatronics and Machine Vision in Practice, New York: Springer-Verlag, pp. 305–312. Originally presented in 13th International Conference on Mechatronics and Machine Vision in Practice, 5-7 December 2006, Toowoomba, Australia.

5. MCCARTHY, C. L., Hancock, N. H. and Raine, S. R. (2007b) Automated ma-

chine vision sensing of plant structural parameters. In: Biological Sensorics: Critical Technologies for Future Biosystems, 15-17 June, Minneapolis, USA. American Society of Agricultural and Biological Engineers, St Joseph.

6. MCCARTHY, C. L., Hancock, N. H. and Raine, S. R. (2007c) A preliminary field evaluation of an automated vision-based plant geometry measurement system. In: Fifth International Workshop on Functional Structural Plant Models, 4-9 November, Napier, New Zealand, pp. 19.1–19.3.

7. MCCARTHY, C. L., Hancock, N. H. and Raine, S. R. Automated internode length measurement of cotton plants under field conditions. Accepted (subject to revisions) by Transactions of the ASABE (August, 2008).

# Contents

**Abstract** **iii**

**Certification of Thesis** **vi**

**Acknowledgments** **vii**

**List of Publications** **vii**

**List of Tables** **xvi**

**List of Figures** **xix**

**Chapter 1 Introduction** **1**

1.1 The Australian cotton industry . . . . . 2

1.2 Infield variability considerations . . . . . 2

1.3 Variable-rate irrigation for large mobile irrigation machines (LMIMs) . . 3

1.4 Machine vision . . . . . 9

1.4.1 Passive versus active vision sensors . . . . . 9

1.4.2 Spectral reflectance . . . . . 10

1.5 Research aim . . . . . 12

1.6 Hypothesis and approach . . . . . 12

1.7 Dissertation chapter outline . . . . . 15

**Chapter 2 Literature review** **17**

2.1 The measurement requirement – plant responses to water stress . . . . . 17
2.1.1 Plant water status/leaf water potential . . . . . 17
2.1.2 Vegetative growth . . . . . 19
2.1.3 Plant mapping (reproductive growth) . . . . . 21
2.1.4 Discussion . . . . . 22
2.2 Applied machine vision for imaging plants and plant structures . . . . . 23
2.2.1 Plant sensing in agricultural fields . . . . . 24
2.2.1.1 Young crops . . . . . 24
2.2.1.2 Mature crops . . . . . 25
2.2.1.3 Canopy topography . . . . . 27
2.2.1.4 Multispectral imaging . . . . . 27
2.2.2 Plant sensing in greenhouses, laboratories and factories . . . . . 27
2.2.3 Plant sensing of specific morphological features . . . . . 30
2.2.3.1 Leaf description and species identification . . . . . 30
2.2.3.2 Fruit development and yield monitoring . . . . . 31
2.2.4 Generation of 3D plant models . . . . . 32
2.3 Development of research objectives . . . . . 33

**Chapter 3 Infield measurement system for cotton plant geometry 34**

3.1 Fixed object plane geometry measurement . . . . . 34
3.2 Camera enclosure designs and manufacturing process . . . . . 37
3.3 Camera enclosure Marks 1 and 2: preliminary designs . . . . . 39
3.4 Camera enclosure Mark 3: apparatus for 2005/06 fieldwork . . . . . 40
3.5 Camera enclosure Mark 4: apparatus for 2006/07 fieldwork . . . . . 40
3.5.1 Extending the focal length with mirrors . . . . . 41
3.5.2 LED array illumination . . . . . 42

3.5.3 Lensing for a narrow depth of field (DOF) . . . . . 44
3.5.4 Sun visor and shroud . . . . . 46
3.5.5 Other possible modifications . . . . . 46
3.6 Required degrees of freedom for camera enclosure conveyance . . . . . 47
3.7 Manual conveyance of camera enclosure (2005/06 fieldwork) . . . . . 49
3.8 Automatic conveyance of camera enclosure (2006/07 fieldwork) . . . . . 51
3.8.1 Automated quad-axis drive system . . . . . 52
3.8.2 Control panel for chassis motors . . . . . 53
3.8.3 Transport of chassis . . . . . 55
3.9 Cost estimate for camera enclosure . . . . . 57

**Chapter 4 Image processing for a single frame 58**

4.1 Introduction . . . . . 58
4.2 Evaluation image sequences . . . . . 60
4.3 Verification of measurements obtained with manual node identification . 64
4.3.1 Internode length calculation . . . . . 64
4.3.2 Verification against physical measurements . . . . . 66
4.4 Approaches for automated node identification from imagery . . . . . 69
4.5 Preprocessing of field images . . . . . 70
4.6 Colour processing and thresholding . . . . . 73
4.6.1 Global thresholding . . . . . 73
4.6.2 Adaptive thresholding . . . . . 78
4.7 Edge detection . . . . . 80
4.8 Line detection . . . . . 81
4.9 Line detection using eigenvalues of the Hessian matrix . . . . . 85
4.10 The ‘vesselness’ measure . . . . . 86
4.10.1 Extracting branches from vesselness image . . . . . 88

4.10.2 Vesselness response for non-branch features . . . . . 91
4.11 Fitting lines to branch segments . . . . . 91
4.11.1 Determining line centre points . . . . . 94
4.11.2 Main stem identification via the Hough transform . . . . . 95
4.11.3 Line-fitting algorithms for branch centre points . . . . . 97
4.11.4 Choosing lines to project to the main stem . . . . . 98
4.12 Summary of single frame algorithm . . . . . 100
4.12.1 Algorithm for control data set . . . . . 100
4.12.2 Algorithm for night time infrared images . . . . . 101
4.13 Single frame algorithm evaluation . . . . . 103
4.13.1 Results . . . . . 103
4.13.2 Analysis of erroneous node omission . . . . . 104
4.14 Conclusions . . . . . 105

**Chapter 5 Node tracking across sequential frames 109**

5.1 Introduction . . . . . 109
5.2 Tracking line segments . . . . . 111
5.2.1 Active contour (or snake) model . . . . . 111
5.2.2 Matching line parameters . . . . . 113
5.3 Tracking candidate node positions . . . . . 115
5.4 Grouping candidate node positions . . . . . 117
5.4.1 Morphological dilation . . . . . 117
5.4.2 Data point mesh spacing . . . . . 118
5.5 Calculation of internode length from node trajectories . . . . . 122
5.6 Conclusions . . . . . 124

**Chapter 6 Evaluation of performance 126**

6.1 Introduction . . . . . 126
6.2 Field data collection . . . . . 126
6.2.1 Fieldwork for 2005/06 season . . . . . 127
6.2.2 Fieldwork for 2006/07 season . . . . . 127
6.3 Overall system performance . . . . . 129
6.4 Evaluation of apparatus operational factors . . . . . 130
6.4.1 Camera enclosure orientation versus internode position . . . . . 130
6.4.2 Illumination – day versus night . . . . . 134
6.4.3 Illumination – shadow and sun angle effects . . . . . 136
6.4.4 Depth of field (DOF) . . . . . 140
6.4.5 Enclosure travel speed . . . . . 143
6.5 Evaluation of agronomic factors . . . . . 144
6.5.1 Crop size and cultivar . . . . . 144
6.6 Conclusions and potential improvements . . . . . 145

**Chapter 7 Real-time implementation 147**

7.1 Rationale . . . . . 147
7.2 Automated conveyance of camera enclosure . . . . . 148
7.3 Real-time software execution . . . . . 148
7.4 Interfacing with post processing and control actions . . . . . 150
7.4.1 Variable-rate irrigation control . . . . . 150
7.4.2 Other potential post processing and control applications . . . . . 151
7.5 Conclusions . . . . . 152

**Chapter 8 Conclusions and further work 153**

8.1 Plant-based vision sensing of cotton . . . . . 153
8.2 Practical implementation of infield vision sensing of individual plants . . 154

8.3 Application to irrigation management . . . . . 155

8.4 Recommended further work . . . . . 155

8.4.1 Potential approach for measurement of nodes above white flower 155

8.4.2 System enhancement . . . . . 157

8.4.3 Post-processing considerations . . . . . 159

**References** **160**

**Appendix A Glossary** **177**

**Appendix B Field apparatus implementation details** **180**

B.1 LED illumination for camera enclosure Mark 4 . . . . . 181

B.2 Overall dimensions of automated infield chassis . . . . . 182

B.3 Overall dimensions of quad-axis drive system for automated infield chassis 183

B.4 Motor control circuit for camera enclosure conveyance . . . . . 184

**Appendix C Spectral differences in plant materials** **185**

**Appendix D Algorithm details** **187**

D.1 Edge detection algorithms . . . . . 188

D.1.1 Sobel edge operator . . . . . 188

D.1.2 Edges by adaptive thresholding . . . . . 188

D.1.3 Canny edge detection . . . . . 188

D.2 Pseudocode for processes in the node and node trajectory detection algorithms . . . . . 189

D.2.1 Filtering the lines that are used to obtain candidate nodes . . . . 189

D.2.2 Identifying successive trajectories from smoothed node positions 191

# List of Tables


1.1 Common dimensions for large mobile irrigation machines (LMIMs) in Australia (applicable to both centre pivots and lateral moves, from Foley & Raine (2001)). . . . . 4

1.2 Sensing system travel speed and plant density for various methods of conveyance. . . . . 8

1.3 A comparison of passive and active vision sensors. . . . . 10

1.4 Vegetation indices (Source: Gibson & Power (2000)). . . . . 11

2.1 Plant water status measures. . . . . 18

2.2 Plant vegetative growth measures. . . . . 20

2.3 Plant mapping/reproductive growth measures. . . . . 22

3.1 Feature dimensions of camera enclosure prototypes. . . . . 38

3.2 Comparison of implemented white LED and halogen lighting systems. . 44

3.3 PICAXE program steps. . . . . 54

3.4 Cost estimate for camera enclosure hardware as at January 2007. . . . . 57

4.1 Possible patterns of Hessian matrix eigenvalues in 2D. . . . . 86

6.1 Data sets for evaluation of the measurement technique. . . . . 127

6.2 Number of internode lengths detected for different camera enclosure orientations (Figure 6.1) and different internode positions for Data Set 1, with three replications. . . . . 132

6.3 Analysis of variance for the detected internode position and camera enclosure orientation ('Orientation') treatments. . . . . 132

6.4 Least significant differences for all possible pairs of detected internode positions. . . . . 133

6.5 Least significant differences for comparing pairs of camera enclosure orientation means at the same internode position. . . . . 133

6.6 Mean absolute errors in internode lengths measured for different camera enclosure orientations and different internode positions for Data Set 1, with three replications. . . . . 133

6.7 Analysis of variance for all the camera enclosure orientation ('Orientation') treatments of Internode 2-3 (Table 6.6). . . . . 134

6.8 Analysis of variance for the Angle 0°, Shear 135° and Shear 315° orientation ('Orientation') treatments of Internodes 2-3 and 3-4 (Table 6.6). . 134

6.9 Number of internode lengths detected for different lighting conditions and camera enclosure orientations ('Orientation') at day and night for Data Set 5, with three replications. . . . . 136

6.10 Analysis of variance for the detected internode position, camera enclosure orientation ('Orientation') and lighting treatments as set out in Table 6.9. . . . . 136

6.11 Least significant differences for all possible pairs of illumination conditions. 137

6.12 Daytime data collection hours and camera direction for Data Sets 1 to 5. 137

6.13 Average number of internode lengths detected for different sunlight conditions and camera enclosure orientations ('Orientation'), with three replications. . . . . 139

6.14 Analysis of variance for sunlight condition and camera enclosure orientation ('Orientation') treatments. . . . . 139

6.15 Least significant differences for all possible pairs of sunlight conditions. . 139

6.16 Least significant differences for comparing pairs of camera enclosure orientation means for the same sunlight condition. . . . . 139

6.17 Number of internode lengths detected for different depth of field conditions and camera enclosure orientations ('Orientation') for Data Set 5 (daytime), with three replications. . . . . 143

6.18 Internode length results for different camera enclosure speeds along row for 30 m for Data Set 5. . . . . 144

6.19 Differences identified between plants of evaluated cotton varieties. . . . 145

7.1 Image processing steps for individual frames. . . . . 150

7.2 Estimated post processing execution time for steps required to generate variable-rate irrigation command. . . . . 151

B.1 Electronic component values for LED arrays. . . . . 181

# List of Figures


1.1 Five spans of a large mobile irrigation machine (LMIM) (here, a centre pivot). . . . . 4

1.2 Plan view representation of a field irrigated by an LMIM. . . . . 4

1.3 Conceptual arrangements of sensors mounted on an LMIM. . . . . 7

1.4 Pictorial top view representation of potential sensing system conveyance on a tractor or on a span of an LMIM. . . . . 8

1.5 Typical plant spacing in a cotton field. . . . . 9

1.6 LEPA sock connected to a sprinkler and applying water directly to the ground. . . . . 14

3.1 Initial concept for vision system apparatus. . . . . 35

3.2 Moving image capture apparatus. . . . . 36

3.3 Motion of the plant with respect to the camera enclosure as the camera enclosure approaches, contacts and moves over the plant. . . . . 36

3.4 Vertical section view of camera enclosure designs. . . . . 38

3.5 Stages of manufacture of fibreglass camera enclosure. . . . . 39

3.6 LED illumination for camera enclosure Mark 4. . . . . 43

3.7 One row of LEDs installed in the hinged front window of Mark 4. . . . . 43

3.8 DOF parameters in camera enclosure. . . . . 45

3.9 Sun visor and shroud for camera enclosure. . . . . 47

3.10 Required degrees of freedom for quad-axis drive system from which the camera enclosure is suspended. . . . . 48

3.11 Side view of camera enclosure illustrating pitch angle $\phi_p$. . . . . 48

3.12 Top view of camera enclosure illustrating effect of yaw angle. . . . . 48

3.13 Mechanical joints for camera enclosure's manual conveyance. . . . . 50

3.14 Manually moved camera enclosure in a cotton crop. . . . . 50

3.15 Automatic conveyance of camera enclosure in a cotton crop. . . . . 51

3.16 Mechanical joints for camera enclosure's automatic conveyance. . . . . 52

3.17 Electrical control panel for chassis motors. . . . . 54

3.18 Block diagram of motor control circuit for automated conveyance of the camera enclosure. . . . . 55

3.19 Chassis road transport by trailer. . . . . 56

4.1 A typical full-scale deinterlaced image for analysis. . . . . 59

4.2 Diagrammatic representation of node numbering on a plant. . . . . 61

4.3 Plan view of the crop rows (east-west), the direction of the afternoon sun's rays and the camera and its optical axis. . . . . 62

4.4 Sample images from video sequences used for evaluating image processing techniques. . . . . 63

4.5 Calculation of apparent internode distance from a single frame. . . . . 65

4.6 Manual node identification from imagery. . . . . 67

4.7 Apparent internode distances in imagery by manual identification of nodes. 68

4.8 Internode length measurements by manual on-screen and physical methods. 69

4.9 Mask generation process. . . . . 72

4.10 Segmentation of a glasshouse image based on the 'excess green' criterion. 75

4.11 Excess green transformation of sample images. . . . . 76

4.12 RGB channels of sample images. . . . . 77

4.13 Adaptive thresholding of Sample Image 1. . . . . 79

4.14 Edge profile descriptors in one dimension. . . . . 81

4.15 Common edge detectors applied to sample images. . . . . 82

4.16 Vision applications where line detection is required. . . . . 84

4.17 Hessian matrix eigenvalues of sample images. . . . . 87

4.18 Vesselness measure of sample images. . . . . 89

4.19 Thresholded vesselness measure of sample images. . . . . 90

4.20 Line-fitting steps on Samples Images 1 and 2. . . . . 92

4.21 Line-fitting steps on Samples Images 3 and 4. . . . . 93

4.22 Gaussian line profile. . . . . 94

4.23 Line centre points of sample images. . . . . 96

4.24 Image processing steps for night time near infrared images. . . . . 102

4.27 Typical node identification results on Sample Image 1. . . . . 104

4.25 Automatically detected nodes for Image Sequences 1 and 2. . . . . 107

4.26 Automatically detected nodes for Image Sequences 3 and 4. . . . . 108

5.1 Active contour model iterations for main stem segment of vesselness transformation of Sample Image 1. . . . . 113

5.2 Active contour model iterations for branch segment of vesselness transformation of Sample Image 1. . . . . 114

5.3 Matching of line segments detected in Image Sequence 1. . . . . 116

5.4 Velocity of the plant nodes with respect to the camera before and after the camera enclosure contacts the plant. . . . . 117

5.5 Automatically detected nodes Image Sequence 1. . . . . 120

5.6 Automatic grouping of candidate nodes for Image Sequence 1. . . . . 121

5.7 Delaunay Triangulation of candidate node data points of Image Sequence 1 for different y-scales. . . . . 123

5.8 Trapezium in $y$-$t$ space representing adjacent nodes detected at times $t$ and $t+1$. . . . . 125

5.9 Graphical representation of the algorithm used to distinguish pairs of successive node trajectories from pairs of adjacent node trajectories. . . 125

6.1 Tested camera enclosure orientations. . . . . 128

6.2 Comparison of internode length measurement by automatic image processing and manual field measurement. . . . . 129

6.3 Images of a single plant from Data Set 5, showing different lighting sources. 135

6.4 Images from Data Sets 1 to 5, showing different sunlight conditions and varieties. . . . . 138

6.5 Stylised representation of shadow and heliotropism effects of sun position when the camera towards or away from the sun. . . . . 141

6.6 Photo of Data Set 2 canopy, showing leaves oriented towards the sun. . 141

6.7 Images of a single plant from Data Set 5, showing effect of a narrow depth of field. . . . . 142

7.1 Conceptual diagram of an FPGA . . . . . 149

7.2 Conceptual block diagram of real-time imaging system and associated variable-rate irrigation control . . . . . 152

8.1 Top view of a cotton plant with yellow flowers, captured with narrow band filters. . . . . 157

A.1 A cotton plant with significant attributes labeled. . . . . 179

B.1 Electronic circuit for LED illumination. . . . . 181

B.2 Schematic diagram of automated infield chassis, with overall dimensions (in mm). . . . . 182

B.3 Schematic diagram of quad-axis drive system, with overall dimensions (in mm). . . . . 183

B.4 Schematic diagram of motor control circuit. . . . . 184

C.1 Spectral response (300–2500 nm) of plant materials. . . . . 186

C.2 Spectral response (325–1075 nm) of cotton plant materials. . . . . 186

# Chapter 1

# Introduction

Agriculture accounted for an estimated 65% of Australia's water consumption in 2004-05, with the largest water users being the pasture and cotton industries (Australian Bureau of Statistics, 2006). Water use efficiency has the potential to be improved through precision agriculture, an area of technological advance which aims to reduce resource wastage and increase yields in agriculture by accounting for the variability of yield-affecting factors throughout a field. The most commonly adopted precision agriculture technologies are grid sampling, variable-rate application for fertiliser, yield monitoring and yield mapping (Zhang et al., 2002). However, spatial variation of water and nutrient requirements may be achieved for large mobile irrigation machine (LMIM) irrigation through use of sensors, controls and decision making tools (Evans et al., 1997b).

There is a wide range of environmental sensing alternatives applicable to precision agriculture. Ultimately, the condition of the plant is an indicator of appropriateness of water (and nutrient) supply. Automating visual assessment of plant condition, to provide sensing information which would enable spatially varied irrigation, is possible using machine vision.

## 1.1 The Australian cotton industry

Cotton accounted for 16.2% of Australian irrigation water use (17535 GL at an application rate of 6.4 ML/ha) in 2004-05 (Australian Bureau of Statistics, 2008). Cotton was selected as the most suitable crop to study for the following reasons:

- There is strong support for the cotton industry in southern Queensland, and particularly from the Cooperative Research Centre for Irrigation Futures (CRC IF) and the National Centre for Engineering in Agriculture (NCEA).
- The cotton industry is presently a large user of LMIM irrigation in Australia and is expected to increase adoption of LMIMs in the future.
- Cotton is an economically viable crop of national significance.
- The cotton plant has a complex structure that presents many sensing alternatives including some that may be applicable to other crops.

## 1.2 Infield variability considerations

The spatial and temporal variability of crop factors in a field has been appreciated for centuries (Zhang et al., 2002). These factors include yield distribution, field topography, soil properties, crop health and growth, weed and disease infestation, and management practices such as fertiliser application and irrigation pattern (Zhang et al., 2002). Bramley & Hamilton (2004) report that in any given year, yield variation within Australian vineyards is typically in the order of ten-fold.

Sadler et al. (2000a) speculate that water is a pertinent resource for precision management since yield is highly correlated with water application in water-limited situations, and that further evidence is given by:

- the lack of correlation between yield and fertility for many crops;

- the spatial variability of crop temperature (and hence, water stress) that is indicated by remote sensing images; and
- the known spatial variability of soil properties, including water holding capacity.

From investigations of canopy temperature and soil moisture content in a corn field, Sadler et al. (2000b) reported that management zones less than ten metres in size may be required to account for spatial variation.

Variation in plant stress indicators due to cultivar is expected to be minimal, since different cotton cultivars follow the same growth and development patterns but under varying heat unit (Appendix A) or timing requirements (Khan, 2003; Oosterhuis, 1990).

## 1.3 Variable-rate irrigation for large mobile irrigation machines (LMIMs)

Large mobile irrigation machines (LMIMs) consist of a series of towers which move concurrently in a field, applying water via sprinklers suspended from the gantry between the towers (also known as spans, Figure 1.1). There are two types which are centre pivots and lateral moves. The main difference between lateral moves and centre pivots is that lateral moves traverse a field whereas centre pivots are fixed at one end, causing the towers to rotate around the fixed axis (Figure 1.2). Common dimensions are listed in Table 1.1. A single pass of the machine may be 12 to 36 hours, thus the LMIM operates during the day and night.

Figure 1.1: Five spans of a large mobile irrigation machine (LMIM) (here, a centre pivot).

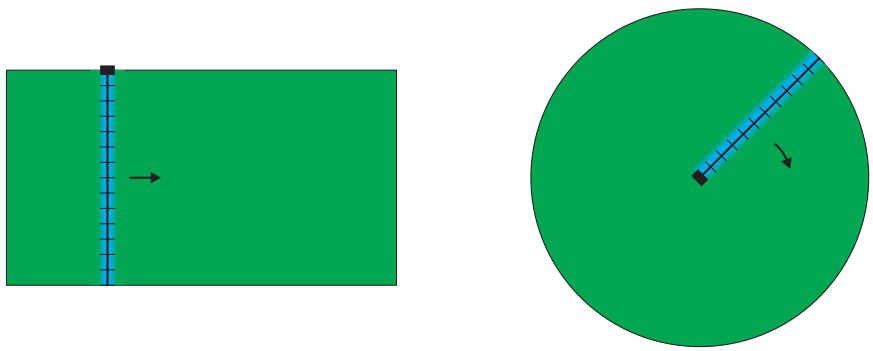

(a) (b)

Figure 1.2: Plan view representation of a field irrigated by an LMIM, where the solid black line represents the LMIM and the arrow represents the LMIM's direction of travel: (a) lateral move; and (b) centre pivot.

Table 1.1: Common dimensions for large mobile irrigation machines (LMIMs) in Australia (applicable to both centre pivots and lateral moves, from Foley & Raine (2001)).

| **Dimension** | **Value** |
|---|---|
| LMIM length | Typical: 400 m<br>Maximum: 500 m, but 1000 m possible |
| Span length | Minimum: 30 m<br>Maximum: 60 m |

NB. Maximum centre pivot tower speed (m/min) = (Centre pivot length) $\times$ $2\pi$/(Time for one pass)
Maximum lateral move tower speed (m/min) = (Length of field)/(Time for one pass)

At present just four percent of Australia's irrigated cotton area is irrigated by LMIMs (Foley & Raine, 2002). However, this proportion is expected to increase in the future (Raine & Foley, 2002) as farmers opt for the potential water, labour and capital savings offered by LMIMs. LMIMs have higher water use efficiency than surface irrigation (Raine & Foley, 2002). However, further water savings are possible since traditionally water discharge from a LMIM is held constant for an entire field despite spatial variations in crop water requirements (Sadler et al., 2000a) caused by soil profile, crop type, plant health or the existence of natural waterways on the field. Increased adoption of LMIMs has emphasised a requirement for research of tools and methods to improve the water efficiency of these machines (Foley & Raine, 2001).

Considerable work is reported in the literature towards development of variable-rate applicators for LMIMs (Sadler et al., 1997a; King & Wall, 1998; Perry & Pocknee, 2004). Variable-rate application may be achieved by a combination of pulsed duty cycles of individual or groups of sprinklers and/or by varying the travel speed of the LMIM.

In 2001, a partnership between researchers at the University of Georgia and the Australian company Farmscan saw the release of a variable-rate irrigation controller for centre pivots (Computronics Corporation Ltd., 2002), and the release of the world's first variable-rate centre pivot machine using this technology (Hobbs & Holder LLC, 2005). The Farmscan system allows irrigation management zones and water application rates to be specified via predefined maps that are uploaded to the variable-rate controller. The predefined maps are based on crop aerial images, yield maps, soil surveys and the farmer's knowledge of the field (Computronics Corporation Ltd., 2002).

The Farmscan system uses a map-based approach for managing variability. However, Evans et al. (1997b) suggest that for variable-rate irrigation under LMIMs to be practical on a large scale, a sensor-based approach for soil or plant properties is required to be developed. Presently 'on-the-go' sensors for monitoring field variability are limited by expense or accuracy, or are not available (Zhang et al., 2002).

Many researchers and manufacturers have attempted to develop on-the-go soil sensors

for soil properties, but the sensors have common limitations of expense and impracticality for on-the-go measurements (Adamchuk et al., 2004). Soil moisture (i.e. volumetric water content) is conventionally estimated as an indicator of the amount of water available to the crop. However, due to soil heterogeneity, meteorology and plant physiological factors, soil moisture is not necessarily an accurate indicator of plant water stress (Jones, 2004).

An alternative view is that the plant is the best indicator of water availability and stress, since plants automatically integrate the atmospheric and soil factors that affect plant water status (Kramer & Boyer, 1995). Plant-based methods of determining irrigation requirements have been reported in the literature for laboratory, glasshouse and field conditions but not for non-destructive on-the-go measurements at high spatial resolution in the field. Hence, plant-based methods of determining irrigation requirement is a particular area of research difficulty and need, particularly to enable the application of variable-rate irrigation.

In principle, a LMIM can be used as a sensing platform that provides regular access to all regions of the field. Data for each crop row may be collected if the implemented sensors have a collective field of view (FOV) of all crop rows or if the sensors have the capability to traverse each span (Figure 1.3).

The sensors potentially have time to traverse the span and maintain high spatial resolution (i.e. high number of effective sensor measurements per unit area in the field) due to the relatively slow speed of a LMIM during irrigation (the maximum speed for a lateral move or the outer towers of a centre pivot may be 2–3 m/min). Multiple sensing systems may need to be implemented to increase sensed area in the field.

In developing the sensing system for LMIMs, the sensing system should not be restricted to use only on LMIMs. The sensing system may be used as an evaluative tool (for example, for identifying spatial variability) when mounted on some other ground-based vehicle that has access to crop areas in a field (e.g. Figure 1.4). Use of different vehicles and travel directions to convey the sensing system lead to a range of travel speeds

(e.g. Table 1.2) and plant densities (Figure 1.5) to consider.

(a)

(b)

Figure 1.3: Conceptual arrangements of sensors mounted on an LMIM: (a) small field of view (FOV) sensors that could either traverse span or be mounted in an array; and (b) large FOV sensors. Conceptual FOV indicated by yellow tint.

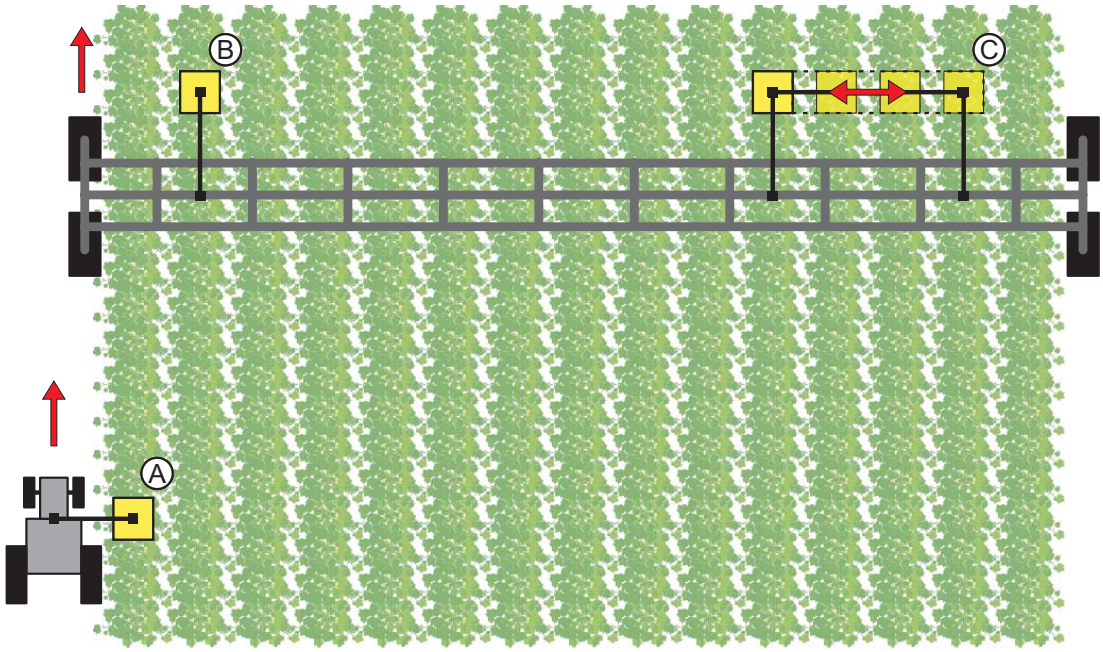


Figure 1.4: Pictorial top view representation of potential sensing system conveyance on a tractor (label A) or on a span of an LMIM (labels B and C). Yellow boxes indicate a conceptual sensing system. See Table 1.2 for further description of labels A–C.

Table 1.2: Sensing system travel speed and plant density for various methods of conveyance.

| **Sensing system conveyance method** | **Travel speed of sensing system** | **Typical plant spacing** | **Figure 1.4 reference** |
|---|---|---|---|
| On tractor in direction of crop row | Equivalent to tractor speed (20 km/h typical) | 10–16 plants/m along row | A |
| On LMIM in direction of crop row | Equivalent to LMIM speed (2–3 m/min typical) | 10–16 plants/m along row | B |
| On LMIM perpendicular to crop row | Governed by independent propulsion mechanism of sensing system across rows | 1 plant/m across row | C |

(a) (b)

Figure 1.5: Typical plant spacing in a cotton field: (a) 10–16 plants per metre along the row; and (b) one plant per metre across the row.

## 1.4 Machine vision

Machine vision is potentially a suitable technology for detecting plant stress by non-contact measurement of plant characteristics, and especially plant architecture. Machine vision systems recover useful information about objects from two-dimensional projections of a scene (Jain et al., 1995). However, there is a wide array of machine vision instrumentation and sensing alternatives. These include the use of active or passive sensors and the ability to measure reflectances in the visible and non-visible bands of the electromagnetic spectrum.

### 1.4.1 Passive versus active vision sensors

Vision sensors may be passive (e.g. cameras) or active (e.g. ultrasonic or laser ranging devices). Passive sensors are entirely dependant on the suitability of ambient illumina-

tion and return colour information for a scene. They may generate depth information from stereoscopic images. Active sensors are less sensitive to changes in ambient lighting conditions. They implicitly return depth information for a scene and by analysis of reflected beams may return colour information. Depth information is useful for determining actual dimensions of objects (e.g. stem diameter, leaf area or internode length). However, the task of active sensor image interpretation retains all the difficulties associated with interpreting images from passive sensors (Jain et al., 1995). Table 1.3 contains a comparison of passive and active vision sensors.

Table 1.3: A comparison of passive and active vision sensors.

| | **Active sensor** | **Passive sensor** |
|---|---|---|
| Example | imaging radar (laser or acoustic) | camera |
| Scene capture | acquires data for a scene by a process of scanning | acquires data for an entire scene simultaneously |
| Effect of ambient environmental conditions | functions effectively in day and night conditions, but ambient daylight (for a laser sensor) and acoustic noise (for an acoustic sensor) must be overcome | requires an external light source, hence the quality of sunlight or artificial light influences data |
| Colour and textural data | using panchromatic illumination, may obtain colour and textural information by analysis of reflected beams | colour and textural information may be obtained |
| Distance data | gives a depth map | using stereoscopic images (multiple cameras/two consecutive images/optics to split single image) and a calibration process, may obtain a depth map |

### 1.4.2 Spectral reflectance

Spectral reflectance is the ratio of reflected to incoming radiation and is used in both remote sensing and machine vision applications (e.g. quality assessment in the food industry). Remote sensing may be used to obtain vegetation indices. Vegetation indices are empirical formulae designed to emphasise the spectral contrast between the red and near-infrared regions of the electromagnetic spectrum, for the purpose of producing quantitative measures of plant biomass and vegetative health (Gibson & Power, 2000).

Table 1.4 contains examples of common vegetation indices.

Table 1.4: Vegetation indices (Source: Gibson & Power (2000)).

| **Vegetation index** | **Formula** |
|---|---|
| Normalised difference vegetation index (NDVI, often used as an index of biomass) | (near infrared − visible red) / (near infrared + visible red) |
| Difference vegetation index (DVI) | (near infrared − visible red) |
| Soil adjusted vegetation index (SAVI) | (near infrared − red) / ((near infrared + red + L)×(1 + L)), where L is a correction factor for the amount of vegetation cover |

Another application of spectral reflectance is for determining the non-visible optical properties of various plant features for the purpose of distinguishing plant features in machine vision applications. In a cotton crop (and particularly for identifying fruit retention or plant mapping procedures) the spectral differences between bolls, squares[1] and stems may potentially be used to differentiate the plant materials. Stems and bolls have a higher moisture content than leaves, so have lower reflectance at water-absorbing wavebands such as 970 nm (Kondo & Ting, 1998). Hence, a differential two-waveband near infrared system may enable differentiation of stems and fruit from leaves despite tonal similarities, as in the cucumber-harvesting robot of van Henten et al. (2002). However, the system developed by van Henten et al. (2002) was in a glasshouse environment under controlled and unstressed crop conditions, in contrast to the cotton crop environment, where moisture content and water stress levels are highly variable and would be expected to have an effect on the plant material's spectral characteristics.

Colaizzi et al. (2003) developed a spectral reflectance and infrared thermometer sensing system on a track on a linear move span to deliver spectral images at high spatial resolution. Sadler et al. (2002) also mounted arrays of infrared thermometers on spans of a centre pivot to map canopy temperature during a dry run of the machine, thus demonstrating use of the LMIM solely as a data gathering platform. However, in practice growers are unlikely to conduct dry runs of the LMIM during the peak irrigation period due to time constraints.

[1] A glossary of cotton terminology is provided in Appendix A.

The implementations of both Sadler et al. (2002) and Colaizzi et al. (2003) have been used for mapping spatial variation in the field rather than real-time assessment of site-specific crop water stress. Similarly, the infrared thermometry system developed by Peters & Evett (2004) had utility only for timing an irrigation event under centre pivot irrigation.

## 1.5 Research aim

The aim of this research is to develop a crop condition sensing system to determine in real-time, water stress in a cotton crop irrigated by a large mobile irrigation machine. The ultimate goal of such a sensing system is its use on a variable-rate LMIM, that is, a LMIM capable of variably adjusting water discharge, at high spatial resolution, in response to actual crop water stress for the purpose of increasing water use efficiency. A LMIM so equipped, and with the support of a decision-making framework, has the potential to become an intelligent learning system, as historical, present and predictive field data are accumulated and compared to optimise water application.

In the context of this research, the desired spatial resolution is defined to be equivalent to one effective sensor measurement for each sprinkler (where there is one sprinkler for each row and row spacing is one metre) at one-metre intervals in the direction of travel of the machine. Hence, the target spatial resolution for sensor measurements is one square metre.

## 1.6 Hypothesis and approach

The hypothesis of this research is that non-destructive measurements of significant plant parameters can be made automatically and conveniently with respect to field irrigation machinery operation.

LMIM irrigation of a cotton crop has been selected as an appropriate target application to assess the viability and utility of using the growing plant as an 'irrigation sensor'. Under commercial conditions, LMIM irrigation is characterised by high-frequency application of water (typically once every few days) and is therefore potentially amenable to real-time sensing and control. Maximising the potential for real-time sensing and control (by maximising temporal and spatial frequency of irrigation) leads to the following additional LMIM operating requirements for the sensing system:

- The system must be applicable for use during the peak irrigation period, in which a LMIM pass of a particular plant may occur every three to four days and the LMIM is in use nearly continuously throughout the day and night. The peak irrigation period for cotton coincides with a crop age of four months (significant ground cover) to the end of the season.
- The LMIMs may be installed with low energy precision application (LEPA) systems. LEPA is a high-efficiency system which applies water directly to the soil and may be spatially varied at one-square metre resolution (Figure 1.6). LEPA is the highest precision application system for LMIMs and is the basis of the target spatial resolution for the sensing system.

The choice of plant metric/s to measure and automate should be agronomically-driven by cotton industry standards rather than by current technological standards, i.e. the primary driver for research direction taken is agronomy rather than technology. It is considered more valuable to choose a significant plant attribute to measure than to select a less significant plant attribute which may potentially present a simpler sensing solution.

The desire to measure plant attributes at high spatial resolution means multiple sensors are required to be deployed in the field. Industry adoption of the devised sensing techniques is also desirable. Hence, cost per sensor is an appropriate consideration for the present research application and it is desirable to develop a sensing system that operates in natural daylight conditions.

Figure 1.6: LEPA sock connected to a sprinkler and applying water directly to the ground. Compare with Figure 1.1 where a mist of applied water is visible above the canopy being irrigated.

In summary, consideration of the operation of an LMIM in a cotton field under commercial conditions leads to the following guidelines for the sensing system's performance:

- Conveyance speed of sensing system: 2 to 3 m/min (0.03 to 0.05 m/s) to 20 km/h (5.6 m/s)
- Plant density: 10 to 16 plants/m along row and 1 plant/m across row
- Spatial resolution of plant measurements: 1 $m^2$
- Daily operating hours: up to 24 h continuous

These conditions contribute to the design, development and evaluation processes of the sensing system throughout the thesis.

## 1.7 Dissertation chapter outline

This dissertation contains eight chapters addressing the development and testing of the vision-based sensor.

- The aim of this project is to develop a sensor that aids in irrigation decisions. Therefore, **Chapter 2** describes plant-based methods of inferring irrigation requirement and identifies cotton plant internode length as a significant indicator of water stress. Internode length is visually-assessable by a human which suggests that internode length measurement may potentially be automated using machine vision. Chapter 2 also contains a literature review of machine vision applications for plants which reveals that generally, machine vision measurement of plant parameters in the field is restricted to whole-plant attributes (e.g. plant height). The literature review leads to formulation of the research objectives.

- A mobile infield machine vision system is required to identify internode length of individual plants in an outdoor environment of densely-populated plants. **Chapter 3** contains the design of a mobile enclosure which non-destructively forces individual plants against a transparent panel. A camera mounted behind the transparent panel views the plants in a fixed object plane which enables reliable single-camera geometric measurement. Apparatus for automatic infield conveyance of the camera enclosure is also reported in Chapter 3.

- Automated internode length detection from video imagery required identification of green stems from a background of green foliage. **Chapter 4** evaluates image processing techniques for automatic main stem node identification in individual video frames including colour thresholding and edge and line detection. The 'vesselness' measure (a function of the eigenvalues of the Hessian matrix) was found to be most effective for detecting lines corresponding to branches. However, other foliage edges were also incorrectly identified as branches and these 'false positives' contributed to the set of detected nodes.

- True nodes were consistently identified in sequential frames whereas false posi-

tive nodes were largely random in nature. Therefore, sequential frame analysis in **Chapter 5** was necessary to remove false positive candidate nodes and provide reliable internode length measurement. Candidate nodes were successfully grouped into node trajectories using a method based on Delaunay Triangulation.

- Automated internode length measurement results are provided in **Chapter 6** for a range of environmental and operating conditions. Natural daylight conditions were found to significantly influence the vision system's performance. The system performed most reliably in partially cloudy conditions (diffused sunlight) with the camera facing either north or south. The vision system's night time performance was found to be as reliable as its performance under favourable daylight conditions.

- **Chapter 7** considers system design and operation in the context of a real-time environment, i.e. with the camera enclosure mounted on an irrigation machine or some other ground-based vehicle. A conceptual FPGA-based analysis of software execution time is included.

- Final conclusions for the research are provided in **Chapter 8**. Recommended further work includes extension of the vision system to measure other significant plant attributes such as nodes above white flower.

# Chapter 2

# Literature review

## 2.1 The measurement requirement – plant responses to water stress

Using the plant as a water stress sensor potentially involves sensing plant water status or plant vegetative and reproductive growth. The sensed plant attributes may be useful as absolute measurements or as differential measurements. Differential measurements may be obtained from comparisons with previous LMIM passes or other plants. Appendix A contains definitions of plant growth and physiology terms.

### 2.1.1 Plant water status/leaf water potential

Plant water status indicates the force that moves water within a plant and may be expressed as plant water potential (Kramer & Boyer, 1995) and estimated by leaf water potential (Huck & Klepper, 1977). Direct measurement of leaf water potential is labour intensive and unsuitable for automation (Jones, 2004). Hence, investigations of indirect measurement of plant water potential via plant properties such as change in leaf thickness, leaf growth rate and leaf temperature have been reported in the

literature (Table 2.1). Stem diameter changes have been investigated as a possible indirect measurement of leaf water potential for decades (Klepper et al., 1971; Huck & Klepper, 1977).

Table 2.1: Plant water status measures.

| **Feature** | **Traditional measurement techniques** | **References** |
|---|---|---|
| Stem/fruit diameter, leaf growth rate, leaf thickness | Linear variable displacement transducers or strain gauges that are continuously clamped to the specimen (including commercial devices) | Lu & Neumann (1999), Yatapanage & So (2001), Goldhamer & Fereres (2004) |
| Leaf angle | Manual observation, inclinometer | Meyer & Walker (1981), Ehleringer & Hammond (1987), Jones (2004) |
| Spectral response | Portable spectroradiometer at the canopy or plant level, under field and laboratory conditions | Gausman et al. (1971), Jackson & Ezra (1985), Bowman (1989) |
| Leaf temperature | Infrared thermometers or thermal imagery for non-contact measurement | Jones et al. (2002), Sadler et al. (2002), Colaizzi et al. (2003) |

Leaf angle is an indicator of visible leaf wilting, which is often considered a belated stress response (Jones, 2004). Leaf angle has added significance in the cotton variety *Gossypium hirsutum* which is heliotropic (Lang, 1973; Ehleringer & Hammond, 1987), that is the leaves track the sun and maintain an average angle of 40 degrees with the sun's rays, except during drought conditions (Oosterhuis, 1990). *Gossypium hirsutum* accounts for 90% of the world's cotton production (Cantrell, 2005).

Leaf water potential and related plant water status measures are affected by meteorological conditions and therefore undergo diurnal variation. The effect of the diurnal variation must be considered when comparing multiple plant water status measurements. Techniques suggested in the literature include:

1. Considering measurements in the context of the daily cycle, by predicting the specific influence of the diurnal variation (e.g. (Peters & Evett, 2004) for canopy temperature) or by normalising observed transient changes against maximum

daily changes. The second alternative was implemented by Goldhamer & Fereres (2004) for trunk diameter measurements and by Kacira et al. (2002) for projected plant area measurements.

2. Comparing measurements from the same time or under the same meteorological conditions each day. For example, comparing leaf water potential measurements taken predawn or at solar noon.

3. Comparing measurements with a continuously-monitored 'reference' specimen. This technique was recommended by Moriana & Fereres (2002) for stem diameter values, by Jones et al. (2002) for thermal imaging of grapevines and by Peters & Evett (2004) for canopy temperature.

Technique 1 may be implemented if enough information about the diurnal variation is known. Implementation of Technique 2 is possible in the LMIM application environment if irrigations are timed such that the LMIM passes over each area at the same time every day. However, Technique 3 requires reference plants to be selected and additional instrumentation to be installed in the field, which may be undesirable over a large spatial area.

### 2.1.2 Vegetative growth

Vegetative growth is the most sensitive indicator of the onset of water stress and indicators include plant height, leaf area index and projected plant area (Table 2.2). From Table 2.2, research towards the automation of field measurement of whole-plant attributes such as plant height and biomass has been reported in the literature. Internode length is a sub-plant attribute and reports of research towards automated field measurement were not found in the literature.

Cotton plants follow a structured growth and development pattern in which a new node develops on the main stem every two to three days. Internode length in cotton is highly influenced by environmental stresses, whereas node development is largely independent

Table 2.2: Plant vegetative growth measures.

| Feature | Traditional measurement techniques | References |
|---|---|---|
| Plant height | Ultrasonic or infrared beams, laser rangers | Tumbo et al. (2002), Geiger (2004), Schumann & Zaman (2005) |
| Leaf area index | Manual allometric techniques, hemispherical photography, radiation interception (including commercial devices) | Breda (2003), Jonckheere et al. (2004) |
| Internode length | Manual observation | Oosterhuis (1990), Hearn (1994) |
| Biomass | Machine vision, remote sensing | Bjurstrom & Svensson (2002), Praat et al. (2004) |
| Top- or side-projected plant area | Machine vision | Casady et al. (1996), Murase et al. (1997), Kacira et al. (2002) |

of stress (Hearn, 1994). The distance between consecutive nodes on the main stem indicates amount of vegetative growth. An internode length becomes fixed (i.e. ceases to elongate) below the fourth node. Hence, for cotton the distance between the fourth and fifth main stem nodes of a plant is used as an indicator of the amount of stress that the plant has experienced in a time period eight to twelve days earlier. Internode length measurement is part of a plant-based water stress monitoring regime for cotton suggested for growers by organisations including the Australian Cotton Cooperative Research Centre (Milroy et al., 2002).

A fully developed internode should be greater than 50 mm (McKenzie, 1998), with smaller internode lengths indicating moisture stress and internode lengths greater than 70 mm indicating excessive vegetative growth. Field observation of internode lengths for the present research ranged from typically 15 to 110 mm (Figure 4.8, Chapter 4), with internodes less than 50 mm typically corresponding to internode positions that were not yet fully elongated. The upper bound of 110 mm indicates excessive vegetative growth in the observed plants.

Average internode length for the entire plant may be obtained by dividing the plant height by the number of nodes (Johnson Hake et al., 1996). This quantity is also known as the plant's height to node ratio. Since an internode length is fully expanded after the fourth node position, an estimate of the average length of the top five internodes may be obtained by dividing the change in plant height for a particular time period by the number of 3-day intervals in that time period (where a new node develops on the plant's main stem on an average of every 3 days) (Landivar et al., 1996). Stabile (2005) reported that the average of the top five internode lengths estimated by this method was found to be more sensitive to moisture stress than height to node ratio and with a potentially shorter time constant for response to water stress than consideration of the fourth-to-fifth internode only. Therefore, the precise measurement of the top five internode lengths has potential use in cotton irrigation scheduling and automation of the measurement has potential extension into the measurement of other plant parameters such as those included in plant mapping (next section).

### 2.1.3 Plant mapping (reproductive growth)

Development of a cotton plant follows a standard pattern, and to optimise yield, a balance between vegetative and reproductive growth is required. Mild stress in cotton causes the highest reproductive growth, whereas low stress encourages vegetative growth and high stress reduces boll setting (Oosterhuis, 1990). Cotton plant mapping (Table 2.3) is a potential irrigation scheduling tool which incorporates both vegetative and reproductive growth, and has been researched extensively in Arkansas (Oosterhuis, 1990). Cotton plant mapping involves frequently recording the positions of squares and bolls on a growing plant to diagnose plant health, but may be reduced to a few key indicators such as nodes above white flower (NAWF) and height to node ratio (Oosterhuis, 1990).

Comparison of sampled NAWF and heat unit data with a target development curve (Appendix A) allows cotton crop health to be diagnosed and a management strategy to be implemented. Field measurements are made manually for a recommended total

of 40 plants, once or twice every week throughout the season (University of Arkansas Division of Agriculture, 2005).

Table 2.3: Plant mapping/reproductive growth measures.

| **Feature** | **Traditional measurement techniques** | **References** |
|---|---|---|
| NAWF, height to node ratio, number of squares set and shed | Manual observation | Oosterhuis (1990), Bourland et al. (1997), Teague et al. (1999) |

### 2.1.4 Discussion

Methods of detecting plant water stress based on plant water status, vegetative and reproductive growth have been presented. Plant water status measures require knowledge of the current meteorological conditions in order to be applied to irrigation management. Plant water status measures such as change in stem diameter and projected plant area also require comparison with historical values of the same plant specimen. Therefore, in the LMIM application environment, the sensing platform would be required to locate the same plant specimen on every pass of the LMIM. In contrast, vegetative and reproductive growth measures integrate previous stress levels to serve as a meaningful stress indicator on an individual plant basis. Hence, temporal comparisons of a sample area within a crop need not necessarily involve the location of exact specimens for comparison.

In addition to considerations for the sensing system implementation, monitoring of both vegetative and reproductive growth in cotton crop management is necessary to ensure that the balance between vegetative and reproductive growth is maintained. Plant mapping is achieved traditionally by labour intensive manual sampling techniques and no reports of possible automation of the techniques were found in the literature. Automation of internode length measurement would potentially enable large-scale quantification of vegetative growth in a cotton crop. Sensing node positions for the purpose of internode length measurement may also potentially lead to a measurement technique for other node-based cotton plant properties such as nodes above white flower.

Sensed plant data (e.g. internode length) is anticipated to be most usefully employed in an irrigation application in temporal and/or spatial field comparisons, rather than in comparison with crop models. A spatial comparison may entail observation of intrafield variation, whereas a temporal variation may involve comparing internode length growth rates for a sample crop area over a series of irrigations with varying irrigation amounts.

## 2.2 Applied machine vision for imaging plants and plant structures

Attributes of internode length and plant mapping are significant crop development indicators for agronomists and automation of the measurements is potentially achievable using machine vision. However, the design of a vision system for the measurement of plant attributes will be affected by many factors, such as the scale of the plant measurement (i.e. leaf- or canopy-level) and the measurement environment (e.g. a laboratory or in the field). The use of shape, range, texture and spectral properties of plants in machine vision systems are reported in the literature. Not all vision system and image processing solutions are automated, but they provide relevant considerations in the design and application of a vision system for plants.

Amongst the variety of plant-based vision systems available, the following major measurement categories have been identified and hence, form the outline of this literature review:

- plant sensing in agricultural fields;
- plant sensing in greenhouses, laboratories and factories (usually includes robotic post-actions such as automatic harvesting or sorting);
- plant sensing of specific morphological features; and
- plant sensing to develop 3D plant models.

### 2.2.1 Plant sensing in agricultural fields

Vision systems developed for measuring plants in agricultural fields are typically required to analyse spatial patterns at the field scale and at high resolution. The goal of such analyses includes yield prediction/monitoring or evaluation of crop management practices.

The magnitude of information required in measuring all plants within a field implies complete automation of the sensing task. However, the outdoor agricultural environment presents complexities that make automation challenging. These complexities include variable natural lighting, wind-induced foliage movement, and occlusion and obscuration of plant features by foliage from neighbouring plants and background material. Automated machine vision sensing of individual plants under field conditions is therefore typically limited to early stage crops (where neighbouring plants are too small to be touching) or to whole-plant characteristics such as plant biomass for more mature canopies.

#### 2.2.1.1 Young crops

Projects such as corn seedling population sensing for the purpose of determining optimal plant spacing and evaluating the uniformity of seeding machines have been conducted in the USA (Shrestha & Steward, 2003; Shrestha & Steward, 2005). Shrestha & Steward (2005) used a camera to collect top view images of the corn plants which were then segmented from the background soil. Pixels were grouped to form estimated projected foliage cover for individual plants, with roundness and area of segmented objects used to separate plants from weeds.

Segmenting foliage from background soil (in top view images) is an important first step in the automated image processing task of young crops. However, objects and their backgrounds often exhibit common intensities which reduces the effectiveness of a monochrome threshold (Tian & Slaughter, 1998). Ewing & Horton (1999) evaluated

three colour models for segmenting a young corn canopy from background soil and speculated that diffuse lighting from cloudy days may provide better illumination of leaves which would otherwise be in shadow on a clear day. Tian & Slaughter (1998) developed a self-learning segmentation algorithm which had superior performance in poor lighting (i.e. overcast conditions). Steward et al. (2004) subsequently developed a 'truncated ellipsoid' model of colours expected to be associated with green leaves under a range of outdoor lighting conditions which Shrestha & Steward (2005) used to automatically separate corn leaves from the background.

Automatic exposure settings of 'point and shoot' digital cameras are capable of providing maximum separation of RGB component colours and excellent visual quality (Meyer et al., 2004) resulting in correct classification of images featuring exclusively plant (i.e. foliage), soil or residue (i.e. stubble) material under a range of illumination conditions. Noh et al. (2005) performed further colour calibration of foliage by including a reference board in the field of view of the image, which was painted with colours of known reflectance for comparison with the foliage. This permitted nitrogen deficiency to be estimated under a range of lighting conditions.

#### 2.2.1.2 Mature crops

In mature crops, segmenting the plant pixels of interest from the background is still an important first step for image processing tasks. In vineyards, the leaf orientation (i.e. the orientation of a tangent plane to the leaf) is generally vertical so an on-the-go downward-facing camera is not as useful for determining canopy properties. However, a developed vineyard canopy is particularly suited to on-the-go machine vision measurement with sideways-facing cameras due to the spacing between rows, which enables a camera and backing board to fit comfortably on either side of the canopy, such that a side view of the foliage can be obtained. Such a system was implemented by Praat et al. (2004), with biomass being estimated by counting green vine pixels and discounting the distinctly-coloured background board. Row spacing enabled observation of the shadows of individual rows cast onto the ground at solar noon (Williams & Ayars, 2005).

Shadow pixels were counted (with a manual threshold on pixel intensity) as an indication of canopy biomass. Bjurstrom & Svensson (2002) extended vision sensing of vineyard canopies to the leaf-level by developing algorithms based on shoot colour to perform shoot counting.

For skyward-facing cameras, such as in hemispherical photography for leaf area index (LAI) estimation (Jonckheere et al., 2004), foliage is required to be separated from background sky and clouds. LAI measurements are typically collected for crop developmental stages up to closed canopy, so foliage in collected imagery is frequently overlapping and automation of the segmentation task involves methods such as automatic thresholding and edge detection (Ishida, 2004; Nobis & Hunziker, 2005).

For small plants, an on-the-go vision system consisting of a lightproof cover can be mounted on the back of a tractor or on a mobile robot, in order to control lighting conditions of the plants under the cover during imaging in the field (e.g. Edan et al. (2000) and Hemming & Rath (2002)). Implementing an on-the-go infield vision system with controlled lighting is more difficult for individual larger plants. In a developed rice canopy, Casady et al. (1996) manually positioned a portable frame and shroud about each plant to segment foliage pixels and measure biomass. However, Tarbell & Reid (1991) transported mature individual corn plants from the field to a laboratory in order to compare foliage colour with colour charts and to measure leaf area from plant silhouettes on a light stage.

Active sensors are not affected by variation in ambient lighting and find common application in developed canopies. Geiger (2004) used an array of infrared emitters on either side of a cotton row to measure cotton plant height on-the-go. The data was used to generate maps of change in canopy height. Tumbo et al. (2002), Wei & Salyani (2004) and Schumann & Zaman (2005) used laser scanning and ultrasound to estimate the volume of trees in a citrus orchard. Other applications of laser scanning includes the estimation of the lean angle and volume of standing trees (Hyyppa et al., 2001; Theis et al., 2004).

#### 2.2.1.3 Canopy topography

Two- and three-dimensional imagery-based canopy visualisations have been used to visually assess crop status at the field scale. Image mosaicing or sequencing involves a moving camera capturing top view images (for example) of a crop row and then automatically identifying where consecutive images 'stitch' together, using matching algorithms. Over a large area, a single high-resolution image of the field can be accumulated (Kise & Zhang, 2006). Three-dimensional maps of canopy structure were obtained by Rovira-Mas et al. (2005) using aerial stereoimages captured from a remote-controlled helicopter with GPS. The change in scene elements caused by wind undermines matching applications such as mosaicing.

#### 2.2.1.4 Multispectral imaging

Potential multispectral imaging technologies for detecting plant water stress include using visible, IR, NIR, UV and microwave radiation (Takakura et al., 2002). Bacci et al. (1998) showed that in a growth chamber, colorimetric techniques could be used to detect plant stress and Carter & Miller (1994) found that herbicide-induced stress could be detected with colour and narrowband digital imagery. Leinonen & Jones (2004) combined visible and thermal imaging to identify regions of interest in a thermal image of plants (e.g. by isolating plant from soil pixels). Chaerle et al. (2003) has also used time-lapse thermal, fluorescence and video imaging of leaves to detect herbicide damage.

### 2.2.2 Plant sensing in greenhouses, laboratories and factories

Applications of machine vision systems in controlled indoor environments (e.g. greenhouses, laboratories and factories) include automatic irrigation management, fruit harvesting and flower grading. The greenhouse environment removes many of the variables that complicate outdoor agricultural machine vision systems. Under green-

house/laboratory conditions, lighting and positioning of free-standing individual plants may be controlled, so the drawbacks of variable natural sunlight, irregular spacing/ location of plants and complicated image backgrounds may potentially be overcome.

The ability to control the environmental conditions in an automated greenhouse irrigation system means that small changes in intricate plant geometric relationships can be detected on a continuous time scale and attributed to a particular cause (such as water stress). Canopy changes due to induced stresses can also be isolated by signal processing from plant diurnal movement and growth. Irrigation scheduling systems have been developed using leaf tip tracking for wilt detection (Seginer et al., 1992) (manual system), change in side projected area (Murase et al., 1997) and change in top projected area (Kacira & Ling, 2001; Kacira et al., 2002). In these applications, the plant parameter of interest is isolated from a binary image in which the plant is segmented from the background. These systems tend to focus on detecting small differences in geometry (leaf inclination, canopy architecture) rather than analysing foliage spectral/hue properties. Techniques devised for automated greenhouse systems have potential application in sustainable biosystems for space (e.g. research to develop automatic irrigation and management systems for crops on space missions (Fleisher et al., 2006)).

Identifying the onset of water stress using petiole wilt detection in a vine canopy was evaluated by Waksman & Rosenfeld (1997). The average petiole angle was extracted from greyscale vine images using line detection techniques and results from images with the light source in different positions were combined in order to reduce occlusion by shadows. Kurata & Yan (1996) calculated the average incline angle of rachis (the central axis of compound leaves) lines in tomato plants to estimate water potential. Waksman & Rosenfeld (1997) also studied colour distribution in plant leaves to identify paleness and hence, the onset of stress. Shimizu & Heins (1995) observed variation in stem elongation rate of a single-shooted plant using an automatic system that captured the silhouettes of the side and front views of a plant simultaneously with a mirror.

Machine vision is typically one of a suite of sensors employed in automatic moni-

toring of plants in greenhouses. Other sensors include infrared thermometers, load cells, anemometers and photosynthesis meters (van Henten & Bontsema, 1995; Ehret et al., 2001; Prenger et al., 2005). Vision systems are not necessarily restricted to direct plant measurements and have been used to assist deployment of other sensors. Kim & Ling (2001) developed a conceptual machine vision system for automatic robotic positioning of an infrared thermometer to enable temperature measurement of individual leaves within a canopy.

A major industry in the Netherlands is cut flowers and a shortage in unskilled labour makes automation of cutting flowers desirable. In this industry, flower stalks are required to be identified prior to harvest. Noordam et al. (2005) considered methods of locating a cutting position on a rose stem and compared the use of stereo imaging, laser triangulation, x-ray imaging and reverse volumetric intersection, a variation of the process of using multiple angles to identify the 3D outer contour of an object (Hemming, Golbach & Noordam, 2005). Occlusions by leaves and stems were found to be limiting to the laser triangulation technique and to identifying correspondences in the stereo imaging system. However, the reverse volumetric intersection technique in conjunction with the Hough transform was promising for identifying stems. Thin leaves were completely invisible in the x-ray images, but stems could be occluded by other stems and there are severe safety regulations regarding the use of x-ray imaging. Gerberas have less foliage around the desired cutting position so Kawollek & Rath (2005) used the expected constant width of stem regions to identify stems from multiple views of the plant.

Robotic harvesting of fruit in greenhouses consists of design options relevant to plant-based machine vision systems. A differential two-waveband infrared vision system was designed and tested that made use of the spectral differences in fruit and leaves at 850 and 970 nm to identify cucumbers on a vine (van Henten et al., 2002). This spectral difference also occurs between stems and leaves (Kondo & Ting, 1998). Hemming et al. (2005) used an air blower system to distinguish leaves, fruit and stems in a canopy on a distinctly-coloured background. Leaves were identified as those objects which moved

with the air stream, while fruit and stems remained relatively still. Additional image processing enabled selective harvesting of only ripe or mature fruit by modeling the fruit size or volume.

Machine vision has been used commercially to grade plant cuttings in the geranium (Simonton, 1990), sugar cane (Wang et al., 1998) and forestry (Wilhoit et al., 1994) industries. The imaging environment is typically an assembly-line. Features of plant cuttings such as flower size and stem-to-leaf area ratio are measured by identifying flowers, leaves, petioles and stems. Both colour and binary shape relationships (e.g. smaller width indicating stems) can be used (Humphries & Simonton (1993), Singh & Montemerlo (1997)). Wang et al. (1998) identified sugarcane shoots using the Hough transform and Zhang et al. (1998) graded tobacco leaves using a colour transformation that simulated human colour vision.

### 2.2.3 Plant sensing of specific morphological features

#### 2.2.3.1 Leaf description and species identification

Automatic leaf shape analysis and identification is used in site-specific pesticide application, biological growth analysis and biodiversity databasing. The soil/foliage segmentation methods and issues described in Section 2.2.1 also apply to automatic segmentation of outdoor crop seedlings in species identification applications. The approach for classification of crop and weed typically involves the recognition of leaf shape, colour or a combination of both.

Tang et al. (2000) described segmentation of green weeds using visible colour under natural lighting conditions. Alternatively, significant discriminatory wavelengths between weeds and crop can be used in a classification model to achieve recognition (e.g. Vrindts & de Baerdemaeker (1997), Wang et al. (2001)). Tang et al. (2003) achieved differentiation between broadleaf and grass weeds using Gabor wavelets and an artificial neural network. Leaf extraction from background soil has also been investigated using genetic

algorithms (Neto, Meyer & Jones, 2006) and Elliptic Fourier leaf shape analysis (Neto, Meyer, Jones & Samal, 2006). McDonald & Chen (1990) considered the use of morphological operators applied to leaf images for discriminating plant species. Texture analysis of plant top views permitted plant identification by image texture properties such as homogeneity, structuredness and brightness (Shearer & Holmes, 1990).

Shiraishi & Sumiya (1996) used leaf properties such as colour, aspect ratio and circularity for leaf identification. However, Du et al. (2007) identified that environmental factors caused leaf colour to be of low reliability for species identification, so they only investigated shape features in the development of an automatic classifier. Their method was intended for biodiversity studies in plant populations and required detachment of the leaf from the plant so that a clear image of the leaf could be obtained.

In the laboratory environment, leaves were automatically segmented from the background soil using a colour transformation (Chien & Lin, 2002). Automatic leaf shape analysis also has application in biology, e.g. plant morphology studies (Kaminuma et al., 2004). Insitu sensing and modeling of leaf shape in vegetable seedlings has successively used Bezier curves (Chi et al., 2002) and the elliptical Hough transform (Chien & Lin, 2002) to identify leaves that were partly occluded.

#### 2.2.3.2 Fruit development and yield monitoring

Early vision systems for agriculture involved automation of fruit identification for harvesting, possibly because fruit was distinctly coloured and thus distinguishable from foliage (Tian & Slaughter, 1998). Jimenez et al. (2000) reported that vision systems based on shape were less sensitive to hue changes (e.g. variation in target object colour), but that shape analysis algorithms were more time-consuming. Jimenez et al. (2000) also recommended that techniques were required to be developed to reduce total occlusion rates of fruit to improve feasibility of automatic systems.

Vision systems that sense fruit may be used in conjunction with yield mapping algo-

rithms. Dunn et al. (2006) developed a GPS-enabled vision system to count fallen nuts in a macadamia plantation, and the parent tree was estimated by identifying the woody trunks of neighbouring macadamia trees using a near infrared filter. Adamsen et al. (2000) used digital images to count coloured pixels belonging to flowers in a crop, for the purpose of assessing plant growth and potential yield estimation.

### 2.2.4 Generation of 3D plant models

Plant modeling has recently become popular for the purpose of generating realistic-looking images and for agronomic purposes such as simulating and visualising the effect of particular physiological stresses on the plant. With the advent of L-systems (Room & Hanan, 1995), complex plant structures and plant development rules can be represented effectively in a computer model, enabling simulation of individual plants and whole fields. Plant topography and geometry is traditionally input by either the manual operation of mechanical articulated arms with electromagnetic or acoustic sensors to detect arm joint 3D-world positions or by using laser scanners to generate point clouds of plant material surfaces (Room & Hanan, 1995).

Stereoimaging has also been investigated as potentially capable of automatically digitising 3D plant structure. Ivanov et al. (1995) generated a 3D reconstruction of a maize canopy using stereoimages. However, in this case leaves were removed to collect photographs necessary for the reconstruction algorithm and the method was inappropriate for routine or field measurement.

Chien et al. (2004) and Chien & Lin (2005) used three mutually perpendicular views (two sides and one top) of vegetable seedlings in a greenhouse to measure 3D plant structure including leaf area, leaf number and internode length. This enabled the generation of continuous growth curves under various conditions. The top view provided the most information but the side views permitted correction to leaf area estimation where leaves were tilted.

Non-destructive stereoimaging approaches include that of Takizawa et al. (2005), who

measured height, width and area of individual leaves of a pot plant using an automatic binocular system, and graphically reconstructed plants with Delaunay Triangulation. Quan et al. (2006) captured images of a plant from multiple viewpoints and correspondences between images were manually identified. Pan et al. (2004) created a semi-automated stereoscopic matching algorithm in which salient structures such as leaves were automatically identified by image processing and finer detail was input by a human operator. Andersen et al. (2005) generated 3D reconstructions of young wheat plants automatically from stereoimages. However, machine vision techniques suitable for automatic digitising of the 3D structure of mature plants have not been found in the literature.

## 2.3 Development of research objectives

On-the-go infield sensing of geometric crop plant parameters is currently limited to leaf shape identification and biomass estimation in the foliage of small plants, or plant height and biomass estimation in fully developed canopies. The desire to measure cotton plant internode length and potentially other topological features in maturing field plants will require the design of a robust outdoor machine vision system that achieves detailed stem structure sensing. These systems have so far only been reported for automated greenhouse systems on a limited number of crops under controlled lighting and environmental conditions. Hence, the specific objectives of this project are:

1. Develop a robust monitoring platform for non-destructive machine vision sensing of individual cotton plants under commercial conditions.

2. Develop an image processing algorithm for the identification of internode length and other plant geometric properties.

3. Evaluate the performance of the machine vision system under a range of crop and environmental conditions expected in commercial application.

4. Assess the potential to use the machine vision system for real-time control of irrigation application.

# Chapter 3

# Infield measurement system for cotton plant geometry

## 3.1 Fixed object plane geometry measurement

Machine vision sensing of plant geometric and topological attributes (e.g. internode length) requires access to individual plants in a developing crop canopy. This necessitates the design of an apparatus that enables each plant to be isolated, or at least discriminated from neighbouring plants. However, typical plant spacing in a cotton crop is one plant per metre across a row and 10–16 plants per metre down the row. Therefore, to simplify image capture and processing, an apparatus design that was able to operate (at least initially) across the row was considered preferable.

The natural flexibility of the plant's growing main stem was incorporated into the apparatus design concept (Figure 3.1). The conceptual apparatus featured a board mounted in front of a camera/s, which moved along the crop canopy. As the board moves through the canopy, it pushes over the flexible top of the plant such that only one plant is between the board and the camera at any time. Thus the captured images include only one plant, which can then be analysed to identify desired plant attributes.

Multiple cameras may potentially be installed on the infield measurement system, depending on the range of plant attributes that may be extracted from images collected with cameras featuring different settings such as optical filters, view angle or resolution.

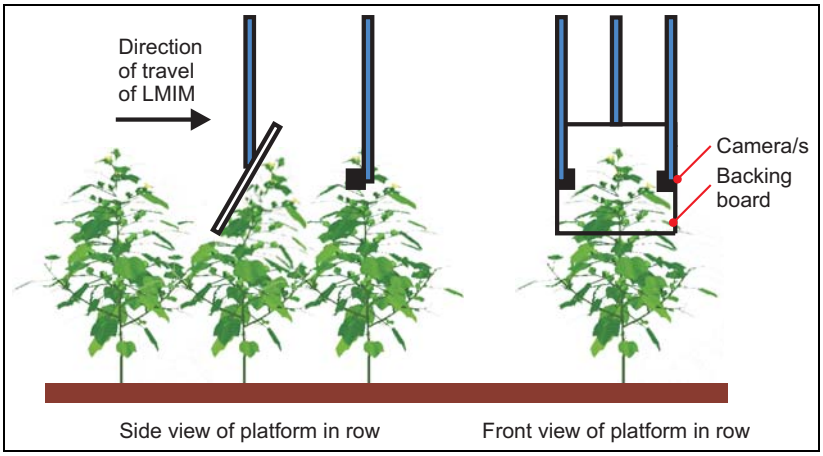


Figure 3.1: Initial concept for vision system apparatus. This concept evolved into the system displayed in Figure 3.2.

The design was further developed with the camera mounted inside an enclosure behind a transparent front panel (Figure 3.2). This design prevents other foliage from coming between the target plant and the camera. The camera enclosure firstly contacts the plant and then smoothly and non-destructively guides the plant under the smooth, curved bottom surface of the enclosure (Figure 3.3). Across-row motion of the camera enclosure is depicted in these figures but the camera enclosure may also move along the row, where the plants are more closely packed, in a similar fashion.

Further consideration of this design revealed another attractive feature. By forcing the plant into a fixed object plane (the transparent panel), reliable 2D geometric measurements could be obtained without the use of binocular vision.

Sections 3.2 to 3.6 discuss the development of the camera enclosure apparatus for infield vision sensing of cotton plant internode length. This is followed by manual (Section 3.7) and automated (Section 3.8) implementations of camera enclosure conveyance and a cost estimate for parts required to manufacture the camera enclosure unit (Section 3.9).

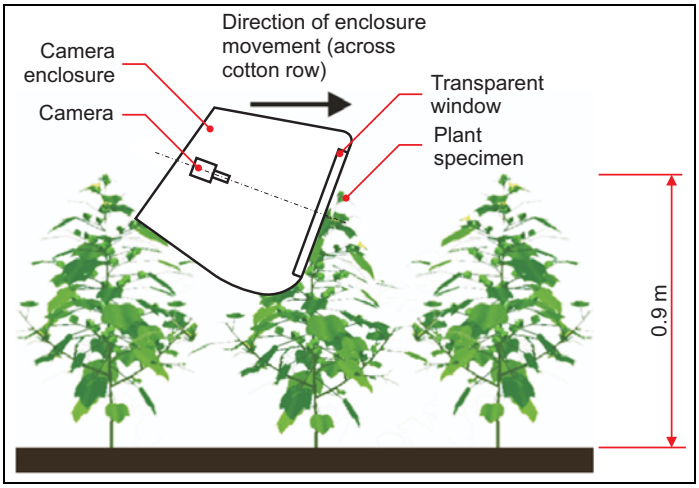


Figure 3.2: Moving image capture apparatus.

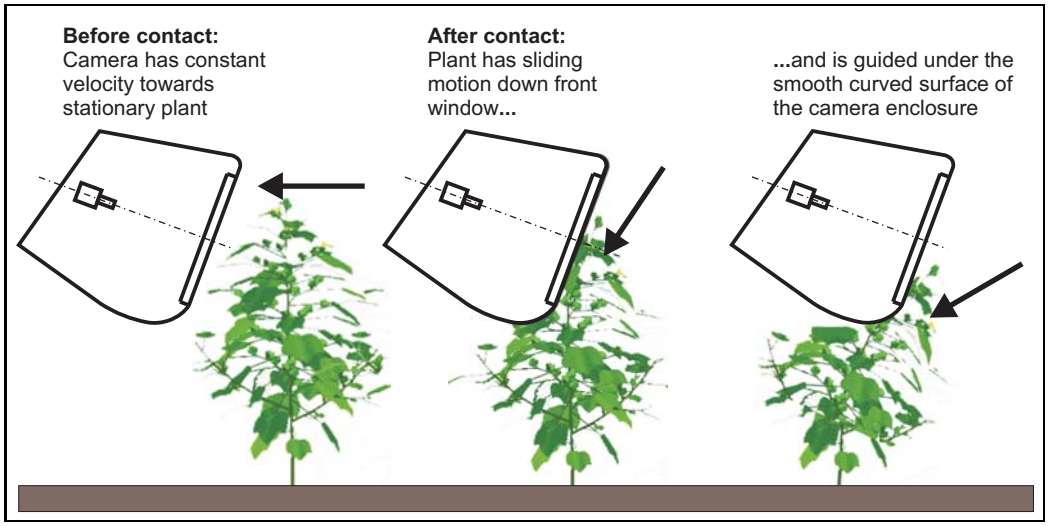


Figure 3.3: Motion of the plant with respect to the camera enclosure as the camera enclosure approaches, contacts and moves over the plant.

## 3.2 Camera enclosure designs and manufacturing process

The design of the camera enclosure evolved over four versions (Marks 1 to 4) throughout the research (Figure 3.4, Table 3.1). Marks 1 and 2 were for preliminary evaluations and Marks 3 and 4 were used in the 2005/06 and 2006/07 trial seasons, respectively.

The enclosures were constructed of fibreglass. The moulds consisted of chipboard cutouts for the two sides. Sheets of 0.6 mm galvanised mild steel were shaped and nailed to the side edges to form the curved parts of the top and bottom surfaces (Figure 3.5). The back surfaces of the enclosures were removable panels that allowed access to the interior of the enclosure (Figure 3.4). Mounting bolts were built into either side of the camera enclosure.

The front glass window (safety glass, 6 mm thick) was held in place in Marks 1 and 2 by internal aluminium brackets along the top and bottom edges of the window opening and in Marks 3 and 4 was set in a wooden frame spanning the front of the enclosure. The wooden frame was screwed in place for Mark 3, but for Mark 4 was hinged to allow access to the lighting wiring inside the camera enclosure. In each of the camera enclosures, a SI scale was affixed to the glass panel to enable interpretation of pixel measurements at the window surface. Marks 3 and 4 featured artificial illumination at the front window and the interior space under the window was used to store a 12V lead-acid battery to power the lights. The camera used in each enclosure was a Sony DV camcorder (model TRV19E) with wide angle lens (camera settings for this application are discussed in Section 4.2 in Chapter 4).

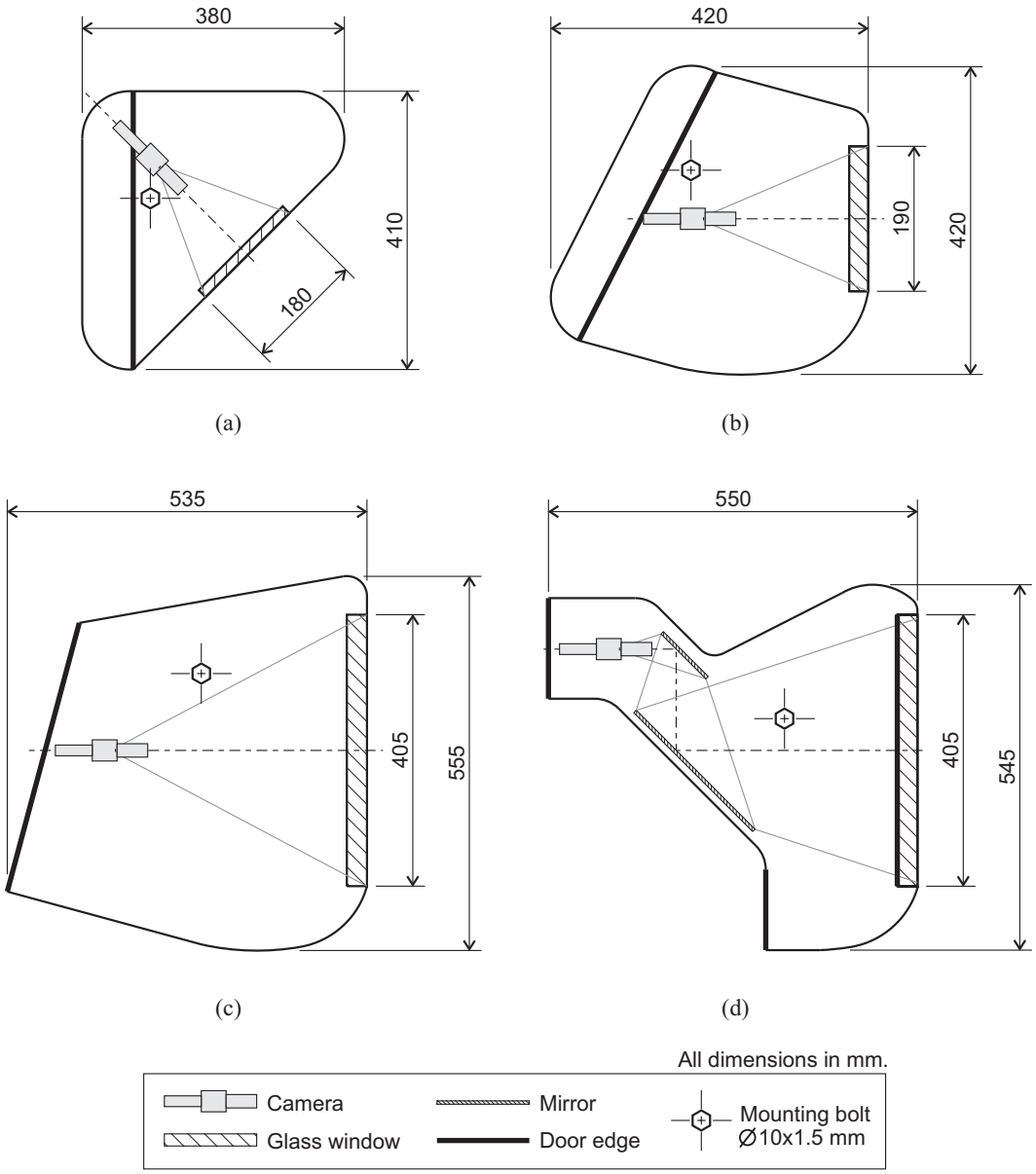


Figure 3.4: Vertical section view of camera enclosure designs, with lines projected between the camera and window indicating the camera's focal path and field of view: (a) Mark 1; (b) Mark 2; (c) Mark 3; and (d) Mark 4 (without sun visor).

Table 3.1: Feature dimensions of camera enclosure prototypes.

| Mark no. | Window area (mm × mm) | Working distance (mm) | Focal length* (mm) | Enclosure depth (mm) | Enclosure mass (kg) |
|---|---|---|---|---|---|
| 1 | 180 × 175 | 135 | 2.5 | 265 | 5 |
| 2 | 190 × 220 | 202 | 3.6 | 265 | 5 |
| 3 | 405 × 205 | 356 | 3.0 | 270 | 6 |
| 4 | 405 × 205 | 554 | 4.6 | 270 | 7 |

*calculated with equations of Section 3.5.3 using Sony camcorder specifications

(a) (b) (c)

Figure 3.5: Stages of manufacture of fibreglass camera enclosure (Mark 3): (a) mould constructed of chipboard and aluminium; (b) fibreglassed shell with wooden frame containing halogen globes at front; and (c) back view of (b) showing mounted camera. The glass window has not yet been mounted in these images.

## 3.3 Camera enclosure Marks 1 and 2: preliminary designs

Mark 1 featured a flat surface from the bottom of the window to the front edge of the enclosure base (Figure 3.4(a)). The plant motion induced by Mark 1 was observed on glasshouse-grown cotton plants and used to identify desirable enclosure shape features. A pronounced curve originating at the base of the window and continuing to the back of the camera enclosure was deemed necessary to provide support for the plant as it moved smoothly under the enclosure.

A smoothly-curved enclosure base was included in the design of Mark 2 (Figure 3.4(b)). The glass window of Mark 2 was approximately square (Table 3.1) and the camera was mounted to capture images in landscape orientation. However, the window was not sufficiently tall to enable the image capture of the top five nodes of the plant in a single frame. There was no damage observed to the plants as a result of contact with the camera enclosure.

## 3.4 Camera enclosure Mark 3: apparatus for 2005/06 fieldwork

Mark 3 was an elongated camera enclosure (Figure 3.4(c)) in which the top five nodes of a cotton plant in front of the enclosure could be viewed simultaneously through the window. The camera was mounted on its side so that the captured images were in portrait orientation, which allowed the top of the plant to be visible in a single captured frame. The purpose of this modification was to simplify the image processing.

The curvature in the base of Mark 3 mimicked the shape of Mark 2. Artificial illumination in Mark 3 was provided by halogen globes ($6 \times 10$ W) that were equally distributed along the vertical edges of the window. The globes were mounted outside the window to prevent light reflections inside the camera enclosure from degrading the image. However, visual inspection of typical imagery demonstrated that this illumination was washed out by sunlight (Figure 4.1 in Chapter 4).

## 3.5 Camera enclosure Mark 4: apparatus for 2006/07 fieldwork

Mark 3 field data from the 2005/06 cotton growing season was used to develop the image processing algorithms (Chapters 4 and 5). However, by the 2006/07 cotton season, algorithm development was continuing and ongoing camera enclosure modifications were expected to potentially enhance the quality of the captured images. Hence, the following design modifications were incorporated into Mark 4 for the 2006/07 cotton season and are discussed in the following sections:

- increased focal length by folding the light path through mirrors (hence, the streamlined camera enclosure shape in Figure 3.4(d));
- near infrared LED illumination for night-time sensing;
- implementation of a narrow depth of field (DOF) via a second camera with a custom lens; and

- addition of a sun visor to the front of the camera enclosure.

### 3.5.1 Extending the focal length with mirrors

Mark 4 of the camera enclosure featured mirrors to extend the focal length of the imaging system, a factor conducive to the achievement of a narrow DOF and to reduced geometrical distortion. A two-mirror system was used so that the sensed image was a non-inverted representation of the scene.

The design constraints for the two-mirror system were:

- the largest mirror size that could be sourced conveniently was 300 mm square; and
- for compatibility with the Mark 3 camera enclosure, the desired window height was 405 mm.

The following three dimensions could be varied:

- the horizontal distance between the bottom mirror and the window;
- the vertical distance between the two mirrors; and
- the horizontal distance between the camera and the top mirror.

A design was chosen to meet the given constraints. The lengths of the top and bottom mirrors were 92 mm and 245 mm, respectively. Both mirrors were 245 mm wide to fit comfortably inside the camera enclosure, allowing space for supporting brackets. The mirrors increased the vision system's working distance between the camera and the window from 356 mm for Mark 3, to 554 mm for Mark 4 (Table 3.1).

### 3.5.2 LED array illumination

The 2006/07 fieldwork included an evaluation of the vision system under a range of operating conditions, including night time. Therefore, a LED illumination scheme featuring white and near infrared LEDs was devised to replace the halogen globes of Mark 3 (Figure 3.6). The scheme consisted of a LED array mounted along the top and bottom edges of the camera enclosure window with each array holding a row of 850 nm, 940 nm and white LEDs. The LEDs were siliconed into an acrylic base (Figure 3.7). Appendix B contains electronic circuit details for the LED implementation.

The different LED types were individually operated by separate power switches. Isolated circuits for powering different wavelengths of illumination were considered more convenient than manually fitting filters to the camera. The LED wavelengths of 850 and 940 nm were selected because they allowed comparison of reflectances in the near infrared spectrum (i.e. water absorbing bands, Section 1.4.2) and were conveniently sourced online (Appendix B).

A comparison of the white LED (Mark 4) and halogen (Mark 3) lighting systems is included in Table 3.2. By inspection of images captured in comparable daylight conditions (e.g. Figure 6.3(b) for white LEDs and Figure 6.4(b) for halogen globes in Chapter 6), both halogen and white LED lighting systems were washed out at the centre of the image in daylight conditions. However, the white LED system cast more light onto plants in front of the window (i.e. at the horizontal edges of the window) than did the halogen system and caused reflections along the horizontal edges of the window area. The difference in incident light on the plants outside the window between lighting systems is believed to be principally the result of the white LEDs being positioned inside the camera enclosure. Further evaluation results for the lighting systems are provided in Chapter 6.

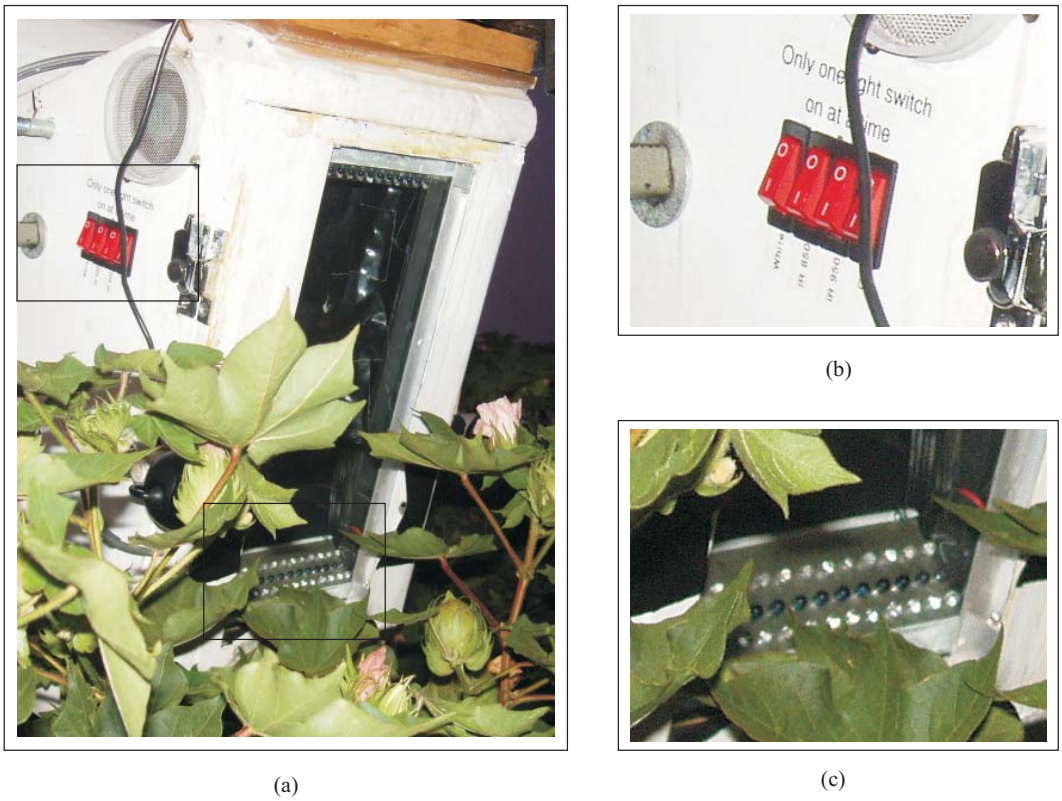


Figure 3.6: LED illumination for camera enclosure Mark 4: (a) camera enclosure in field; (b) power switches for each light source; and (c) three rows of LEDs, with top, middle and bottom rows corresponding to white, 850 nm and 940 nm LEDs, respectively. Images (b) and (c) are enlarged from the outlined regions in (a).

Figure 3.7: One row of LEDs installed in the hinged front window of Mark 4.

Table 3.2: Comparison of implemented white LED and halogen lighting systems.

| Lighting system | Halogen | White LED |
|---|---|---|
| Number of globes | 6 | 36 |
| Power of each globe | 10 W | 0.15 W |
| Luminous flux per globe | 140 lm | 1.15 lm |
| Colour temperature | 3000°K ('warm white', i.e. yellow glow) | 7000°K ('cool white', i.e. blue hue) |
| Globe positioning on camera enclosure | Evenly distributed along outside of vertical edges of window | Evenly distributed along inside of horizontal edges of window |

### 3.5.3 Lensing for a narrow depth of field (DOF)

An attractive feature of the camera enclosure measurement concept was that the foliage was forced into a fixed object plane. The images obtained by this method were expected to be further enhanced by implementing a narrow DOF, in which the region immediately behind the window was in focus and the background further behind the window was out of focus. In this case, image processing techniques (e.g. edge detection) could be tuned to have a reduced sensitivity to the blurry background and hence increase the confidence in feature detection at the fixed object plane.

An additional camera was mounted in the enclosure next to the Sony camcorder for the purpose of implementing a narrow DOF. The second camera was a Prosilica (www.prosilica.com) firewire camera (model EC750C, 1/3-inch CMOS image sensor, 752 × 480 pixels), fitted with a Tamron (www.tamron.com) varifocal, manual iris lens.

The size of the lens was calculated using equations for DOF, with parameters illustrated in Figure 3.8. The equation for the near and far bounds relative to the imaging plane, $D_N$ and $D_F$ respectively, on the DOF is (Larmore, 1965):

$$D_N = \frac{sf^2}{f^2 + Nc(s-f)} \tag{3.1}$$

$$D_F = \frac{sf^2}{f^2 - Nc(s-f)} \tag{3.2}$$

where $f$ = focal length (mm);

$N$ = f-stop number (e.g. 1, 1.4, 1.8, 2, 2.8, ...);

$s$ = lens-to-object distance (mm) (Table 3.1); and

$c$ = circle of confusion, a parameter that specifies the amount of blurring (mm).

The values $f$ and $c$ are calculated from:

$$f = (\text{sensor size}) \times (\text{working distance}) \div (\text{field of view}) \tag{3.3}$$

$$c = 0.025 \div \left( \frac{\text{35 mm equivalent lens focal length}}{\text{actual lens focal length}} \right) \tag{3.4}$$

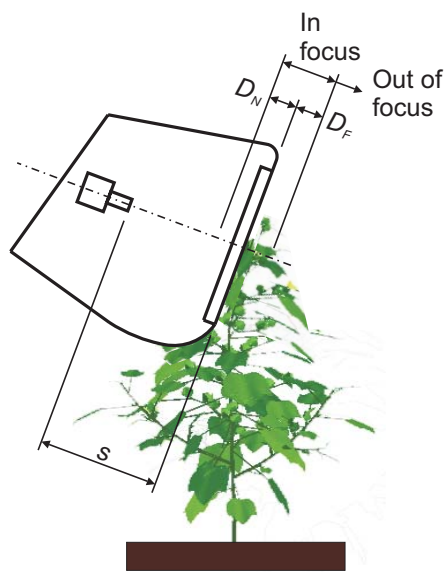


Figure 3.8: DOF parameters in camera enclosure.

In the present application, $D_F$ refers to the region of sharpness outside the camera enclosure. A suitable value for $D_F$ was calculated by substituting different values for $N$ into Equation 3.2. The required Tamron lens size was calculated to be $f = 6.2$ mm with $N = 1$, to give a $D_F$ value of 27 mm. This is the minimum theoretical $D_F$ for the possible range of $N$ values. However, a small DOF implies but does not guarantee the extent of blurriness in background objects (Larmore, 1965).

Altering the f-stop number ($N$) for DOF adjustment changes the aperture diameter and the amount of incident light on the image sensor. Hence, the shutter speed was

required to be decreased to compensate for the increased amount of incoming light caused by decreasing the f-stop number and decreasing the DOF (Section 6.4.4).

Field images were captured simultaneously with the Sony camcorder and the Prosilica firewire camera. Inspection of images captured with the narrow DOF (e.g. typical images displayed in Figure 6.7 of Chapter 6) revealed that the background was indeed more blurred than the window area, but the effect was not pronounced. This was believed to be because the image background was physically close to the window.

### 3.5.4 Sun visor and shroud

Variations in sunlight conditions observed during 2005/06 fieldwork with Mark 3 led to the development of a sun visor for Mark 4 (Figure 3.9(a)), in an effort to create more uniform images irrespective of sunlight conditions. Visual inspection of imagery collected with the sun visor revealed no particular reduction in the amount of sunlight incident on the plants. This was expected as the sun visor did not cast a shadow much larger than the shadow already cast by the camera enclosure as it contacted the plant. The sun visor was not sufficiently expansive to block the sun at low angles or to soften the intensity of the sunlit background.

Covering the sun visor with a black cloth shroud (Figure 3.9(b)) was not practical for field use, since the shroud was prone to becoming caught in the canopy and affecting image capture (Figure 3.9(c)).

### 3.5.5 Other possible modifications

Other Mark 4 modifications that were considered but not evaluated were: an additional low-resolution camera facing perpendicular to the window surface, for the purpose of measuring the offset of the main stem from the window (for potential geometric correction); and an air blower system with air outlets at the window for ruffling foliage and reducing occlusion of the stems by the foliage.

(a) (b) (c)

Figure 3.9: Sun visor and shroud for camera enclosure: (a) sun visor mounted on camera enclosure; (b) shrouded sun visor; and (c) captured image from the enclosure, with the shroud caught in front of the plant.

## 3.6 Required degrees of freedom for camera enclosure conveyance

The following dynamic movements were necessary to the camera enclosure's position and orientation during field measurements (Figure 3.10):

- **traversal**, the horizontal displacement of the camera enclosure with respect to the plant, to convey the enclosure across or along the crop rows;
- **pitch**, the up/down angle of enclosure rotation around the horizontal axis, which affects how the contacting plant rests against the front window (typically held constant for a single set of canopy measurements, Figure 3.11);
- **yaw**, the rotation about the enclosure's vertical axis, which affects whether the plant bends under the camera enclosure or shears across the enclosure window (Figure 3.12); and
- **height** adjustment as required for different crop sizes.

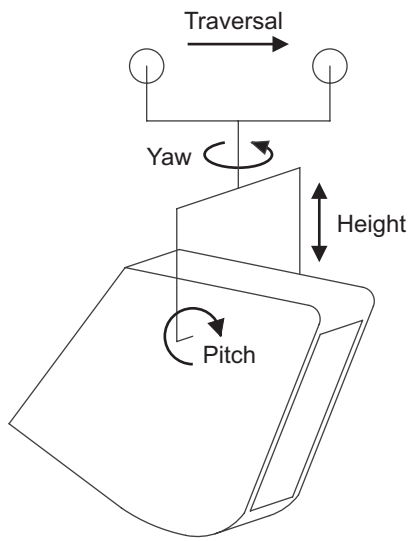


Figure 3.10: Required degrees of freedom for quad-axis drive system from which the camera enclosure is suspended.

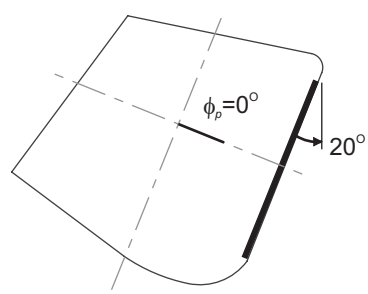


Figure 3.11: Side view of camera enclosure illustrating pitch angle $\phi_p$.

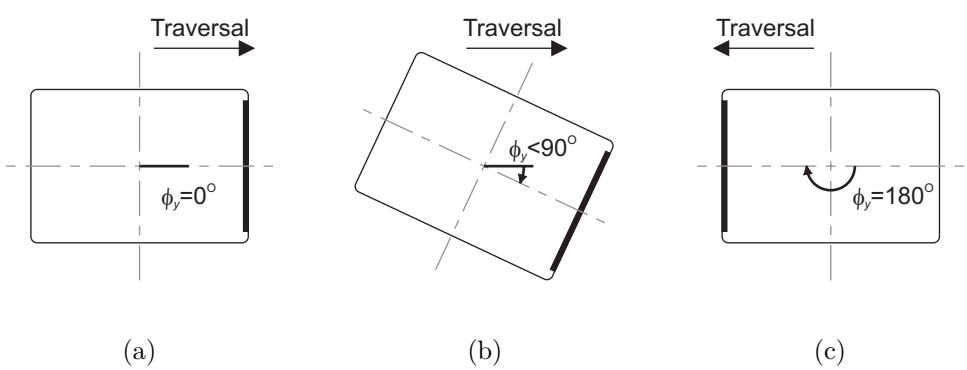


Figure 3.12: Top view of camera enclosure illustrating effect of yaw angle $\phi_y$: (a) 0°: enclosure pushes over plant; (b) $<$ 90°: enclosure shears past plant; and (c) 180°: camera enclosure faces opposite direction to (a).

The camera enclosure was suspended from a quad-axis drive system and gantry for movement across the plants in the field. The following two sections discuss manual and automated implementation of the enclosure's conveyance.

## 3.7 Manual conveyance of camera enclosure (2005/06 fieldwork)

The manual quad-axis drive system was implemented by suspending the camera enclosure from sliding door rollers and matching sliding door rail (Figure 3.13). This allowed the camera enclosure to be pulled along the rail across the plants. Between the sliding door rollers and camera enclosure was a pin joint that enabled rotation of the camera enclosure about its yaw axis. The sliding door rail (3 m) spanned an effective operating length of one row width (1 m) and was supported on either end by a pair of star posts, pin-jointed at the top to form an A-frame (Figure 3.14). The camera enclosure height was adjusted by opening or closing the base of the A-frames, or via the worm drive on the vertical rods on either side of the camera enclosure.

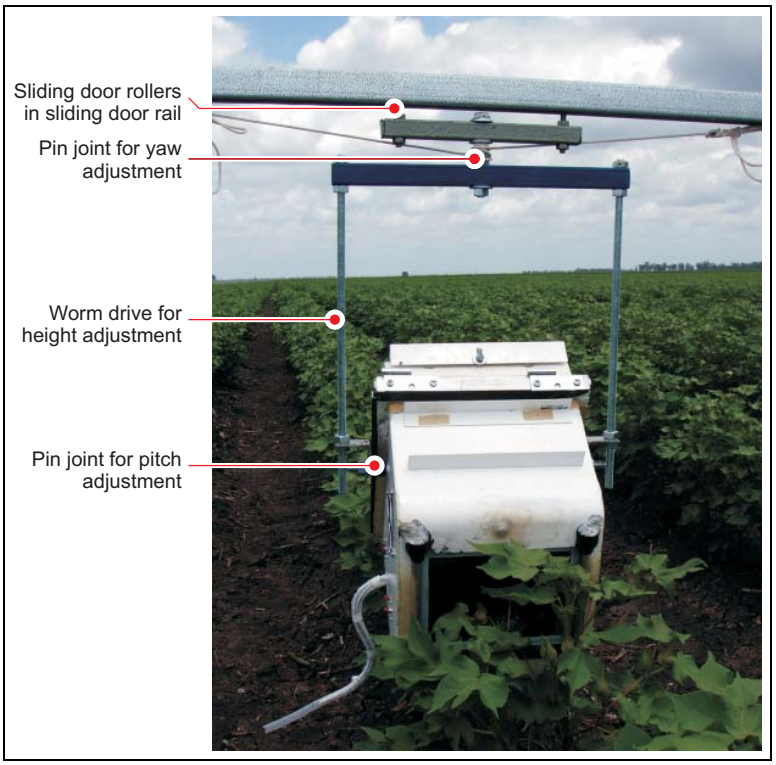


Figure 3.13: Mechanical joints for camera enclosure's manual conveyance.

Figure 3.14: Manually moved camera enclosure in a cotton crop.

## 3.8 Automatic conveyance of camera enclosure (2006/07 fieldwork)

A four-wheeled chassis supporting a camera enclosure boom which spanned three cotton crop rows was designed and constructed to allow for automatic movement of the camera enclosure (Figure 3.15; major dimensions in Appendix B). The automatic conveyance of the camera enclosure imitated an envisaged operation of the vision system where the camera enclosure may be mounted from a boom of a centre pivot or sprayer. While the manual apparatus was placed individually about each plant, the automatic apparatus spans multiple rows and hence, may need to deal with variations in plant height and position from row to row. It is anticipated that further system development (e.g. adaptive camera enclosure height) will cater for row to row variations.

Figure 3.15: Automatic conveyance of camera enclosure in a cotton crop.

### 3.8.1 Automated quad-axis drive system

Windscreen wiper motors (12V) were used to motorise the traversal, yaw and height adjustments of the quad-axis drive system (Figure 3.16), as well as the chassis' propulsion along the crop rows. The pitch joint was not motorised since this adjustment was only required once per data collection session.

Figure 3.16: Mechanical joints for camera enclosure's automatic conveyance. A mechanical drawing of the drive system is included in Appendix B.

The traversal movement was implemented using a pair of 200 mm trolley wheels that moved along a 50 mm steel channel (two lengths of angle steel welded together to make a U cross-section). Anti-skid tape (as commonly used on steps) was applied to the inner bottom surface of the boom rail to prevent the wheels from slipping. Worm drives on either side of the camera enclosure were used to adjust the camera enclosure's height via two pulleys and a belt. The yaw rotation was implemented with a bicycle chain. The propel motor was geared 4:1 using a standard-sized bicycle chain and sprockets.

Limit switches were necessary for the yaw and boom traversal motors, so that the camera enclosure remained on the boom, and accurately turned to face the opposite direction without overshooting and causing twisting and breakage of electrical wiring.

### 3.8.2 Control panel for chassis motors

Operator control of the motors was implemented via a panel of electrical switches (manual motor control) or alternatively via software on a PICAXE microcontroller (automatic motor control) (Figure 3.17), with the control signals being input to H-bridge motor drivers (Appendix B). The microcontroller implemented an algorithm which sequentially activated the motors such that the camera enclosure traversed across the boom, turned around, and then waited while the chassis advanced down the row for a few metres (Table 3.3). A block diagram of the motor control electronic circuit is in Figure 3.18 and a schematic circuit diagram is included in Appendix B. The system was powered by a 12V car battery with solar panel charging. An external monitor with camera output next to the control panel permitted a live preview of the camera enclosure's view.

Each motor had independent settings for automatic and manual control. This enabled flexibility in apparatus movement during data collection. For example, if the 'propel' motor was in manual OFF mode while the other motors were in automatic (program) mode, the camera enclosure traversed back and forth over the same plants without the chassis advancing down the row.

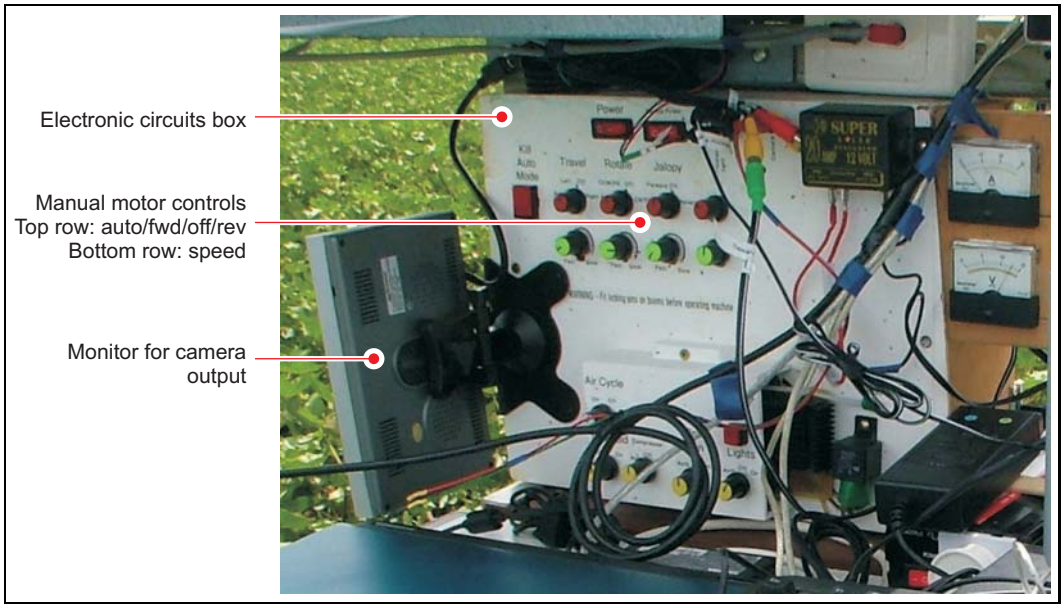


Figure 3.17: Electrical control panel for chassis motors.

Table 3.3: PICAXE program steps.

**PICAXE program to control camera enclosure conveyance in automatic (program) mode**

The camera enclosure's initial position is the left end of the boom, facing the right end, as in Figure 3.15.

1. Activate 'traversal' motor until boom limit switch (right end) is activated.
2. Activate 'yaw' motor until rotational limit switch (clockwise) is activated.
3. Activate 'propel' motor for specified time, corresponding to $x$ metres.
4. Activate 'traversal' motor until boom limit switch (left end) is activated.
5. Activate 'yaw' motor until rotational limit switch (counterclockwise) is activated.
6. Activate 'propel' motor for specified time, corresponding to $x$ metres.
7. Return to Step 1.

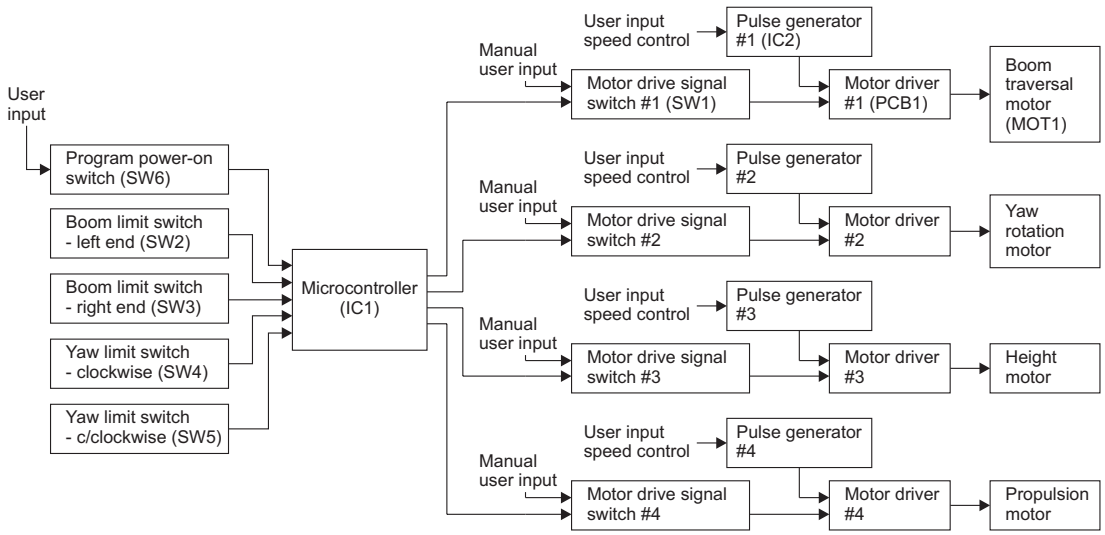


Figure 3.18: Block diagram of motor control circuit for automated conveyance of the camera enclosure. The bracketed symbols refer to electronic component labels of the schematic circuit diagram in Figure B.4 of Appendix B.

### 3.8.3 Transport of chassis

The chassis was designed to fit in a standard trailer to enable convenient road transport between the workshop and trial sites. A 12V, 680 kg winch was bolted to the front of the trailer and was used to pull the chassis onto the trailer (Figure 3.19). The camera enclosure remained suspended from the boom during road transport but was securely tied down to prevent swaying.

Compactness of the chassis was achieved by designing the outer lengths of the boom to be removable. The boom lengths that spanned the outer two crop rows were joined by hinges and highfield levers onto the chassis, which enabled removal of the boom ends during transport and storage of the chassis.

The boom height was adjustable to be either raised or lowered via a pair of hydraulic jacks (each 1850 kg, 165 mm) on the back vertical posts of the chassis. The boom was required to be in the raised position for data collection at the trial site. The lowered boom position was used for transport and storage of the chassis, since the combined

height of the trailer and chassis was designed to fit under a 2.1 m garage door when the boom was lowered.

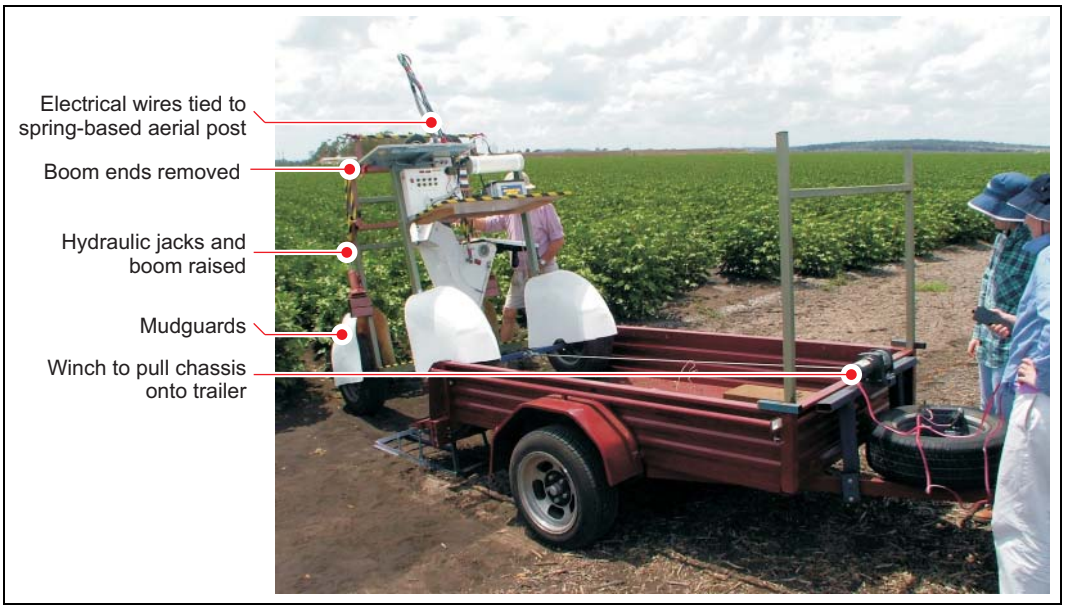


(a)

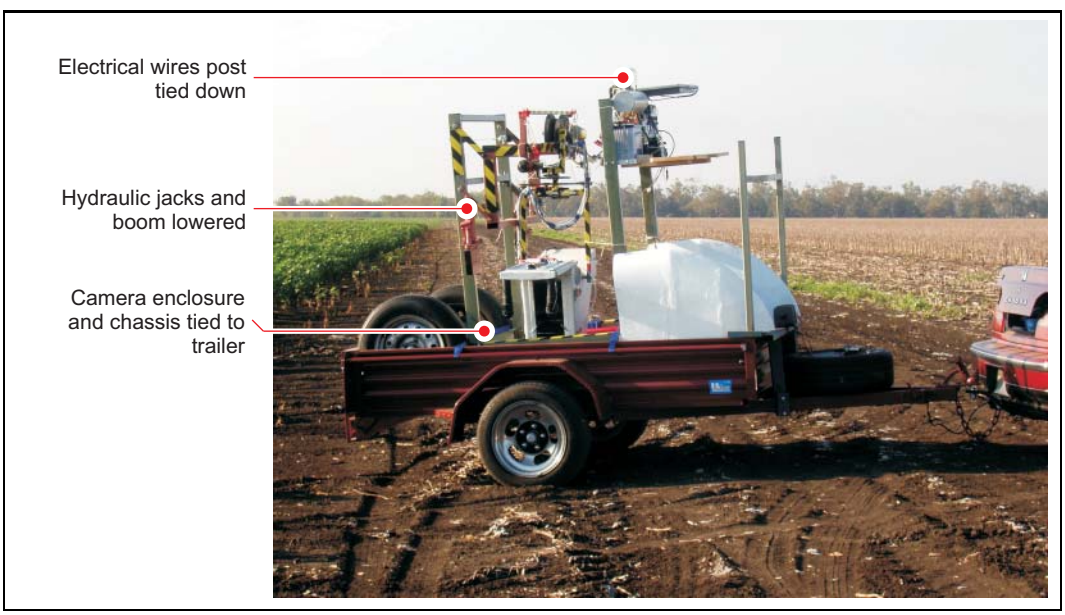


(b)

Figure 3.19: Chassis road transport by trailer: (a) chassis being winched onto trailer; and (b) chassis loaded onto trailer.

## 3.9 Cost estimate for camera enclosure

An overall cost estimate for the hardware required to manufacture the camera enclosure and quad-axis drive system are provided (Table 3.4, labour not included). Those parts that are considered necessary for mounting a single camera enclosure on a large mobile irrigation machine (LMIM) are included. Hence, cost estimates for the automated chassis are not included.

The costs are indicative only and are not representative of a commercial product. The large-scale manufacture of the unit would be expected to reduce the cost of component parts.

Table 3.4: Cost estimate for camera enclosure hardware as at January 2007.

| Component | Estimated cost |
|---|---|
| Camera | 800 AUD |
| Quad-axis drive system (windscreen wiper motors, steel, wheels, bicycle sprockets and chains) | 200 AUD |
| Electronics for motor control | 300 AUD |
| Enclosure (fibreglass and glass window) | 200 AUD |
| Embedded image processing hardware | 2000 AUD |
| **Total** | 3500 AUD |

# Chapter 4

# Image processing for a single frame

## 4.1 Introduction

The cotton plant structural parameter of internode length has been identified as a desirable measurand for cotton water stress (Chapter 2) and cotton plant images were collected using a custom built infield machine vision system (Chapter 3). However, automatic measurement of internode length requires discrimination of plant features such as leaves and stems from collected field images (see a typical image in Figure 4.1). This is complicated in field images since green and red stems are required to be discriminated from green leaves, and since in any particular frame, there are leaves and stems from neighbouring plants as well as the target plant (plant spacing along cotton crop rows is 10 to 16 plants per metre). Therefore, the image processing is required to account for leaf edges and branches of neighbouring plants, and also occlusion of essential points of geometry by plant foliage such as leaves.

This chapter begins with an overview of the image sequences used in the image processing evaluations (Section 4.2) and a discussion of geometric measurement from main

Figure 4.1: A typical full-scale deinterlaced image for analysis.

stem node positions (Section 4.3). A description of the standard image processing techniques considered for automated detection of nodes follows (Section 4.4). These techniques (i.e. thresholding, edge detection and matched filtering) were then evaluated (Sections 4.6 to 4.8) but found to be not viable for real-time identification of nodes in outdoor imagery. However, the 'vesselness' function of the Hessian matrix eigenvalues was found to be effective (Section 4.9). Once branch segments of the plants are reliably extracted, line-fitting techniques to yield accurate node localisation on the main stem are discussed (Sections 4.11 and 4.12.2), and the efficacy of the overall method is considered (Section 4.13).

## 4.2 Evaluation image sequences

Several data sets of cotton plant video footage were collected with the machine vision system, under a variety of field and environmental conditions. The apparatus configurations tested were the camera enclosure approach and yaw angles[1] (Figure 6.1), camera enclosure speed and illumination, and the agronomic factor evaluated was crop variety (Chapter 6). To enable verification of the measurement technique, the top five internode lengths (Figure 4.2) of the plants that were automatically measured by the camera enclosure were manually measured in the field (using a ruler). Internode lengths ranging from 12 to 115 mm were observed. Manual measurements were also made of plant height (using a tape measure), stem diameters of the top five internodes (using calipers), nodes above white flower, retention of first-position fruit on the top five nodes, number of fruiting branches and plant spacing.

A Sony TRV19E camcorder (www.sony.com.au) with a wide angle lens and 1/4-inch image sensor was used to collect the video images. Interlaced image size was 720 × 576 pixels. Deinterlacing the image produced pixel dimensions of 720 × 288 pixels, which corresponds to a frame aspect ratio of 5:2. The images were RGB with 8-bit colour depth. Hence, each image pixel was represented by 256 shades each of red, green and

[1] the angle of rotation about the camera enclosure's vertical axis

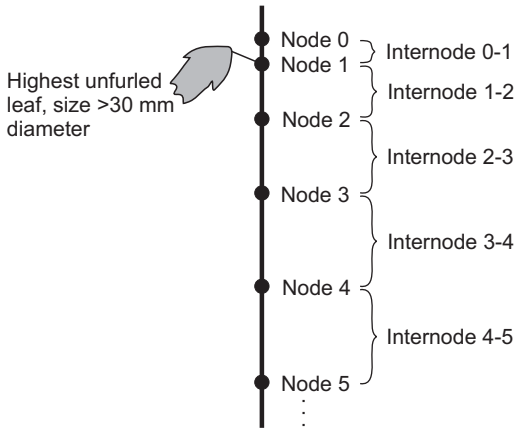


Figure 4.2: Diagrammatic representation of node numbering on a plant, with the vertical black line representing the plant's main stem.

blue colour levels.

Deinterlaced image resolution at the transparent panel was found to be 1.0 pixels/mm in the horizontal direction and 0.6 pixels/mm in the vertical direction (with the camera mounted in 'portrait' orientation and hence, a vertical raster scan). This was calculated by comparing pixel locations of window scale marks in the image (Figure 4.1). The camera settings were left in automatic mode, except for focus which was set manually to the window scale marks. Zoom was adjusted such that the window area extended to the vertical image boundaries. The barrel distortion apparent in the sample image was found to be minimal (less than 0.5 mm, found by evaluating the scale for different vertical slices of the image). The video was recorded onto DV tape, and then downloaded via the camera's firewire port into the video editing software Adobe Premiere, in which the video was divided into clips corresponding to a single pass of the camera enclosure over a single plant and digitised in AVI format. The Microsoft DV (PAL) codec was used at the 100% quality setting to create the AVI files from the camera's DV output signal. These files were then post-processed in custom image processing software written in Borland Delphi version 6. AVI-to-bitmap conversion was achieved in the software using the VideoLab 2.2.1 component library for Delphi (downloaded from Mitov Software, www.mitov.com).

Inspection of acquired imagery from different times of day and different camera enclo-

sure approach angles revealed that illumination of the target plant varied throughout a video sequence, and also varied as a result of the camera enclosure approach angle with respect to the solar angle. The amount of image contrast was low when the sun was behind the camera, and high when the sun was above or in front of the camera. However, typically branches oriented towards the camera enclosure fell into the camera enclosure's shadow when the camera enclosure was contacting the plant. By visual inspection, the halogen lighting evident in Figure 4.1 (at intervals along the window scale as discussed in Chapter 3) was largely ineffectual in the natural daylight.

The video data set used for algorithm development was for plant rows which were oriented east-west, such that the camera was perpendicular to the sun's direction (Data Set 1 of Table 6.1)(Figure 4.3). The video recording occurred in the mid-afternoon hours of 2 to 3pm, for plants (cultivar: 'Sicot 80B') ten weeks after planting. The principal source of illumination was natural sunlight, which was softened by cloud cover for the duration of video recording. This data set was selected since in these images the stems were easily visually discernible, and there were no hard shadows evident in images.

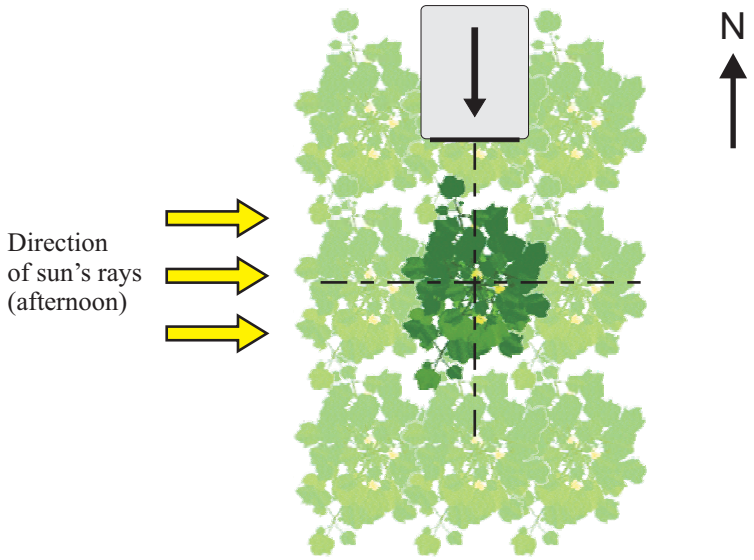


Figure 4.3: Plan view of the crop rows (east-west), the direction of the afternoon sun's rays and the camera and its optical axis.

Image processing techniques on a sample image from each of four sample sequences (labeled Sample Images 1 to 4) from the selected data set (Figure 4.4) are demonstrated

in the discussion of this chapter. These sequences (labeled Image Sequences 1 to 4) were chosen for the following reasons:

- **Image Sequence 1** featured many visible dark branches (red and green);
- **Image Sequence 2** featured a significant occlusion by a leaf;
- **Image Sequence 3** featured a branch that protruded away from the camera enclosure at the centre of the image and hence contained both light and dark significant branches; and
- **Image Sequence 4** contained light and dark stems (red and green) and a branch from another plant in the bottom half of the image.

The algorithm developed in this chapter (and extended to sequential frames in Chapter 5) is evaluated in Chapter 6 for video data sets containing different plant varieties and lighting conditions.

(a) (b) (c) (d)

Figure 4.4: Sample images from video sequences used for evaluating image processing techniques, cropped from original size for display purposes. Images (a)–(d) represent Sample Images 1 to 4 from Image Sequences 1 to 4, respectively. Image (d) corresponds to Figure 4.1.

## 4.3 Verification of measurements obtained with manual node identification

Plant geometry was manually measured from collected imagery so that the effectiveness and accuracy of automated measurement could be evaluated. As discussed in Chapter 3, the image capture apparatus (i.e. the camera enclosure) enabled geometric measurement of the cotton plant to be made without binocular vision. This was because the transparent panel at the front of the camera enclosure became a fixed object plane when the plant contacted the panel. Therefore, the equation derived below calculates 'apparent internode length' (i.e. internode length as seen by the camera at an arbitrary time instant in the sequence) from the pixel location of the nodes (as illustrated in Figure 4.5).

### 4.3.1 Internode length calculation

Let $\Delta x_{px}$ and $\Delta y_{px}$ be the horizontal and vertical pixel distances, respectively, between adjacent nodes $P_1$ and $P_2$ (in this example, nodes 4 and 5 of Figure 4.5(a)). To calculate the distance between points $P_1$ and $P_2$ in millimetres, $\Delta x_{px}$ and $\Delta y_{px}$ are substituted with $\Delta x_{mm}$ and $\Delta y_{mm}$, respectively, where $\Delta x_{mm} = \Delta x_{px} \cdot x_{res}$ and $\Delta y_{mm} = \Delta y_{px} \cdot y_{res}$, and $x_{res}$ and $y_{res}$ are the horizontal and vertical image resolutions, respectively. Then the apparent internode distance $L$ is given by:

$$L = \sqrt{(\Delta x_{px} \cdot x_{res})^2 + (\Delta y_{px} \cdot y_{res})^2} \,. \tag{4.1}$$

Alternatively $L$ is given by the following, in which $\Delta x_{px}$ is substituted with $\Delta y_{px} \tan\theta$, and $\theta$ is as defined in Figure 4.5:

$$L = \Delta y_{px} \sqrt{(x_{res} \cdot \tan\theta)^2 + {y_{res}}^2} \,. \tag{4.2}$$

The origin of the coordinate system used for image processing is illustrated in the top left corner of Figure 4.5(a), and is equivalent to $(x, -y)$ of a conventional Cartesian

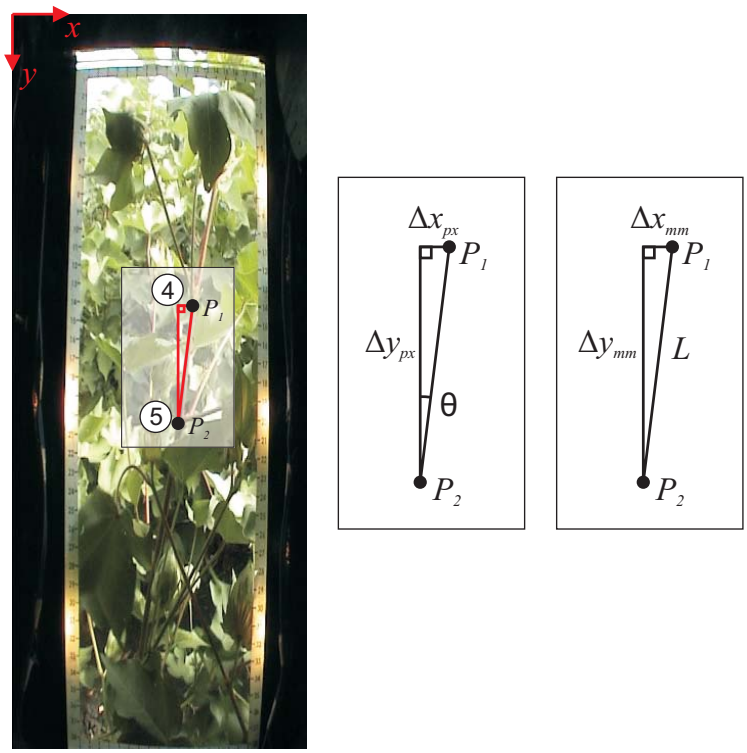


(a) (b) (c)

Figure 4.5: Calculation of apparent internode distance from a single frame: (a) nodes 4 and 5 (black circles) labeled on a sample image; (b) triangle from boxed region of (a) labeled for geometric analysis (pixels); and (c) triangle from (b) converted into millimetres to enable calculation of the internode length $L$.

system (in which $y$ points up), but is common for image processing coordinate systems. The window scale marks of Figure 4.5(a) are similarly annotated, with 1 to 18 (cm) from left to right in the horizontal direction, and 1 to 38 (cm) from top to bottom in the vertical direction. However, for illustrative purposes, graphs of node position (e.g. Figure 4.6) are plotted relative to the bottom of the image such that the bottom of the $y$-axis represents the direction closest to the ground.

Figure 4.6 shows a graph of node positions over time for a typical image sequence, in which the camera enclosure approached, contacted and moved over the target plant. The node positions in this graph were obtained using a simple software application written in Borland Delphi Version 6, which allowed the user to visually assess the position of nodes and click points (with a cursor) on each frame of a video clip, storing

the coordinates of all the clicked points. For the purpose of illustrating apparent node position as the camera enclosure approached the plant, the y-coordinate of identified nodes relative to the bottom of the image was then graphed for each time step in Microsoft Excel (Figure 4.6(a)).

Node positions in Figure 4.6(a) move down the image as a result of the plant sliding down and then beneath the camera enclosure (Figure 3.3 in Chapter 3). Not all nodes remain visible for the whole sequence, because the enforced motion of the plant caused transient occlusions as leaves moved into and out of the camera's line of sight to the node. The effect of perspective is also evident with the apparent distance *between* adjacent nodes increasing as the camera enclosure approached the plant (Figure 4.7). Logically, this apparent distance will increase to some maximum which coincides with the time instant when the plant is closest to the window (i.e. in contact with the glass), a fixed object plane. Hence, the maximum distance between successive node trajectories for an entire sequence of images is taken as the true internode distance for each plant.

In a distribution of measurements for a particular length $L$ this technique will unavoidably favour measurements with positive random error. This issue is considered further in Section 6.3.

### 4.3.2 Verification against physical measurements

The previous section provided a methodology for measuring internode length from the video imagery collected by the infield camera enclosure. Figure 4.8 shows that internode lengths calculated by this manual screen-based method (using 30 sequences in the control data set) have a correlation coefficient ($R^2$) of 0.97 when compared with internode lengths physically-measured on plants. The mean absolute error of measurements is 4.0 mm. Standard error in screen-based measurements was calculated for each physical internode length for which more than three readings were measured on-screen from the replicate video sequences. The standard error ranged from 0.7 mm to 2.6 mm, with an average of 1.4 mm. This compares with the uncertainty of the screen-

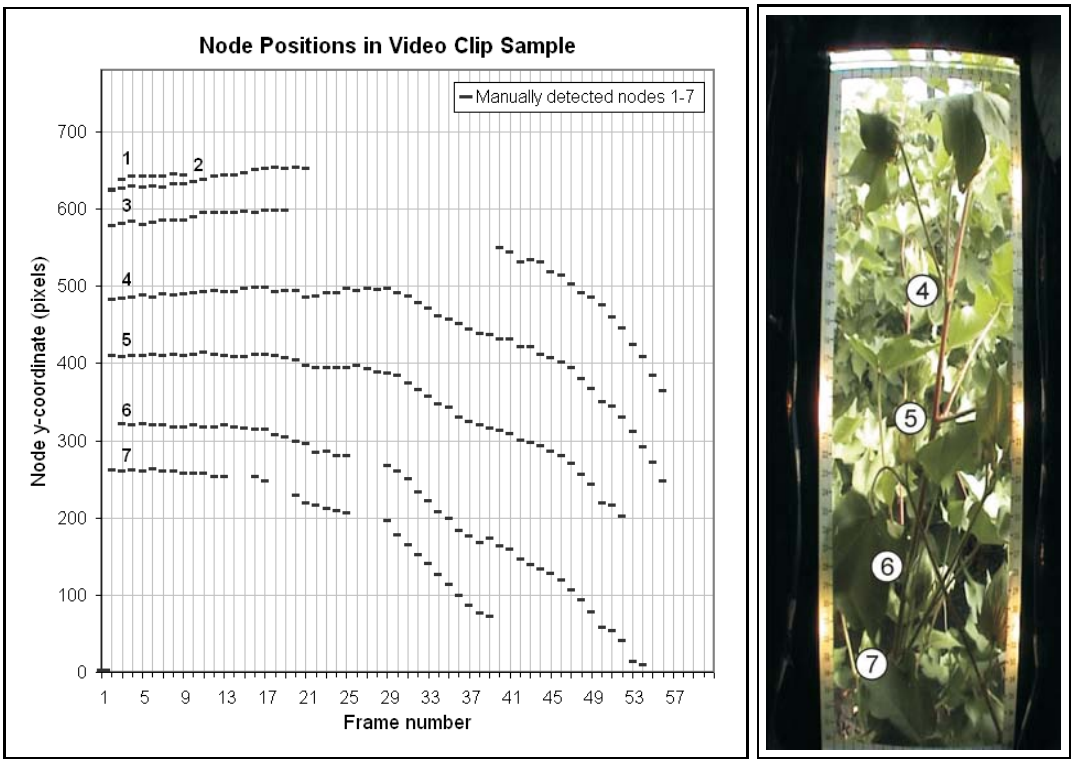


(a) (b)

Figure 4.6: Manual node identification from imagery: (a) graph of manually identified node positions for each frame of a typical image sequence; and (b) nodes identified (in numbered circles) for frame 38 of the sequence in (a).

based measurement of $\pm\frac{1}{2}$ pixel = $\pm 0.3$ mm and the uncertainty of the physically-measured values in the field of $\pm 0.5$ mm.

There is no obvious bias in the regression line graphed in Figure 4.8 since by visual inspection the screen-based measurements appear to be symmetrically distributed above and below the regression line. The regression equation has a slope parameter of less than one and a constant parameter of less than zero, which indicates that the screen-based method has a tendency to underestimate the physical measurement. This was judged to be caused by the plant's main stem not contacting the fixed object plane, but being held a distance off the transparent panel by other branching. This explanation was verified by field observations of the camera enclosure contacting and moving over the plant.

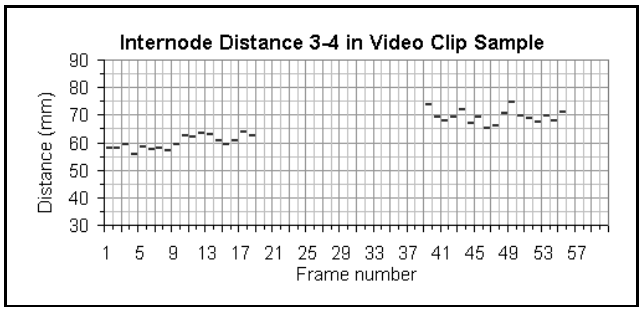


(a)

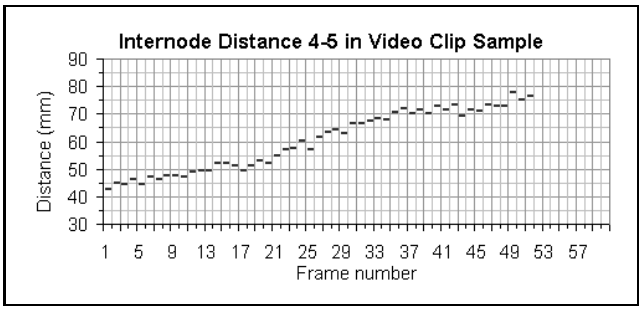


(b)

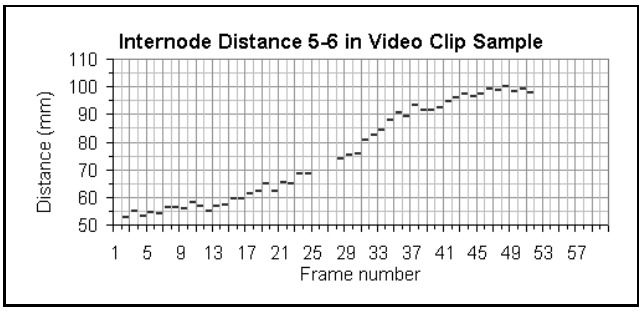


(c)

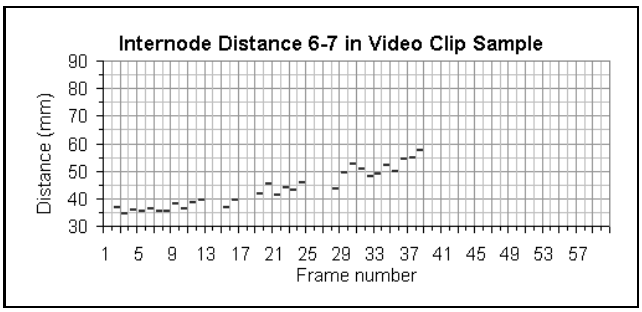


(d)

Figure 4.7: Apparent internode distances in imagery by manual identification of nodes, for image sequence of Figure 4.6.

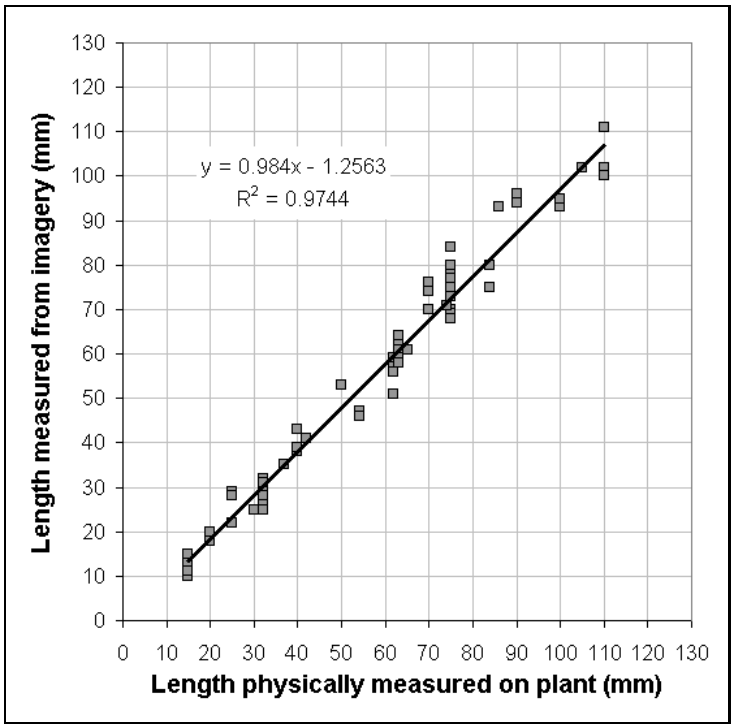


Figure 4.8: Internode length measurements by manual on-screen and physical methods, with a least squares regression line. Each point corresponds to a unique internode length measurement.

## 4.4 Approaches for automated node identification from imagery

Automated calculation of internode lengths from imagery requires identification of nodes (branch junctions). Two properties of node appearance have been identified that may be used to detect nodes with automated image processing:

1. Nodes visible on the main stem may be identified using the localised increase in main stem width and the presence of a branch junction on the main stem.

2. Nodes with adjoining branches partially visible may be identified using line-finding algorithms, since branches are significant curvilinear structures (compared to leaves). Accurate node estimation results from accurate projection of detected branch segments on to the main stem. This property also enables estimation of the position of nodes that are occluded on the main stem.

Both properties of node appearance require accurate identification of the main stem. The main stem generally appeared as the most salient near-vertical line in images, if the main stem was not occluded by other plant foliage. However, other branches were less prominent and less constrained in orientation. Hence, the steps for identifying nodes are broadly described as follows:

1. Estimate main stem and reconstruct possible branches, thence estimating intersection of branches with main stem (single frame analysis – this chapter).
2. Assign node numbers to branch junctions and track nodes to find internode distance (sequential frame analysis – Chapter 5).

Node detection via basic image processing techniques such as thresholding, edge detection and line detection are considered in the following sections. Adequate results for node detection were not achieved using many of these techniques. However, Section 4.9 discusses the eigenvalues of the Hessian matrix method of line detection, which was found to be effective at extracting curvilinear structures from the field images.

Typical results are shown in the following sections for image processing techniques which were considered of sufficient promise to code and evaluate by application to the field images. Other techniques, such as matched filtering, were investigated theoretically only and not coded if the algorithm was considered too expensive in developmental resources or in run-time computational requirement in relation to the expected results.

## 4.5 Preprocessing of field images

Preprocessing steps were necessary to prepare the images for stem detection. This included determining and isolating the 'window area' and removing interlacing effects.

Due to the speed at which the enclosure moved through the canopy (0.10 to 0.30 m/s), interlacing effects were observed in the captured footage. Deinterlacing processes involve discarding either the set of odd or even lines of the image and then (usually)

restoring the image to its original size using interpolation. In the present case, acquired imagery was deinterlaced by simply separating the image into odd or even lines only. The resizing step was omitted since resizing does not improve the resolution of the data, and the distorted aspect ratio of the image does not influence the effectiveness of image processing.

The images used for algorithm development were collected with the camera oriented in portrait to maximise the amount of main stem present in the image. However, the camera's native image orientation was landscape. Therefore, the downloaded images were rotated 90° so that the image was portrait and the plant appeared upright during the image processing steps.

Acquired imagery contained both 'window' and 'non-window' areas. The non-window area of the image contained features that could influence further image processing results, such as the window scale marks, electrical wiring and the textured fibreglass surface of the box interior. The box interior was painted flat black so that there was a significant difference in intensity between the window area and box interior. The image was separated into window and non-window area using the following steps (Figure 4.9):

1. **Contrast enhancement** was performed to produce an image in which the non-window area was close to black and the window area was white. However, some white areas existed in the non-window area due to reflections of objects in the box, and some black areas existed in the window area due to shadows in the foliage. Hence, a threshold was applied to convert the image to binary, with black representing the non-window area and shadowed areas of the captured scene.

2. A **flood fill** with a seed point near the image boundary selected all connected pixels of similar intensity. A single solid region corresponding to the non-window area was selected, which was not connected to any other dark objects in the window scene. This step of the mask processing could only occur when the window area featured no shadow areas close to the border.

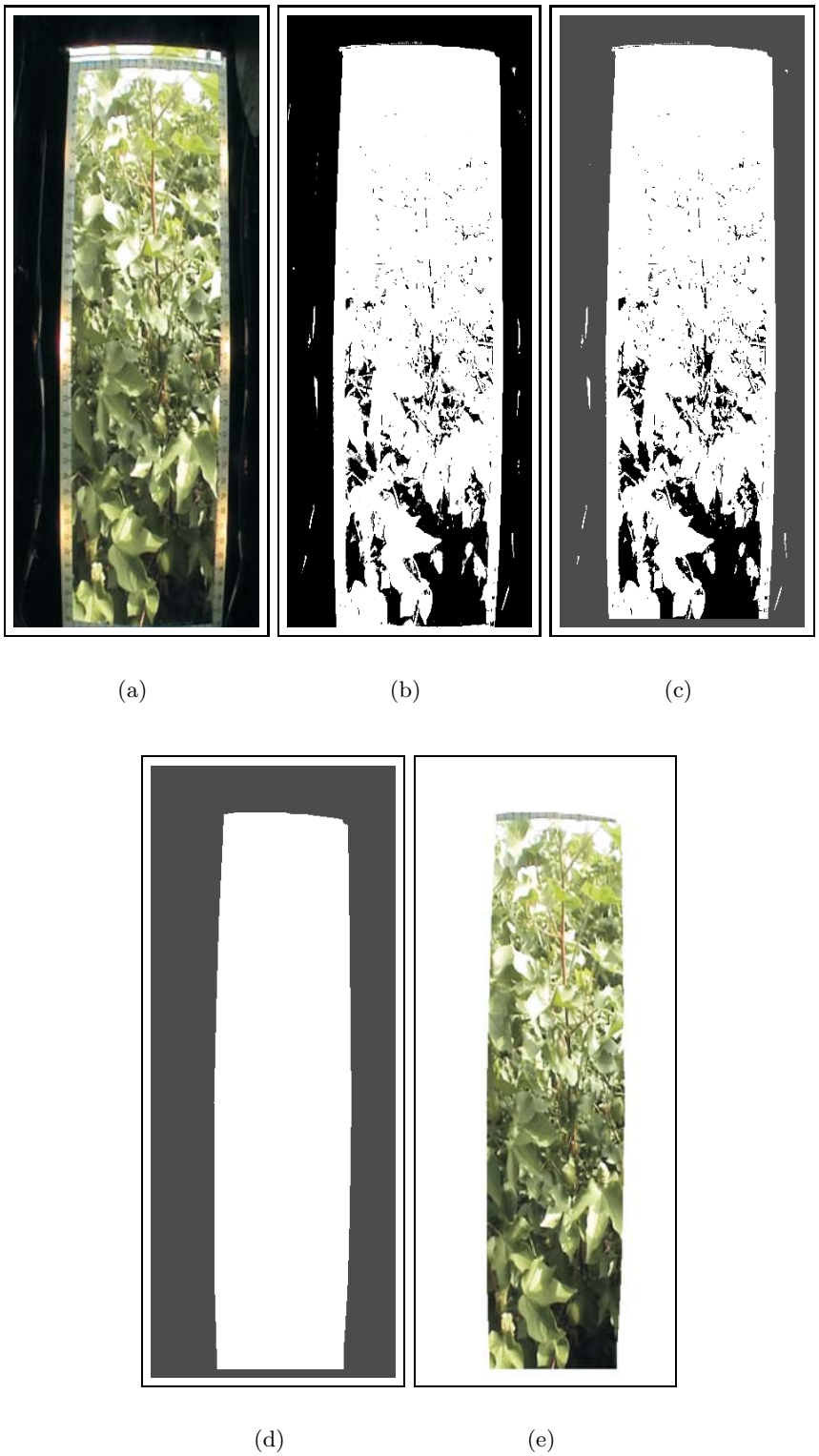


Figure 4.9: Mask generation process: (a) input image from camera enclosure; (b) contrast enhancement; (c) non-window pixels (in grey) separated from window-area pixels (in black) by flood fill operation; (d) morphological operation to remove gaps; and (e) mask applied to input image.

3. **Mathematical opening**[2] was performed for the purpose of removing small white areas in the non-window region of the image. This produced a solid black region in the image that represented the non-window area. A mathematical dilation was then performed so that the mask extended to include the window scale (which was too light to be included in the mask thus far).

The mask generated by this process was applied to all subsequent images. Hence, the mask only needed to be created once per video capture session.

## 4.6 Colour processing and thresholding

The images used for algorithm development were in 24-bit RGB format (Section 4.2). This potentially enabled tonal information to be used to differentiate between leaves and stems, providing such differences exist in the visible wavebands. In situations where intensity or tonal differences exist between objects of interest and other non-useful background information, thresholding may be used to isolate the objects of interest. The desired outcome of successful thresholding for the cotton plant imagery was to isolate stem pixels from leaf and background pixels.

### 4.6.1 Global thresholding

For the purpose of comparison, thresholding results for a cotton plant image from a glasshouse environment are included. In the glasshouse image, there was significant tonal difference between the plant and background that enabled thresholding to segment the plant in the image. Thresholding may be used on a greyscale image, or on a transform of the three colour components of an RGB image such as the 'excess green' criterion $ExG$, which is effective at discriminating green plant matter from background soil (Woebbecke et al., 1995) and is given by $ExG = 2G - R - B$, where $R$, $G$ and $B$

[2] Mathematical opening is one of a series of morphological operators (Serra (1982), Jain et al. (1995)) which searches for and transforms (e.g. dilates, erodes) a predefined shape in a binary image.

are the red, green and blue pixel intensities, respectively. The excess green criterion successfully discriminated between the plant and background in the glasshouse image (Figure 4.10). Furthermore, discrimination is achieved between stems and exposed top-of-leaf areas, which by visual inspection was a different shade of green to the bottom-of-leaf areas present in this image.

The excess green criterion was effective for the non-green background present in the glasshouse. However, this was not the case in the field images, where the target plants have a background of green foliage. Figure 4.11 contains the four sample images of Figure 4.4 thresholded based on the excess green transformation. This figure demonstrates that the criterion was not effective at discriminating between stems and leaves, or stems and background material.

Figure 4.12 contains the sample field images and their corresponding red, green and blue colour channels (each 8-bit), to enable visual assessment of the potential for colour to be used to segment stems in the cotton plant field imagery. By visual inspection, the blue image provided the least contrast between both leaves and stems, and the foreground and background material. The red image provided contrast between foreground and background material and some contrast difference between leaves and stems. However, the green image appears to provide the largest contrast between foreground stems and other material. Therefore, the green channel was used in the remaining image processing evaluations.

Spectral analysis of stem and leaf matter may potentially enable identification of significant wavelengths to discriminate between the two plant materials (Kondo & Ting, 1998). Hyperspectral image analysis featuring a range of significant wavelengths may potentially be used to differentiate leaves and stems based on narrowband reflectance ratios. A possible solution is demonstrated in van Henten et al. (2002), where a multiple-camera, two-wavelength system is employed in a glasshouse to enable discrimination of plant materials by relative rather than absolute reflectances. A preliminary spectral analysis of cotton plant materials was conducted (Appendix C) for the purpose of identifying potential discriminatory wavelengths. However, this approach

(a)

(b)

(c)

(d)

(e)

Figure 4.10: Segmentation of a glasshouse image based on the 'excess green' criterion of Woebbecke et al. (1995): (a) original image; (b) greyscale image of excess green value, scaled between 0 and 255; and (c)–(e) excess green value from image (b) thresholded at: (c) 20; (d) 40; and (e) 60.

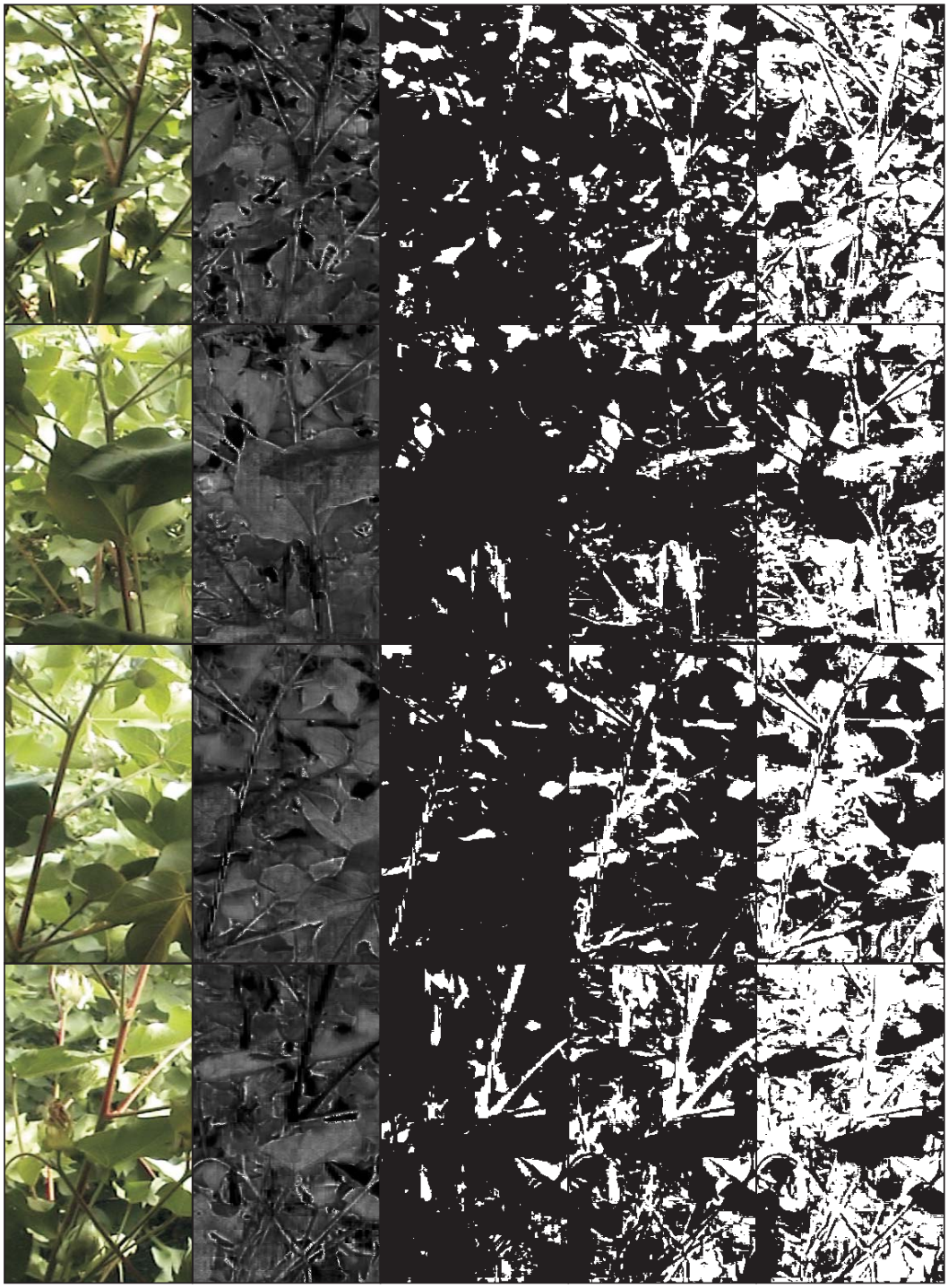

(a) (b) (c) (d) (e)

Figure 4.11: Excess green transformation of Sample Images 1 to 4, in rows 1 to 4 respectively. For each row: (a) input image; (b) greyscale image of excess green value, scaled between 0 and 255; and (c)–(e) excess green value from image (b) thresholded at: (c) 20; (d) 40; and (e) 60.

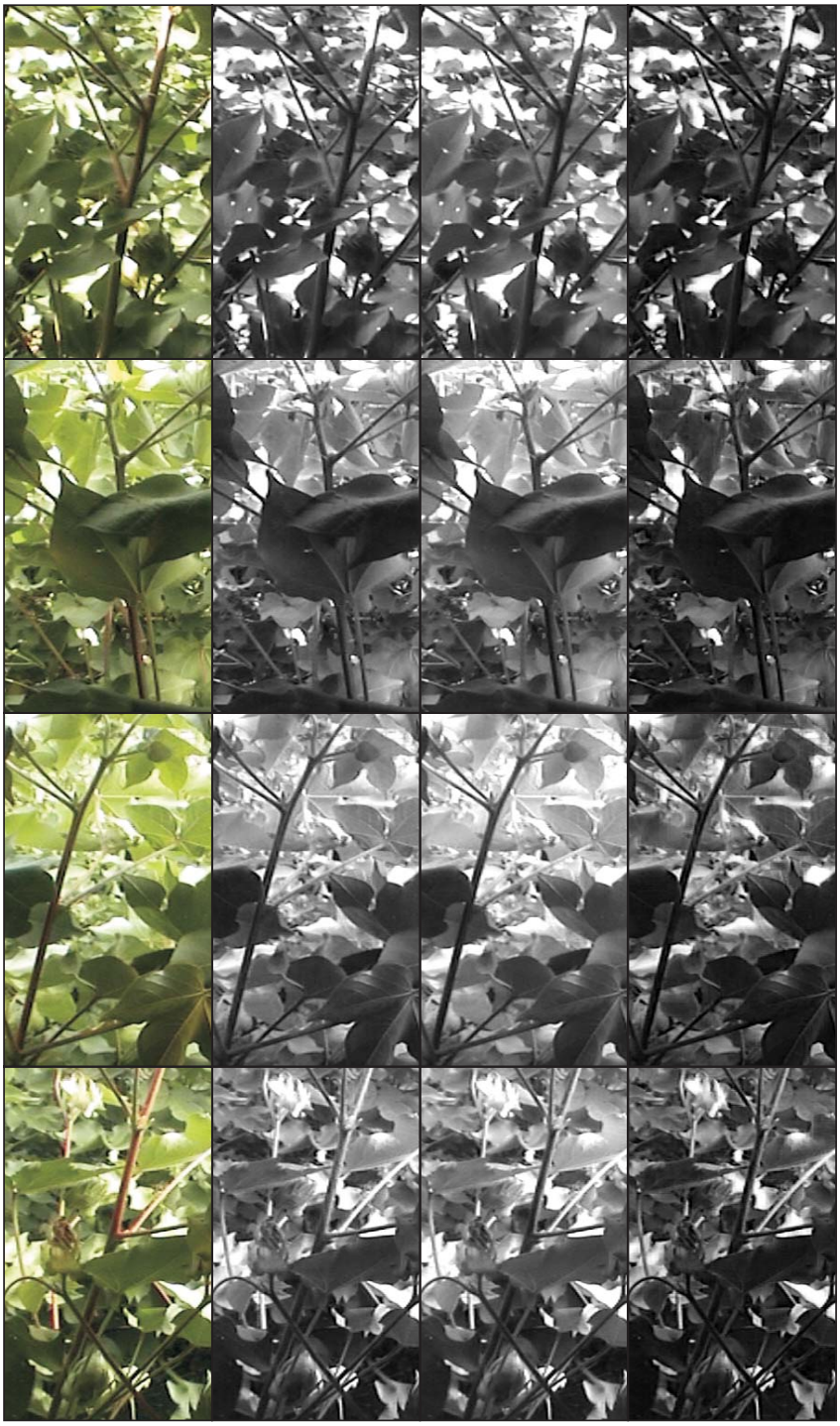

(a) (b) (c) (d)

Figure 4.12: RGB channels of Sample Images 1 to 4, in rows 1 to 4 respectively, where the three separate channels are rendered to grayscale to permit comparison. For each row: (a) input image; (b) red channel; (c) green channel; and (d) blue channel.

was not pursued further due to the overriding factor that in outdoor environments and in the absence of shading, ambient sunlight would prevent uniform illumination of the plant and hence, prevent consistent reflectance measurements within the image area.

### 4.6.2 Adaptive thresholding

A uniform image intensity threshold was identified (Section 4.6.1) as ineffectual for whole-image discrimination of stems and leaves. However, some images exhibited high contrast between the node and the localised background, such as the upper nodes visible in Sample Images 2 and 3 (Figure 4.4). In these images, the high contrast was caused by the target plant in front of the window falling into the camera enclosure's shadow, whilst the foliage behind the plant was illuminated by sunlight. The high contrast potentially enabled localised thresholding about the main stem to segment the node from the background. Successful segmentation of stems from background could enable shape analysis on the foreground to identify whether a branch junction (or node) is present, or whether the stem area is a straight line without joints (and hence no node present). However, this method is only suitable for nodes that are visible in the window area (i.e. the method does not detect nodes that are occluded by foliage).

Four square (side 40 pixels) regions of interest were examined along the main stem of Sample Image 1 (identified in Figure 4.13), for which intensity histograms are shown in Figure 4.13(a). In the thresholded images of Figure 4.13(c), black is foreground and white is background, where foreground was ideally stems and background was other foliage. Although an automatically-selected threshold was not coded for this evaluation, the threshold intensity was manually chosen to coincide with the 'valley' in the histogram shape (e.g. as described in Sezgin & Sankur (2004)). The valley occurs at the union of two normally-distributed intensity populations, which assumes that stems and background form two distinct populations in the sample squares analysed. This seemed a reasonable assumption since stems often appear dark on a background of a distinct (lighter) intensity, such as for the upper nodes of Sample Images 2 and 3.

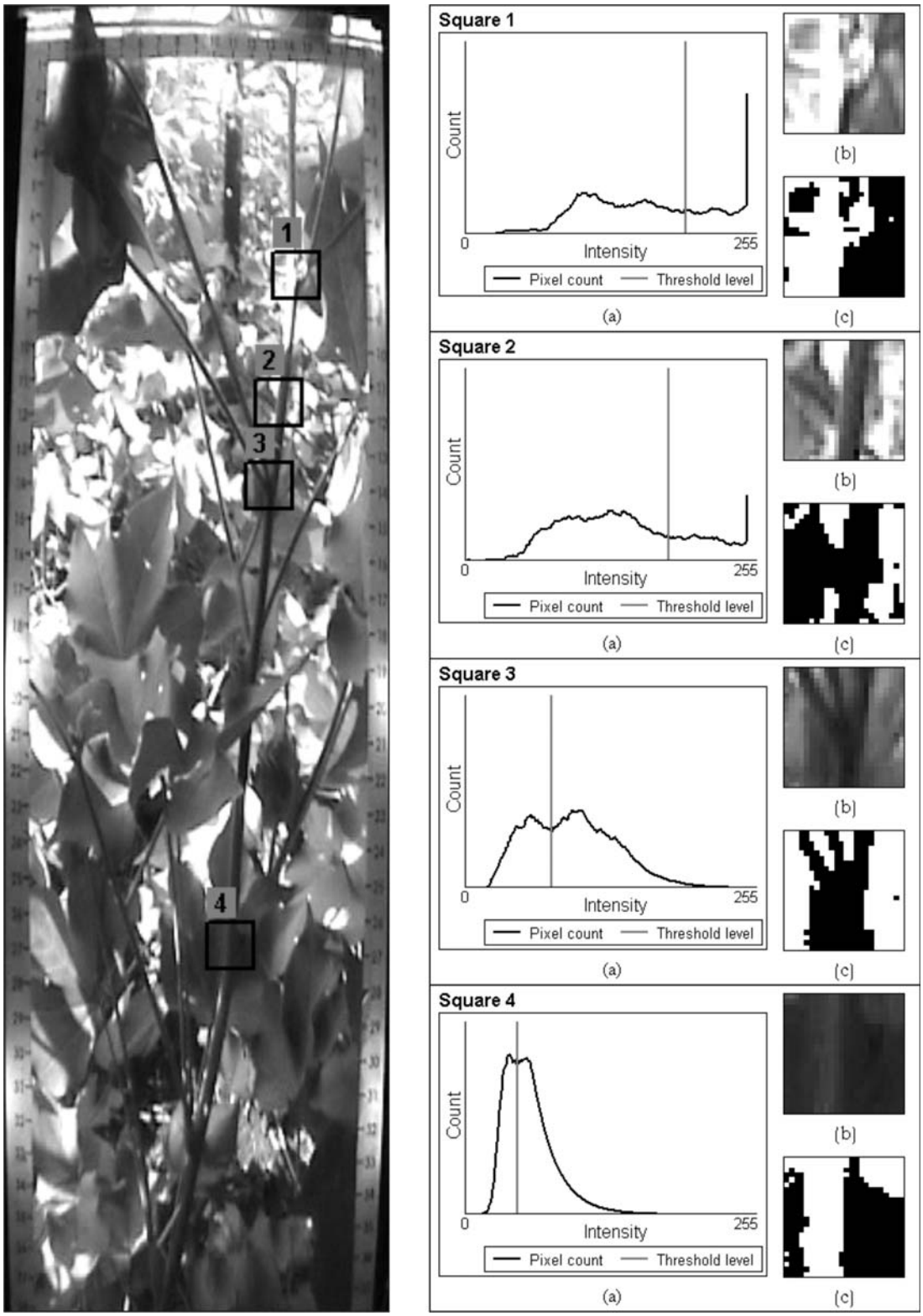


Figure 4.13: Adaptive thresholding of Sample Image 1 (on the left). For each of the Squares 1 to 4 along the main stem, (a)–(c) is a study of adaptive thresholding as follows: (a) histogram of green channel for sample square; (b) detail of sample square; and (c) image (b) thresholded at an intensity value that was manually chosen to coincide with a valley in the histogram.

None of the four sample squares from Sample Image 1 accurately segmented the stems from the background (Figure 4.13). Square 3 showed a true branch junction being segmented in the thresholded image, although some background material was also included in the detected stem area. In Square 1, the stems were too bright to be detected (and no clear valley is evident in this histogram). Square 2 shows stems and background foliage being detected as foreground stems and Square 4 has low contrast and a partial occlusion which prevented stems from being effectively segmented.

The adaptive thresholding process based on histogram shape was evaluated on the other sample images of Figure 4.4, and similar results for inaccurate segmentation of stems were obtained. Some stem areas were identified correctly, such as for the higher nodes of Samples Images 2 and 3, but a consistent problem was the false classification of shadowed areas of background foliage as foreground stems, as was the case for Square 2 of Figure 4.13. Therefore, it was concluded that the adaptive thresholding method was not effective for general node detection due to the overlap in intensities exhibited by nodes and other foliage behind the main stem.

## 4.7 Edge detection

Although plant stems had variable tonal properties in acquired images, their shape was consistently long, smooth and curvilinear, which potentially enabled edge detection to be used to detect stem edges. An edge is a significant local change in image intensity (Jain et al., 1995) and the profile of an edge point approximates a step function for sharp edges, or a ramp function for soft edges (Figure 4.14(a) and (b)). A line is a type of edge where the image intensity changes from a background value, to the edge value, and then returns to the background value within a short distance. Line profiles are represented in Figure 4.14(c) and (d) and are considered further in Section 4.8.

Parallel edge detection operators evaluate the local image gradient of every pixel to determine whether that pixel is an edge point. Common edge detector results (Fig-

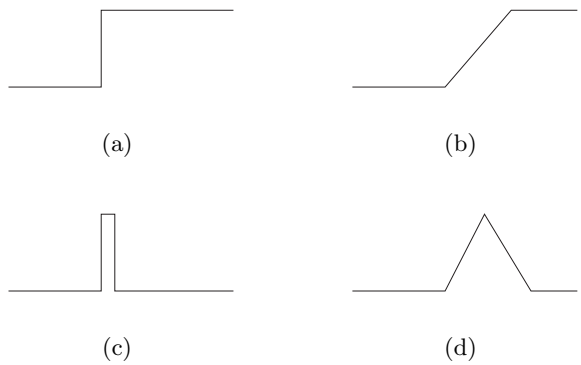


Figure 4.14: Edge profile descriptors in one dimension: (a) step; (b) ramp; (c) top hat (or bar); and (d) roof.

ure 4.15, algorithm details in Appendix D) demonstrated that both branch edges and edges caused by randomly-oriented leaf edges yielded strong responses. This limits the applicability of edge detection for identifying branches. However, a prominent response to the main stem was obtained for the vertical edge detector and adaptive thresholding (Figure 4.15(c) and (d)).

Another type of edge detection is edge following, which is a sequential edge detection process where edges are followed, pixel by pixel, from an initial point until the edge fails some local gradient strength criterion. This method was judged to be inappropriate for the plant images because, as was apparent in the adaptive thresholding discussion of Section 4.6.2, there is overlap and variation in the intensity levels of stem and leaf pixel areas which is likely to prevent edges between stems and background foliage from being accurately followed.

## 4.8 Line detection

In the preceding sections, automatic thresholding and edge detection were discounted as methods of identifying branches in images. This led to the consideration of line detection strategies. A line is a type of edge in which the change in image intensity associated with the edge returns to its original level, as is the case for the stems in

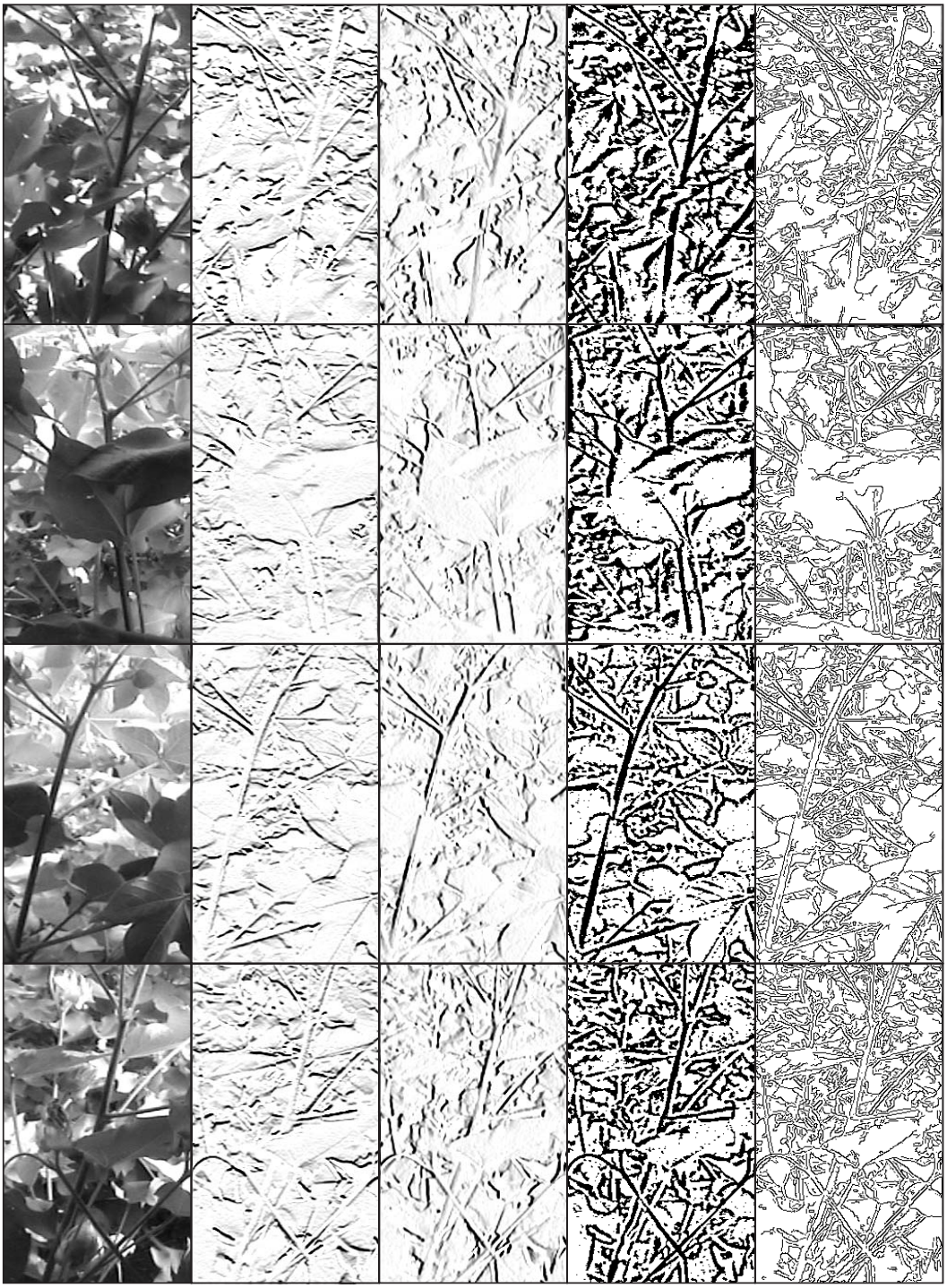

(a) (b) (c) (d) (e)

Figure 4.15: Common edge detectors applied to Sample Images 1 to 4, in rows 1 to 4 respectively. For each row: (a) input green channel image; (b) Sobel horizontal edges; (c) Sobel vertical edges; (d) edges by adaptive thresholding; and (e) Canny edge detection with $w = 8$, $t_{low} = 30$ and $t_{high} = 150$ (Appendix D.1.3).

the cotton plant images. Other comparable computer vision applications which require detection of lines in images are as follows (Figure 4.16):

- Roots in soil (rhizotron) images (Bakic, 1996). Occlusions may be caused by soil particles and a large range of root widths may be required to be detected.
- Blood vessels in medical images (Chanwimaluang & Fan, 2003).
- Roads in aerial mapping images (Steger, 1996). These images may feature occlusions caused by shadows and vehicles on the road.

In these applications, lines of interest in a single image may have varying width, intensity, contrast and length, and may also be subject to occlusion by other image features. Hence, these applications were deemed to be visually similar to the detection of stems in plant images.

A technique commonly-used to extract blood vessels from biomedical images is matched filtering (e.g. Chanwimaluang & Fan (2003)). The technique also finds application in the automated extraction of roots from soil images (Zeng et al., 2006). This process involves applying a series of Gaussian masks to the image, one mask for each expected orientation and width of line to be detected. A complete network of lines may potentially be detected. However, the processing may take several minutes per image as was not considered appropriate for this application. Another technique commonly encountered in biomedical image analysis is the eigenvalues of the Hessian matrix method.

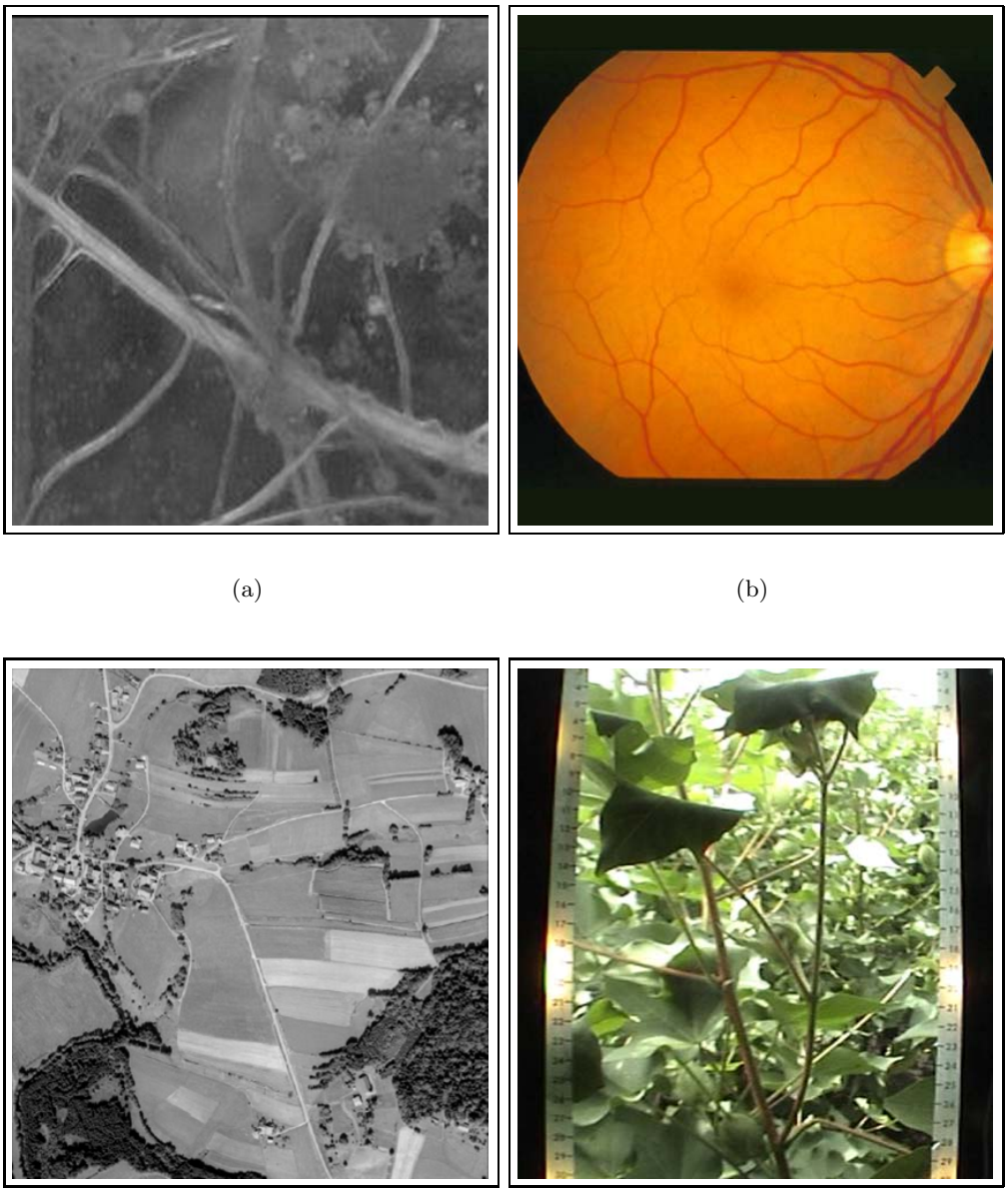


Figure 4.16: Vision applications where line detection is required (reproduced from published literature as follows): (a) roots in soil images (Bakic, 1996); (b) vessels in medical images (Chanwimaluang & Fan, 2003); (c) roads in aerial images (Steger, 1996); and (d) the present application of stems in cotton plant images (McCarthy et al., 2007).

## 4.9 Line detection using eigenvalues of the Hessian matrix

A method of extracting curvilinear structures from an image involves calculating the eigenvalues of the Hessian matrix $\mathcal{H}$, which is the square matrix of second-order partial derivatives for a given function (Magnus & Neudecker, 1999):

$$\mathcal{H} = \begin{bmatrix} I_{xx} & I_{xy} \\ I_{xy} & I_{yy} \end{bmatrix} \tag{4.3}$$

where $I_{ab} = \frac{\partial^2 I}{\partial a \partial b}$ for each image pixel. For the current application, the function $I$ is the pixel's intensity or greyscale value.

The eigenvalues of $\mathcal{H}$, denoted by $\lambda_1$ and $\lambda_2$, can be used to extract the principal direction in which the local second order structure of the image features can be decomposed and detect tubular (3D) or curvilinear (2D) structures in an image (Frangi et al., 1998). The image second-order derivatives are computed by convolving the image with derivatives of a Gaussian kernel with standard deviation $\sigma$ (as per Steger (1996)). Multiple convolutions of an image with masks at different orientations are not required (in contrast to matched filtering in Section 4.8) and lines of different widths may be targeted by varying the standard deviation $\sigma$ of the smoothing filter, with larger $\sigma$ values causing wider lines to be detected. Successful applications of the eigenvalues of the Hessian matrix include enhancement of blood vessels in medical images (Sato et al., 1997; Frangi et al., 1998; Hladuvka & Groller, 2002) and automated extraction of roads from aerial mapping images (Steger, 1996).

Iteration through values of $\sigma$ on the sample images and visual inspection of results revealed that $\sigma = 1.2$ yielded a strong response to branches. Figure 4.17(b) demonstrates the maximum Hessian matrix eigenvalue for Sample Images 1 to 4. However, both stem and leaf edges have been detected in these images. Thresholding the magnitude of the eigenvalues reduced noise and removed weak responses, limiting the response of leaf frontage areas (for example, compare the response of leaf areas in Figure 4.17(b) to

other areas of the image). However, as the threshold is increased (Figure 4.17(c)–(e)), valid stem pixels as well as leaf edges were eliminated.

## 4.10 The 'vesselness' measure

Whilst line saliency (i.e. conspicuousness) is related to the magnitude of the Hessian matrix eigenvalues (as used in Steger (1996)), criteria based on some other function of the Hessian matrix eigenvalues can be used to classify image pixels as either 'tube-like' or 'blob-like' (Table 4.1) (Sato et al., 1997; Frangi et al., 1998). Figure 4.18 demonstrates the input images transformed using the 'vesselness' measure $\mathcal{V}_o$ of Hessian matrix eigenvalues, as described in Frangi et al. (1998). The vesselness is a measure of the likelihood of the pixel belonging to a blood vessel in Frangi et al. (1998), or (here) a plant stem.

Table 4.1: Possible patterns of Hessian matrix eigenvalues $\lambda_1$ and $\lambda_2$ in 2D, with N=noisy; L=low; H=high; +/− indicating eigenvalue sign; and $|\lambda_1| \leq |\lambda_2|$. (Source: Frangi et al. (1998))

| $\lambda_1$ | $\lambda_2$ | Image structure |
|---|---|---|
| N | N | noisy, no preferred direction |
| L | H− | tubular structure (bright) |
| L | H+ | tubular structure (dark) |
| H− | H− | blob-like structure (bright) |
| H+ | H+ | blob-like structure (dark) |

According to Frangi et al. (1998), the vesselness measure consists of two criteria, the 'blobness' measure $\mathcal{R}_\mathcal{B}$, and the 'second order structureness' $\mathcal{S}$. The blobness $\mathcal{R}_\mathcal{B}$ is given by the ratio of the Hessian matrix eigenvalues $\lambda_1/\lambda_2$ and has a relatively low value for tubular (rather than blob-like) structures. The second order structureness, which gives a low response where there is low image contrast or no image structure, is calculated using the Frobenius matrix norm $||\mathcal{H}||_F$ of the Hessian matrix $\mathcal{H}$,

$$\mathcal{S} = ||\mathcal{H}||_F = \sqrt{\sum_{j \leq D} {\lambda_j}^2} \tag{4.4}$$

where $D$ is the dimension of the image (here $D = 2$).

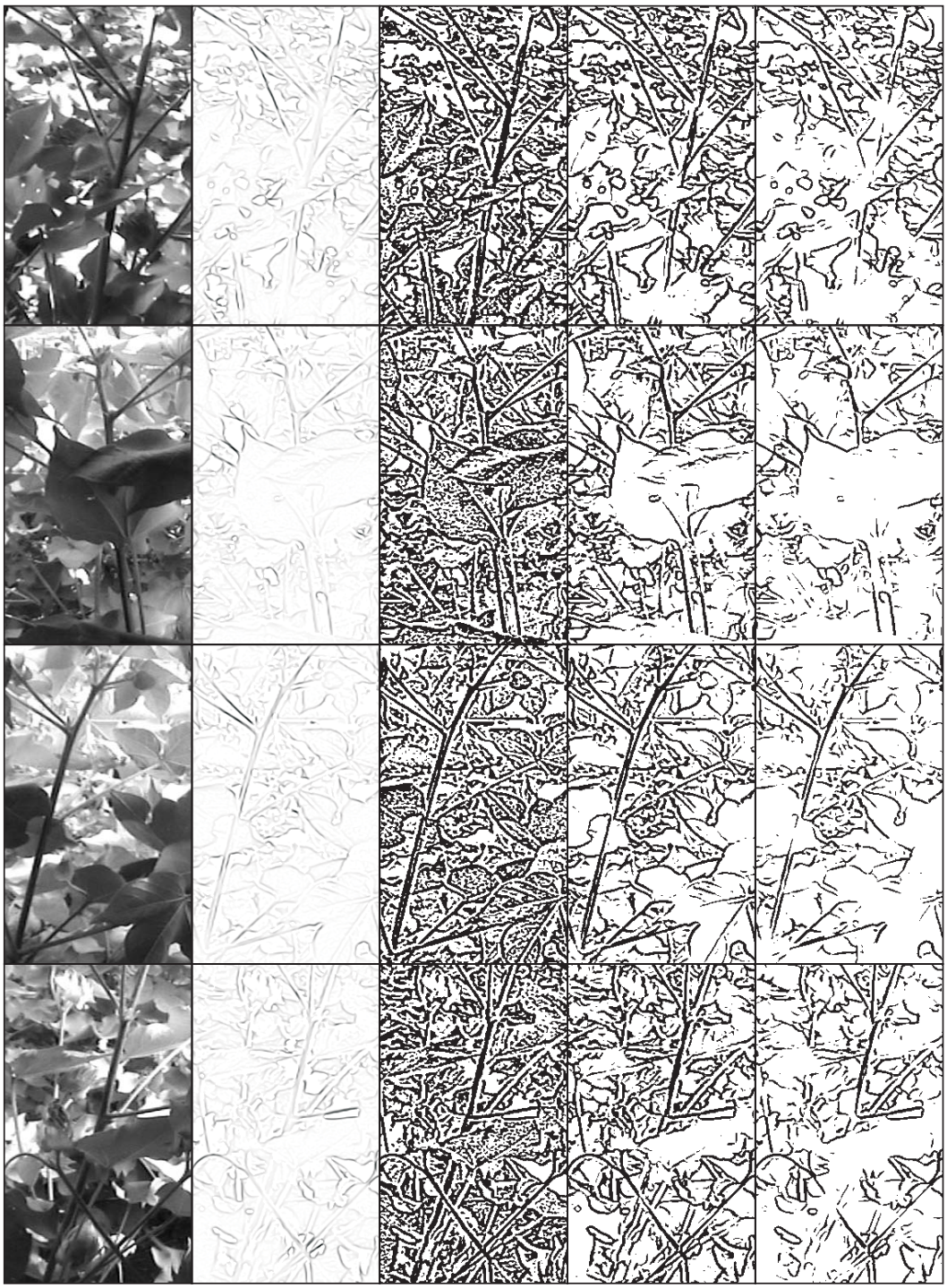

(a) (b) (c) (d) (e)

Figure 4.17: Hessian matrix eigenvalues of Sample Images 1 to 4, in rows 1 to 4 respectively. For each row: (a) input green channel image; (b) magnitude of the maximum Hessian matrix eigenvalue for $\sigma = 1.2$, scaled to intensities between 0 and 255; and (c)–(e) Hessian matrix eigenvalues from image (b) thresholded at: (c) 0; (d) 20; and (e) 50. Note image (b) is hard to see on paper but renders well in the electronic version of the image.

The $\mathcal{R}_{\mathcal{B}}$ and $\mathcal{S}$ measures are combined into the following vesselness expression, in which $\beta$ and $c$ are thresholds which control the filter's sensitivity to $\mathcal{R}_{\mathcal{B}}$ and $\mathcal{S}$, respectively:

$$\mathcal{V}_o = \begin{cases} \exp\left(-\frac{\mathcal{R}_{\mathcal{B}}{}^2}{2\beta^2}\right)\left(1 - \exp\left(-\frac{\mathcal{S}^2}{2c^2}\right)\right) & \text{if } \lambda_2 > 0; \\ 0 & \text{otherwise.} \end{cases} \tag{4.5}$$

The vesselness images of Figure 4.18 show that stem pixels were prominent compared to other foliage pixels, with decreasing $\mathcal{R}_{\mathcal{B}}$ value. In Figure 4.18(b), the image consisted of mainly disjointed pixels that were more concentrated around stem areas and some leaf edges. In Figure 4.18(c) more background pixels were accentuated but the pixels that were part of leaf and stem edges formed connected regions, whilst in Figure 4.18(d) many stem, leaf and background foliage edges were apparent and joined in a single connected region. Of the three images, Figure 4.18(c) was of most use since stems formed continuous regions. The vesselness value was then thresholded (Figure 4.19) to remove pixels of low vesselness which otherwise randomly connected stem regions with other edges. The threshold was selected so that stems formed continuous regions that were disconnected from other image features (Figure 4.19(c)) which potentially enables the use of a size filter on connected components to isolate stem regions.

A single stem appeared as two parallel lines (e.g. Figure 4.19(b)) when the shadowing befalling a wide stem caused the stem to resemble a pair of dark lines (when compared to the intensity of the background foliage). From visual inspection of image processing results, this did not cause a problem for the vesselness function since the pixels that were identified as branch centrepoints were not based exclusively on the vesselness measure but also involved a secondary calculation which was the line centrepoint algorithm of Steger (1996) (Section 4.11.1).

### 4.10.1 Extracting branches from vesselness image

The thresholded vesselness image has been identified (Figure 4.19(c)) as useful for accentuating branch areas, where branches coincided with large connected regions of 'on' pixels. However, background noise and the smaller-area edges form smaller connected

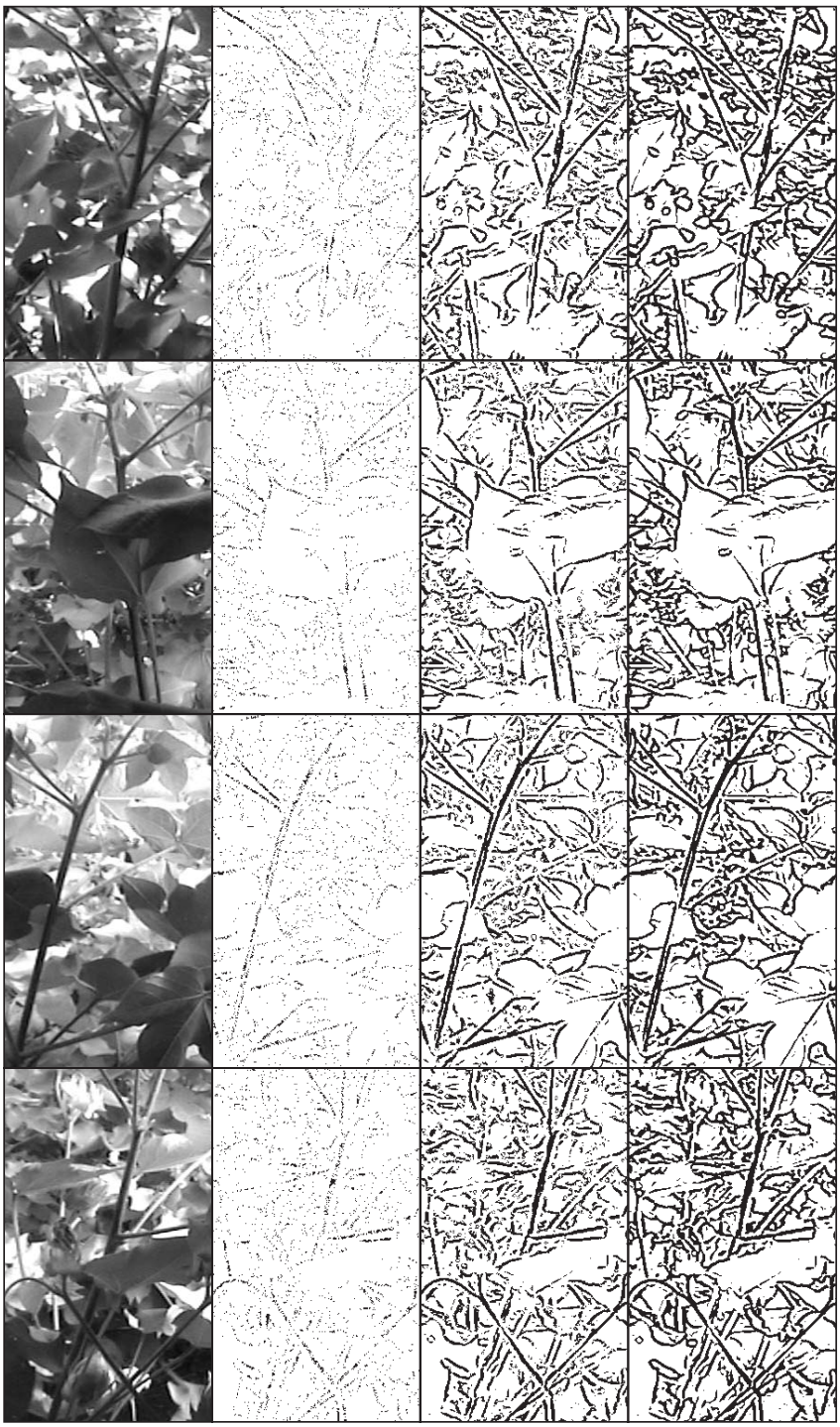

(a) (b) (c) (d)

Figure 4.18: Vesselness measure of Sample Images 1 to 4, in rows 1 to 4 respectively. For each row: (a) input green channel image; and (b)–(d) vesselness measure for $\sigma = 1.2$ and maximum Hessian matrix eigenvalue exceeding 20, with the vesselness coefficients $\mathcal{S} = 3000$ and $\mathcal{R}_{\mathcal{B}}$ at a value of: (b) 0.001; (c) 0.01; and (d) 0.1.

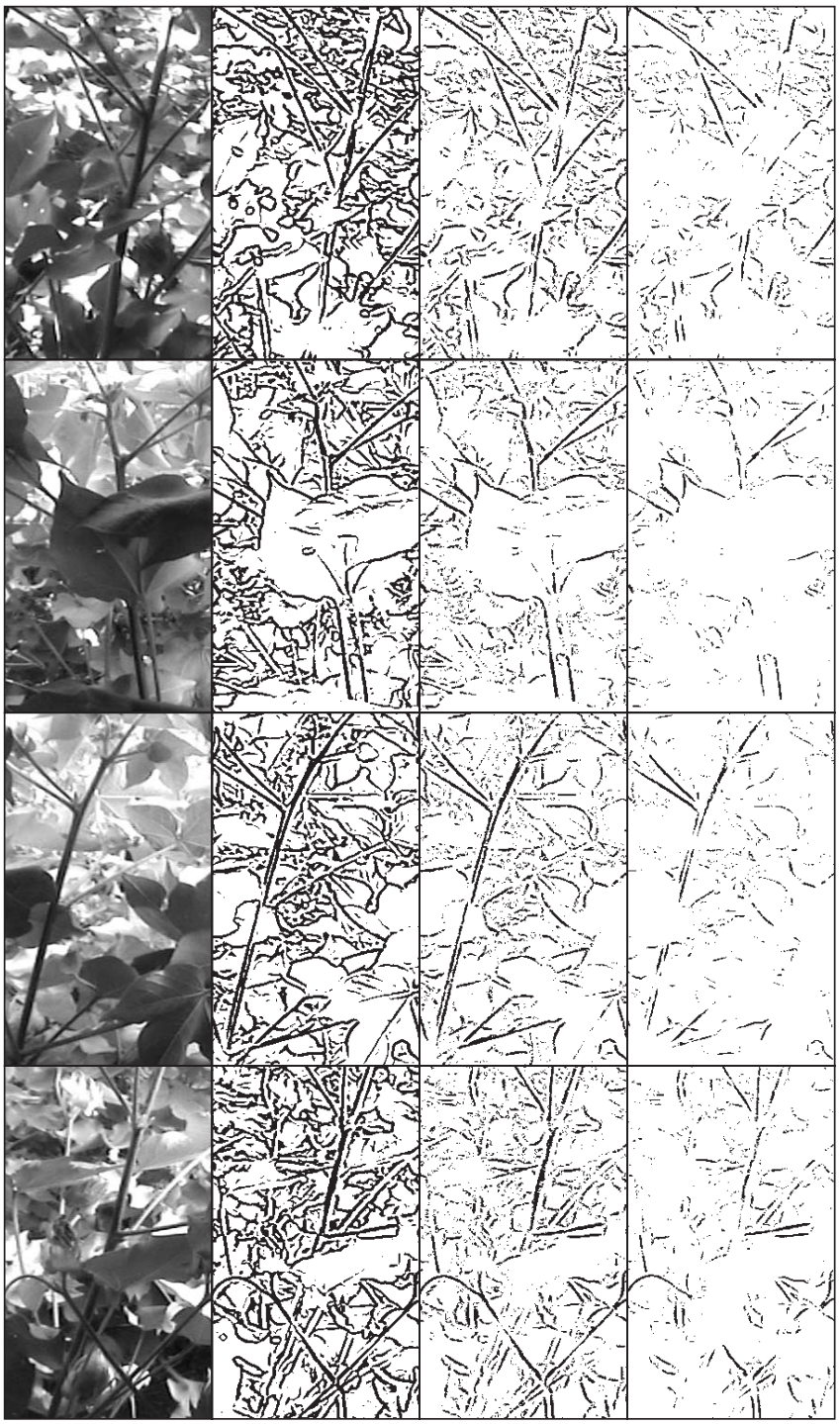

(a) (b) (c) (d)

Figure 4.19: Thresholded vesselness measure of Sample Images 1 to 4, in rows 1 to 4 respectively. For each row: (a) input green channel image; (b) vesselness measure from Figure 4.18(b); and (c) and (d) vesselness from (b) thresholded at: (c) 0.01; and (d) 0.1.

regions in these images. Therefore, a size filter was used to isolate the larger areas. The effect of increasing the size filter from 10 to 100 pixels is demonstrated in parts (c)–(e) of Figures 4.20 and 4.21. In this evaluation, using a size filter of 50 pixels eliminated much of the unwanted lines while not eliminating many true branches.

### 4.10.2 Vesselness response for non-branch features

The discussion so far has focused on detection of stems, which are 'tube-like' structures according to the terminology of Table 4.1. On the other hand, leaf areas are 'blob-like' structures which yield low Hessian eigenvalues compared to stem pixels. The vesselness measure yielded strong responses to both stem and leaf edges, but leaf edges were generally smaller than stem areas hence were eliminated using a size filter.

## 4.11 Fitting lines to branch segments

Branch orientation was required to be estimated from the extracted branch segments so that node position could be calculated from an accurate intersection between the branch and the main stem. This introduced the requirement for lines to be fitted to the branch segments. Fitting a line model to a curvilinear image feature allows a representation of the image feature that is concise, accurate and effective for subsequent processing (Jain et al., 1995). The potential for fitting straight lines and quadratics to extracted branches is considered in Section 4.11.3.

The vesselness response to branches was several pixels wide (reflecting the original feature's saliency; Figures 4.20(d) and 4.20(d)) but with coarse edges that did not match the branch shape in the original image. This diminished the accuracy of any lines fitted to the vesselness branch segments. Therefore, although the vesselness image was effective at detecting branch segments, the vesselness image was expected to introduce inaccuracies in the estimation of branch centreline and orientation and an alternative method for extracting centrelines was required.

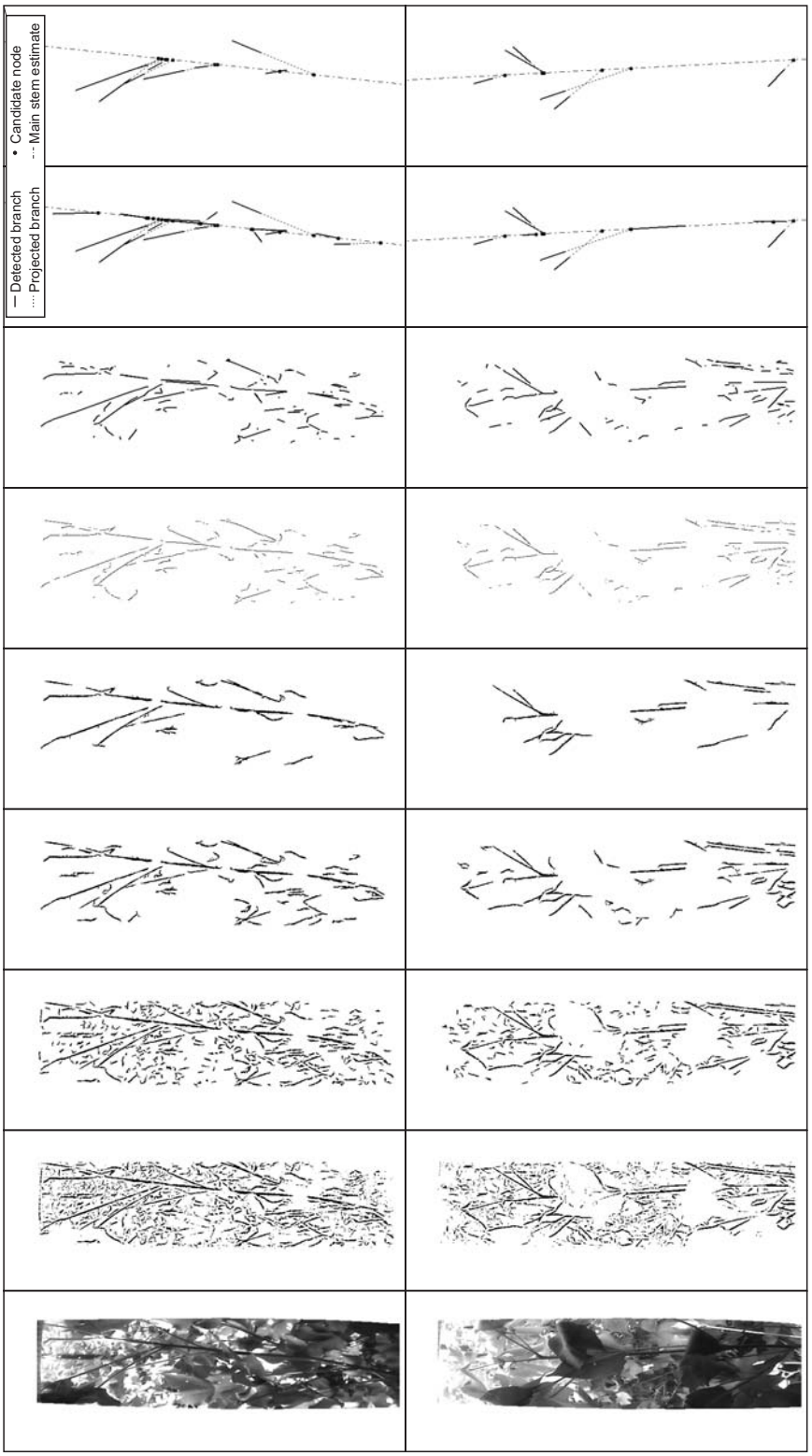


Figure 4.20: Line-fitting steps on Sample Images 1 (row 1) and 2 (row 2). For each row: (a) input green channel image; (b) vesselness function of Figure 4.19(b); (c)–(e) image (b) with a size filter of: (c) 10; (d) 50; and (e) 100; (f) line centre points for image (a) masked with image (d); (g) hop-along lines fitted to image (f); and (h) and (i) lines projected to the main stem that meet criteria for: (h) length; and (i) length and orientation. The sample images are in their uncropped and deinterlaced format. Line-fitting for Sample Images 3 and 4 is shown in Figure 4.21.

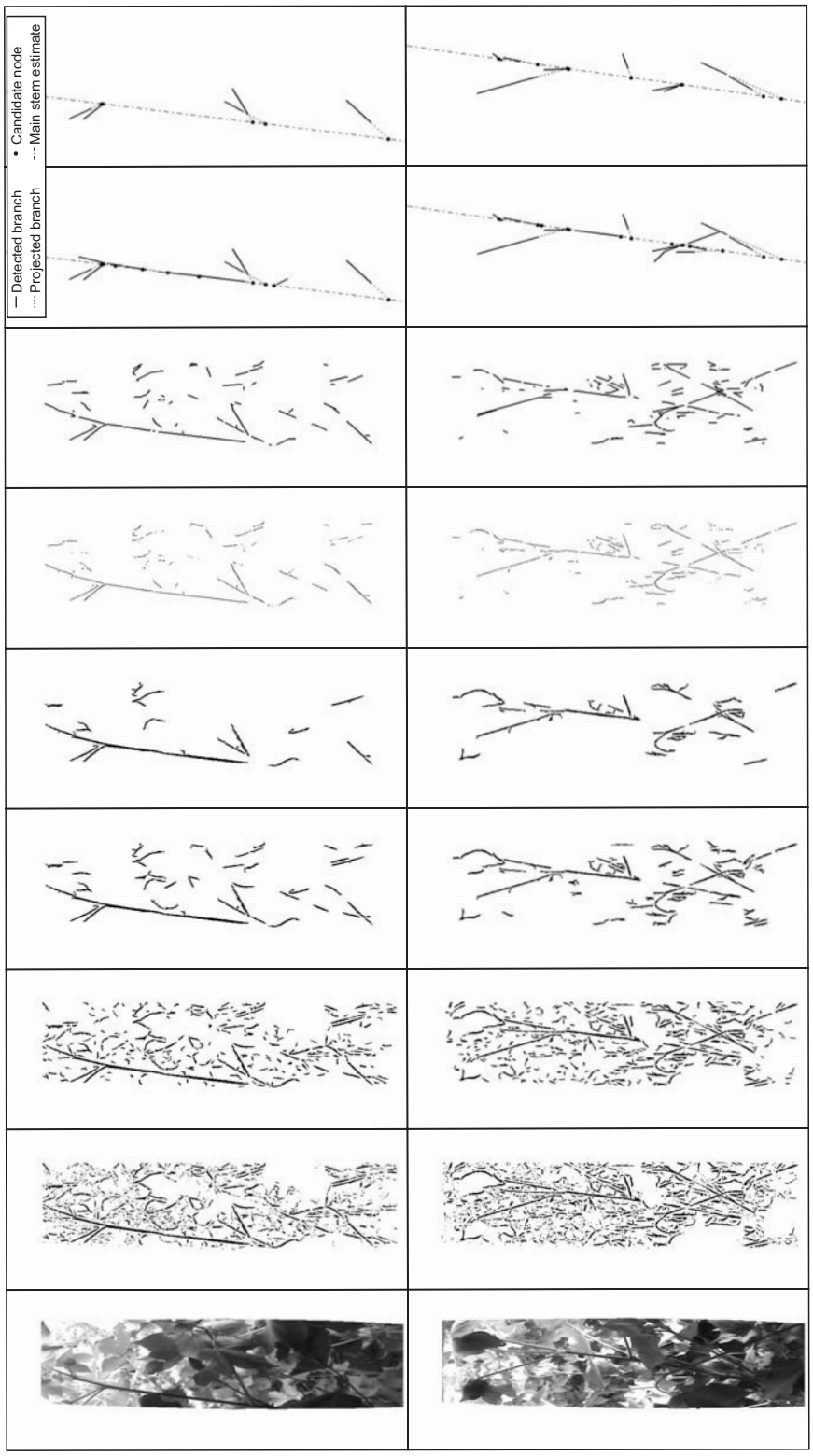


Figure 4.21: Line-fitting steps on Sample Images 3 (row 1) and 4 (row 2). For each row: (a) input green channel image; (b) vesselness function of Figure 4.19(b); (c)–(e) image (b) with a size filter of: (c) 10; (d) 50; and (e) 100; (f) line centre points for image (a) masked with image (d); (g) hop-along lines fitted to image (f); and (h) and (i) lines projected to the main stem that meet criteria for: (h) length; and (i) length and orientation. The sample images are in their uncropped and deinterlaced format.

### 4.11.1 Determining line centre points

Accurate estimation of branch centreline was achieved using the method of Steger (1996), in which the pixel's Hessian matrix eigenvalues and second directional derivatives determine whether the pixel lies at the centre of an arbitrarily-oriented line profile, for a specified $\sigma$ value. The method is as follows. Line centre points exhibit a characteristic 1D line profile in the direction $\hat{\underset{\sim}{n}}$ perpendicular to the line (Figure 4.22). At the centre of the line profile, the first directional derivative in the direction $\hat{\underset{\sim}{n}}$ should become zero and the second directional derivative should be of large absolute value. A zero crossing detector for the image derivatives may be used to find this point to single pixel accuracy, but for sub-pixel accuracy, a second degree Taylor polynomial can be used to find the centre point.

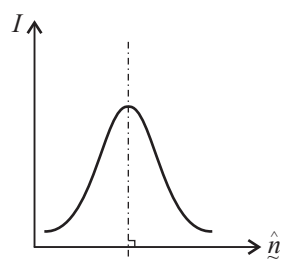


Figure 4.22: Gaussian line profile.

In the 1D case, the second degree Taylor polynomial $p$ is:

$$p\left(x\right) = I + I'x + \tfrac{1}{2}I''x^2 \tag{4.6}$$

where $I$ is the pixel's intensity, and $I'$ and $I''$ are the locally estimated first and second image derivatives on $\hat{\underset{\sim}{n}}$, respectively. For this Taylor polynomial, the required first derivative $p'\left(x\right) = 0$ occurs when $x = -I'/I''$.

In two dimensions, the direction perpendicular to the line is given by $\hat{\underset{\sim}{n}} = (n_x, n_y)$, the unit eigenvector corresponding to the eigenvalue of maximum absolute value. The zero crossing position $(c_x, c_y)$, to sub-pixel accuracy, is given by:

$$(c_x, c_y) = (tn_x, tn_y) \tag{4.7}$$

where $t$ is the solution to the first derivative of the second-order, two-dimensional Taylor polynomial:

$$t = -\frac{I_x n_x + I_y n_y}{I_{xx} n_x^2 + 2 I_{xy} n_x n_y + I_{yy} n_y^2} \ . \tag{4.8}$$

A pixel is a line centre point if the zero crossing occurs within the current pixel, i.e.

$$(c_x, c_y) \in \left[-\frac{1}{2}, \frac{1}{2}\right] \times \left[-\frac{1}{2}, \frac{1}{2}\right], \tag{4.9}$$

Figure 4.23 shows that according to the differential geometry of a standard line profile, potential line centre points occurred throughout the captured image area. Since only centre points belonging to significant curvilinear structures were desired, line centre points were only required to be calculated for pixels which were deemed to be part of a salient line, e.g. for pixels which had a maximum Hessian matrix eigenvalue exceeding some threshold (as in Steger (1996)), or for pixels which belonged to large areas that exhibited vesselness, i.e. the branch pixels of Figure 4.20(d) and 4.21(d). Therefore, the centre points corresponding to branches were isolated by performing a logical AND operation on the centre points and vesselness images (Figures 4.20(d) and 4.21(d)). This yielded an image in which 'on' pixels corresponded to the centre points of detected branch segments (Figures 4.20(f) and 4.21(f)).

### 4.11.2 Main stem identification via the Hough transform

Once the stem and branch centre points were extracted from the input image, the main stem was required to be identified. The Hough transform (Duda & Hart, 1972) was applied to the branch centrepoints of the previous section to estimate the main stem. The Hough transform uses a voting technique to identify strong linear features in an image and is effective even in the presence of large amounts of noise (Jain et al., 1995).

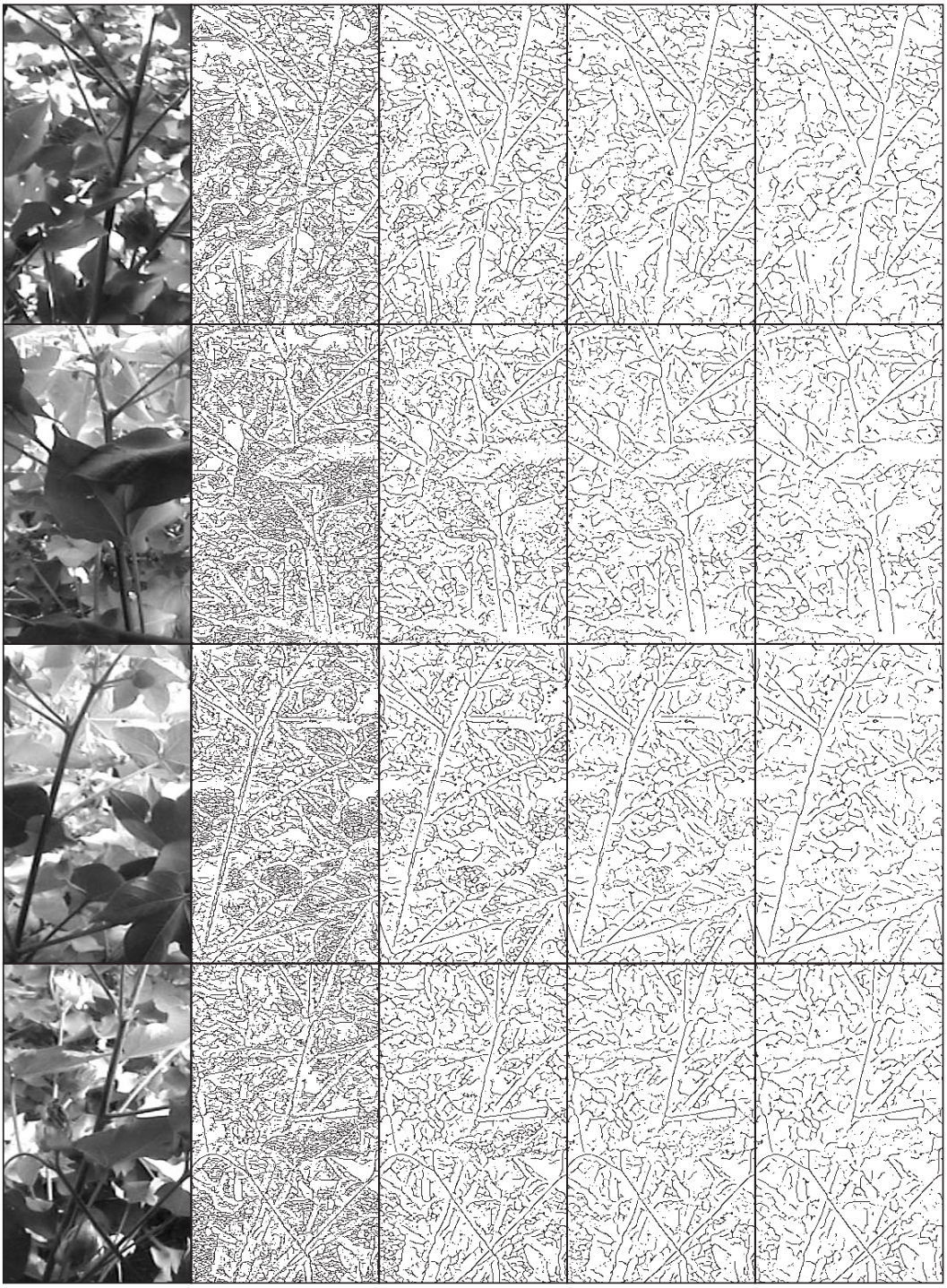

(a) (b) (c) (d) (e)

Figure 4.23: Line centre points of Sample Images 1 to 4, in rows 1 to 4 respectively. For each row: (a) input green channel image; and (b)–(e) pixels corresponding to line centre points, for $\sigma$ values as follows: (b) 0.5; (c) 1.0; (d) 1.2; and (e) 1.5.

Each 'on' pixel, at position $(x, y)$ in the image, contributes a vote to an element $(r_n, \theta_n)$ of an accumulator array of size $r$ by $\theta$ entries, with $r_n$ and $\theta_n$ given by:

$$r_n = \sqrt{x^2 + y^2} \tag{4.10}$$

$$\theta_n = \tan^{-1}\left(\frac{y}{x}\right) \tag{4.11}$$

where $r$ spans 0 to the image diagonal length. In this application, where a near-vertical main stem was desired, the range of $\theta$ was chosen such that the Hough line search space was within $\pm 30°$ of the vertical.

Variables $r$ and $\theta$ form a parameterised representation of the line, with $r$ representing the perpendicular distance to the line (from the origin) and $\theta$ representing the angle to the normal of the line. Representation of the line in the $(r, \theta)$ domain enables a finite state space for the line's parameters. In the slope-intercept domain the range of values for the slope of the line is infinite. This approach assumed that the main stem was close to vertical, was partly visible and was the single most significant linear structure in the edge map.

To reduce the likelihood of the main stem estimate 'jumping' to another significant line during the sequence (e.g. another branch or another plant's main stem), for each frame $f_k$ the size of the Hough parameter space was limited to $\theta_{k-1} \pm 5°$ and $r_{k1} \pm 15$ pixels, where $\theta_{k-1}$ and $r_{k-1}$ represent the Hough parameters for the previous frame $f_{k-1}$. These criteria were based on visual evaluation and were found to be effective in the sample image sequences. Typical results for main stem detection are shown in Figures 4.20(h) and 4.21(h).

### 4.11.3 Line-fitting algorithms for branch centre points

Branch segments of Figures 4.20(f) and 4.21(f) were generally approximately straight lines with some curvature exhibited in the vicinity of the main stem. Therefore, the branch segments were fitted with straight lines rather than quadratics or some other curve model because an accurate fit was required near the node and the accuracy of

the fit elsewhere on the branch was unimportant.

The Hough transform was considered but not adopted for identifying branch lines since candidate branches were identifiable in the Hough space only when the branch was long and straight. However, branches that were curved yielded a similar response in the linear Hough space to other curved foliage edges (such leaf edges). Therefore, the linear Hough transform was not suitable for discerning the range of branch geometries expected to be encountered in cotton plant images. Instead a line-fitting algorithm called the 'hop-along' method (Jain et al., 1995) was implemented. The hop-along algorithm steps along an ordered edge list (i.e. an edge list in which the coordinates follow the curve end-to-end), and either appends edges to the existing calculated line if the edge points follow the same direction, or starts a new line if there is a significant change in the direction of the edge points. Hence, a curve is represented as a sequence of straight lines joined end-to-end. Results of applying the hop-along algorithm to the branch centre points of Figures 4.20(f) and 4.21(f) are shown in Figures 4.20(g) and 4.21(g), respectively.

### 4.11.4 Choosing lines to project to the main stem

Not all lines detected corresponded to branches (Figures 4.20(g) and 4.21(g)). The detected lines were required to be filtered so that lines that obviously did not correspond to branches were not projected to the main stem to form candidate nodes.

The simplest valid criterion to apply was based on line length, since true branch lines are expected to be longer than erroneous or noisy lines. In addition, true branches were expected to be detected in the vicinity of the main stem, so a criterion was added to prevent short, distant lines from forming candidate nodes, by discarding those lines that were projected over three times their own length to the main stem. The results of application of these criteria are shown in Figures 4.20(h) and 4.21(h), in which black circles denote candidate node positions obtained by projecting filtered lines to the main stem estimate (dash-dot line). Even in this image, false positive candidate nodes were

detected, and further rules were defined to remove lines which were responses to the main stem and lines with a slope that fell with respect to the main stem.

Conditions for determining whether a line was used to form a candidate node are listed below (and pseudocode in Appendix D.2.1). A line is projected to the estimated main stem to form a candidate node if the line meets all of the following seven conditions:

(i) is longer than a threshold length;

(ii) does not cross over the main stem (since in this case the line does not originate at the main stem);

(iii) has an incline which is greater than a threshold angle ($\pm 15°$) to the main stem incline (For two reasons: firstly, if the branch and main stem line estimates are close to parallel, their geometric intersection is likely to overshoot the true node position; and secondly, this rule aims to remove branch lines that correspond to the main stem, so that such branch lines are not projected to the main stem estimate to form candidate nodes);

(iv) has an angle of $< 90°$ to the main stem upward direction (so that the branch rises with respect to the main stem);

(v) is not connected to another similar-sloped line that is closer to the main stem (since the lines are likely to belong to a single branch, and only one line is required to be projected to the main stem);

(vi) has a length that is no shorter than $\frac{1}{3}$ of the total length of the line projected to the main stem (to reduce the occurrence of small erroneous lines at a relatively large distance from the main stem being projected to the main stem); and

(vii) intersects with the estimated main stem within the image bounds.

These rules were applied to filter the lines used to generate candidate nodes. Figures 4.20(i) and 4.21(i) display the line segments that remained after application of these rules to the sample images. Application of these rules found that the rules erred

on the side of false positive prevention and as a result some true positives may be erroneously discarded (on average 6% of true positives were eliminated per frame while 90% of false positives were eliminated by these rules), particularly for rules (i) and (iii).

## 4.12 Summary of single frame algorithm

### 4.12.1 Algorithm for control data set

The following original algorithm was developed based on the work reported in the previous sections to extract node positions from individual frames. The algorithm was used to identify nodes in Images Sequences 1 to 4. Internode length measurement from candidate node positions in successive frames is discussed in the next chapter.

**Algorithm for node identification (per frame)**

1. The image is preprocessed.
2. The image derivatives are calculated by convolving the image's green channel with derivative of Gaussian kernels ($\sigma$).
3. The Hessian matrix eigenvalues and vesselness function are calculated for each image pixel (thresholds for $\lambda_1$ and $\lambda_2$, $\mathcal{R}_{\mathcal{B}}$, $\mathcal{S}$).
4. A size filter is applied to the connected components of the vesselness image (pixel count threshold).
5. Centre points for components resulting from Step 4 are calculated.
6. Lines are fitted to the centre points using hop-along algorithm.
7. The main stem is estimated using the Hough transform on the centre points.
8. Lines are projected to the main stem to identify candidate nodes.

### 4.12.2 Algorithm for night time infrared images

Images were also collected at night with near infrared illumination. This produced images in which the vegetation in front of the camera enclosure appeared bright and other foliage and background material appeared dark (Figure 4.24(a)). The algorithm developed thus far only detected dark lines. Hence, either the algorithm or the input image needed to be modified so that the algorithm could analyse images in which foliage appeared lighter than the background. This was achieved by implementing the following two extra preprocessing steps for the night time infrared images:

1. Invert the green channel of the image (Figure 4.24(b)).
2. Adjust the image contrast (Figure 4.24(c)).

The remaining line detection steps remained unchanged (Figures 4.24(d) and (e)).

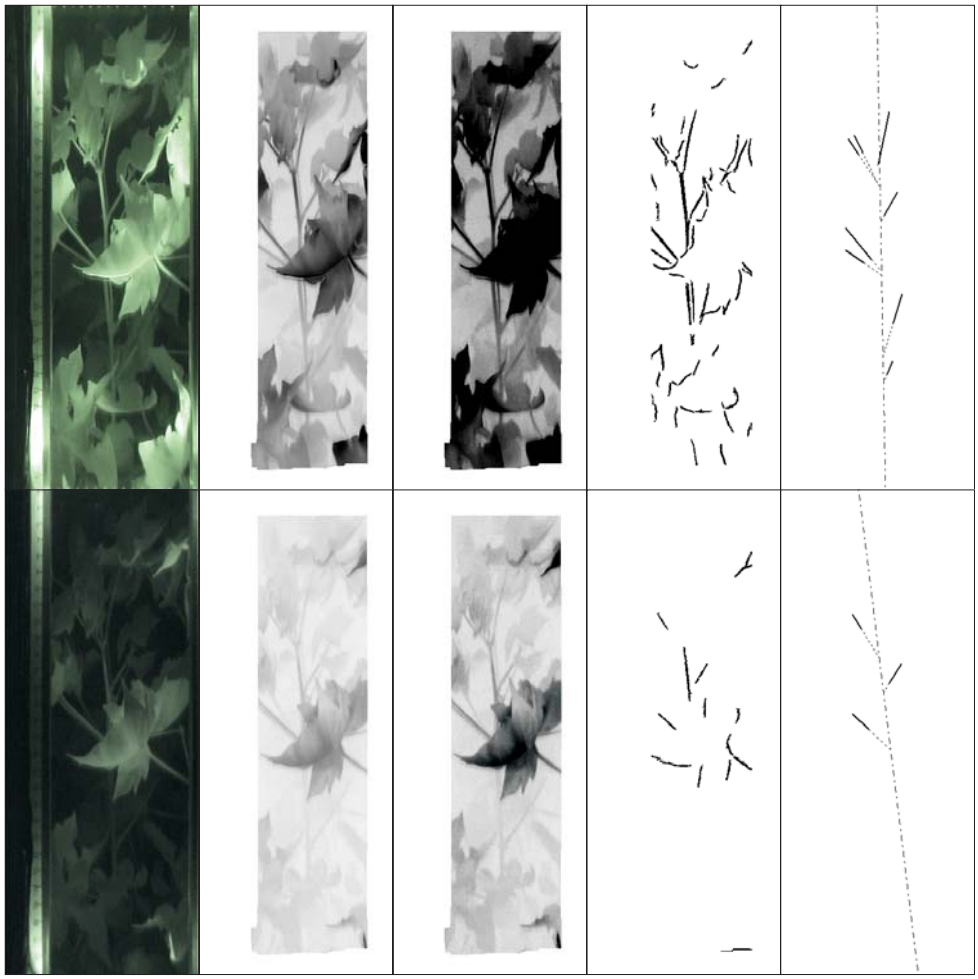

(a) (b) (c) (d) (e)

Figure 4.24: Image processing steps for night time near infrared images, for illumination at 850 nm (row 1) and 940 nm (row 2). For each row: (a) input green channel image; (b) inverted green channel; (c) intensities in the range (50, 255) stretched to the range (0, 255); (d) size filter on vesselness image; and (e) fitted lines.

## 4.13 Single frame algorithm evaluation

### 4.13.1 Results

Typical candidate node detection results for Image Sequences 1 to 4 are displayed in Figures 4.25 and 4.26. In individual frames, both correct and incorrect ('false positive') nodes were detected, with correctness (or otherwise) determined by visual frame-by-frame inspection. There were a large number of falsely identified nodes evident in the plots, with approximately 22% of detected nodes being false positives (Figures 4.25 and 4.26). However, several node trajectories were consistently detected.

The top two or three nodes were generally not detected as a result of the adjoining branches being too short to be detected. Longer branches were overlooked when the branch was sunlit (e.g. node 4 of Image Sequence 3) or near-parallel to the main stem (e.g. node 5 of Image Sequence 2). Bright branches were not detected because the current automated node identification process only targets dark lines. However, node positions were estimated for node 4 of Image Sequence 2 despite the node being occluded for the second half of the sequence. The scatter and multiplicity of individual candidate nodes (e.g. node 4 of Image Sequence 1 and node 3 of Image Sequence 3) were identified to be caused by non-homogeneously-sloped lines being projected to the main stem, due to the nodes adjoining branch and petiole both being projected to the main stem, or curved branches being detected as a series of disjointed line segments (Figure 4.27).

Clearly, the existence of false positives between correctly identified adjacent nodes and the multiple responses to single nodes prevent the reliable automated measurement of internode length at the individual frame level. However, the accumulation of candidate node positions for a whole video sequence (e.g. Figures 4.25 and 4.26) enables the observation that overall, the trend in candidate node positions for the whole video sequence follows the positioning of the manually identified node trajectories (i.e. true nodes were generally reliably detected over multiple frames). This potentially enables a time sequence of candidate nodes to be used to improve confidence in candidate node

detection for individual frames. The use of trajectory tracking across successive frames is investigated in Chapter 5.

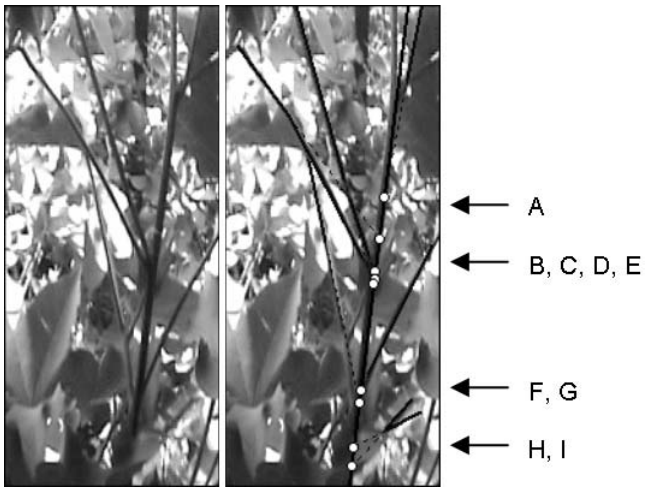


Figure 4.27: Typical node identification results on Sample Image 1. Left: Input green channel image. Right: Automatically detected candidate nodes (white discs labeled in descending order A–I). A is an inaccurate projection to the main stem; B, C, D and E are multiple responses to a single node; F and G are accurate projections to the main stem; and H and I are false positives. The main stem deviates from a straight line at the top of the image.

### 4.13.2 Analysis of erroneous node omission

The three major sources of erroneously-omitted candidate nodes in the current algorithm were identified as follows.

**Nodes adjoined only by bright/sunlit branches.** The Hessian eigenvalues yielded distinct responses for dark and light lines (as evident in Table 4.1). Only dark lines were targeted in the line identification step, since the plant generally falls into shadow when contacting the transparent panel. However, branches appeared light if they protruded away from the transparent panel and hence did not fall into shadow. Further algorithm development or shading of the camera enclosure (such that all branches in front of the window appear dark) could refine the line identification process.

**Short branches.** Size filters were used throughout the image processing as a measure to reduce the incidence of false positives, but this caused some false negatives. Hence, identification of false positives by criteria other than size alone is required.

**Branches near-parallel to main stem.** Estimating a node position from the geometric intersection of the main stem with a branch of similar incline was likely to result in overshooting of the true node position. Hence, branches near-parallel to the main stem were automatically omitted from estimating candidate nodes. Further algorithm development consisting of branch shape modeling close to the main stem is expected to overcome this limitation.

## 4.14 Conclusions

This chapter has evaluated potential techniques for the automated identification of internode length from video imagery collected from a moving, infield camera enclosure. Manual (screen-based) identification of nodes in collected imagery yielded standard errors of 1.4 mm in internode length measurement, which verified the viability of using the fixed object plane at the front of the camera enclosure for geometric measurement.

Automatic identification of internode length was considered for four image sequences captured from the camera enclosure. Techniques evaluated for automatic node identification on single frames included colour and shape analysis. The excess green criterion was not effective at isolating foreground stems from other foliage since the stems and other foliage were all green in colour. However, by visual inspection, the green channel of collected images provided the most contrast between foreground stems and other material. Hence, the green channel was used in the remaining image processing evaluations. The use of colour information to extract nodes from imagery was further tested using adaptive thresholding about the main stem. However, this method was not effective due to the overlap in intensities exhibited by nodes and other foliage behind the main stem.

Edge detectors were found to be of limited applicability for node detection because both branch edges, and edges caused by randomly-oriented leaf edges, yielded strong responses. However, line detection via the vesselness transformation was identified as useful for accentuating branch pixels because the vesselness response to branches consisted of large connected regions of 'on' pixels, whereas the vesselness response to leaf areas was a more sparse and disconnected distribution of pixels. Hence, a size filter could be used to discriminate branch pixels from the leaf pixels.

Nodes adjoined by long, shadowed branches were reliably detected using the derived method. However, the existence of false positives between correctly identified adjacent nodes and the multiple responses to single nodes prevented the reliable measurement of internode length at the individual frame level. Therefore the potential to extract node trajectories from sequential images for internode length measurement was evaluated and is reported in Chapter 5.

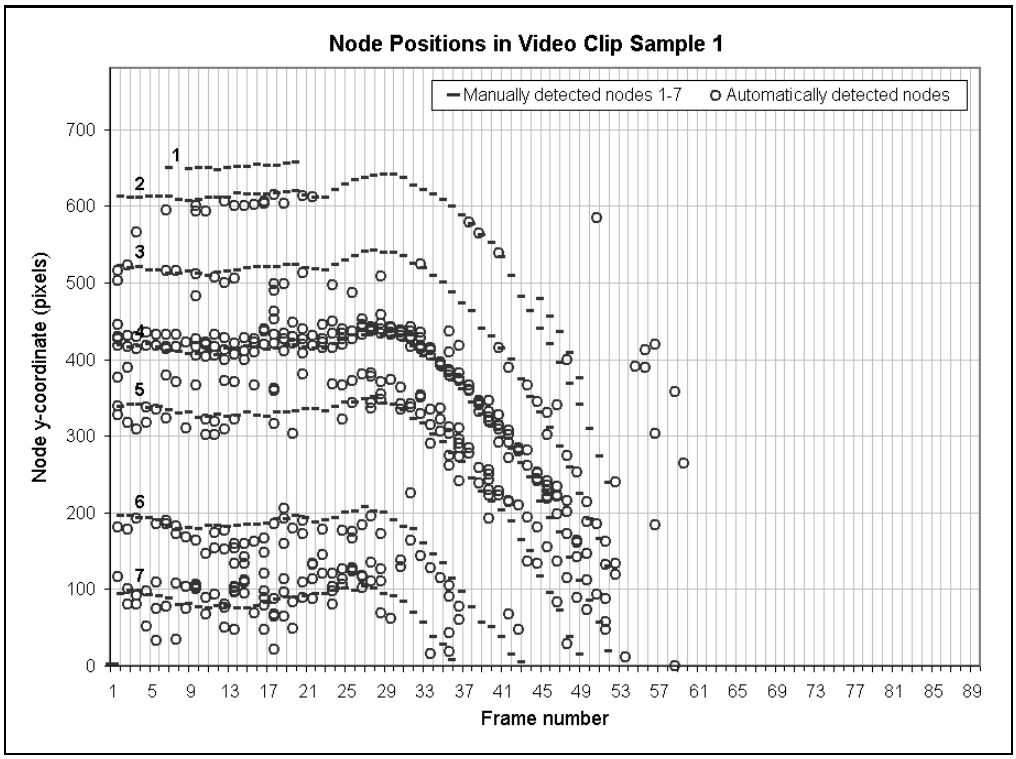


(a)

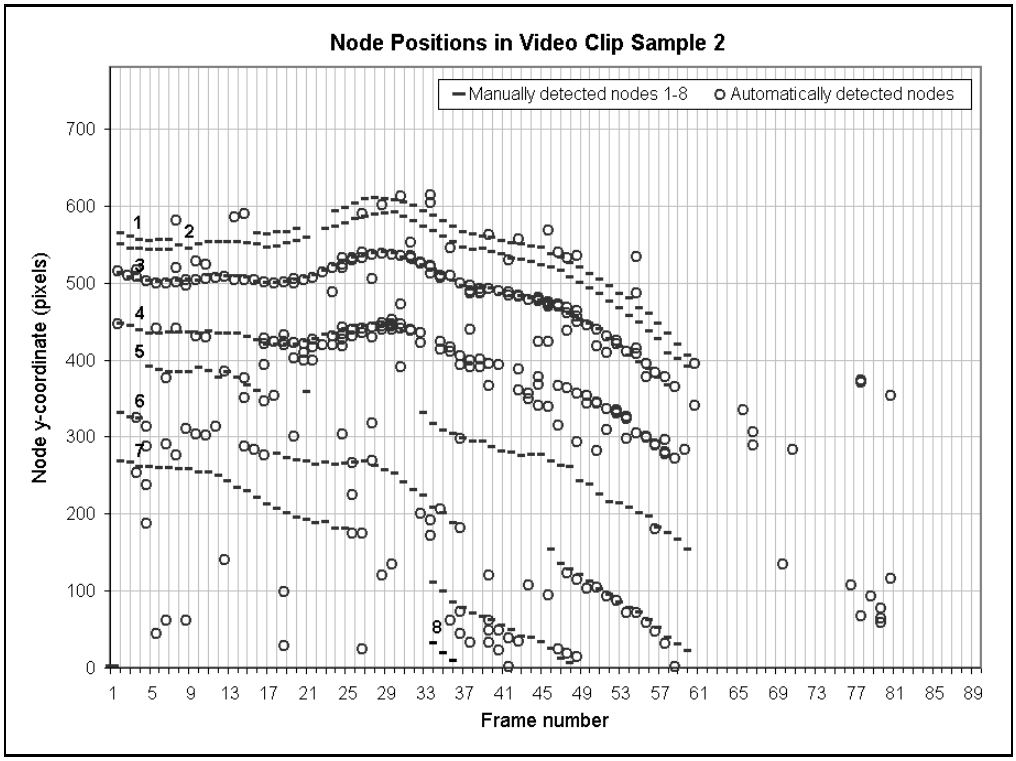


(b)

Figure 4.25: Automatically detected nodes for: (a) Image Sequence 1; and (b) Image Sequence 2.

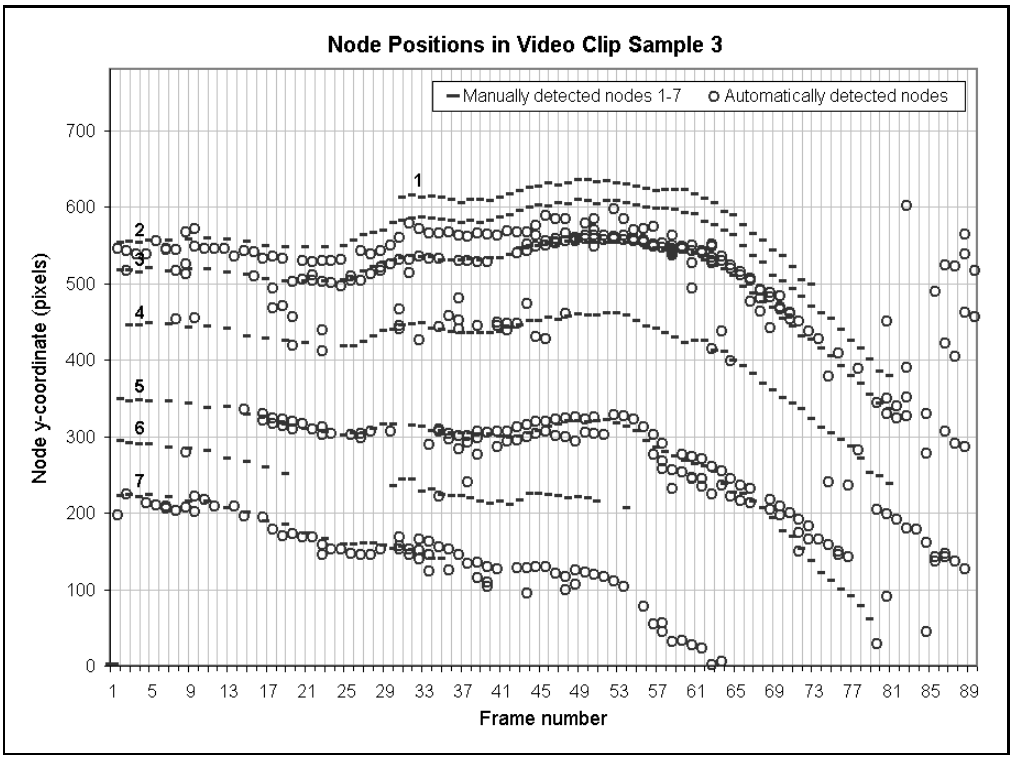


(a)

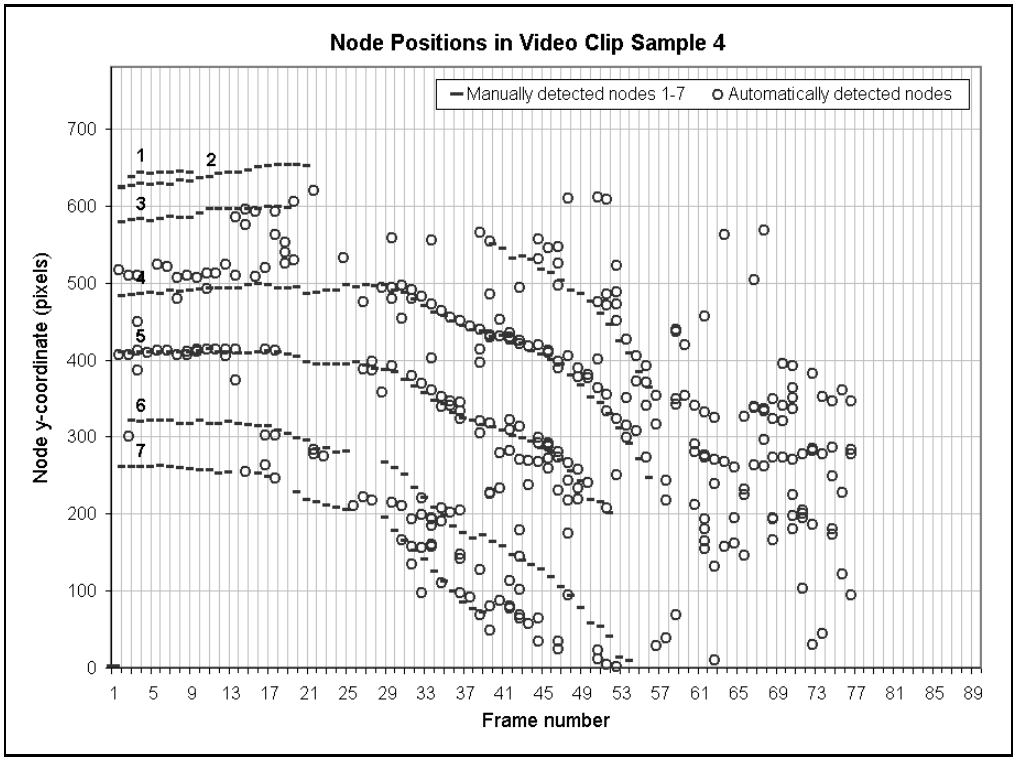


(b)

Figure 4.26: Automatically detected nodes for: (a) Image Sequence 3; and (b) Image Sequence 4.

# Chapter 5

# Node tracking across sequential frames

## 5.1 Introduction

The preceding chapter discussed the detection of candidate nodes in individual frames of a video sequence. However, the process was susceptible to detection of false nodes for which no reliable scheme to exclude them could be devised. Hence, reliable internode length measurement from a single image was not possible. Sequential image analysis was therefore evaluated as a technique to identify candidate nodes as either transient false positives or true nodes.

In principle, the nature of the tracking algorithm for nodes on a plant is not complex if true nodes are reliably detected and the false nodes ('false positives') are relatively few. In the absence of wind or other external forces, the plant is a stationary object that undergoes predictable movement when it comes into contact with the moving camera enclosure. Sequential images are available at $\frac{1}{25}$ s intervals, hence each frame will (normally) be quite similar to its predecessor. Clearly, the node positions remain fixed with respect to the main stem. Hence, the tracking algorithm does not need to

account for random or unpredictable motion and may incorporate some pre-emption or extrapolation for node trajectories. However, algorithms developed for single frame node detection (Chapter 4) typically yielded reliable true node detection but with a high false positive rate. This error rate is expected to be reduced by the tracking across sequential frames which should also substantially reduce noise.

The following three characteristics of the single frame processing results (Section 4.13) are pertinent to tracking in this application:

1. True nodes were generally reliably detected over multiple frames.
2. False positives occurred at largely random locations within each frame, and did not reappear over a large number of sequential frames.
3. A true node may have yielded multiple responses within a single frame, and these needed to be recognised as multiple responses to a single node (as described in Figure 4.27).

Options for forming node trajectories are discussed in the following sections. These are:

1. tracking individual branches or petioles (i.e. line segments) by active contour models and matching line parameters (Section 5.2);
2. tracking candidate node positions including pre-emption of node position (Section 5.3); and
3. grouping candidate nodes into trajectories based on morphological dilation and data point mesh spacing (Section 5.4).

The most success was obtained by grouping candidate nodes (Section 5.4). Finally, this chapter presents the algorithm used to calculate internode length from detected candidate node trajectories (Section 5.5).

## 5.2 Tracking line segments

### 5.2.1 Active contour (or snake) model

The active contour model is an iterative method of contour tracking, in which a contour (snake) attaches to a feature in an image and then minimises an 'energy' function of the contour, based on an initial estimate of the feature's position. The snake's energy components are (Kass et al., 1987):

- **image energy** $E_{img}(\vec{v})$ such as image intensity or edges, or any transformation of the image which yields a strong response to the features of interest;
- **internal energy** $E_{int}(\vec{v})$ such as geometric constraints on snake length and smoothness (analogous to elastic and bending forces, respectively); and
- **external energy** $E_{ext}(\vec{v})$ such as spring forces which define the contour's attraction/repulsion to prescribed regions of the image.

The input image is usually blurred so that sharp edges become graduated, which assists the snake in 'latching' onto the feature. Convergence of the contour occurs when the contour points change by some suitably negligible amount from one iteration to the next. Noisy pixels in the image energy function (i.e. strong response to features not of interest, or weak response to features of interest) can potentially cause the snake to behave unreliably, such as settling on an unexpected contour, or failing to converge on any particular image feature in which case the snake may iterate indefinitely. In standard edge detection results, where both stem and leaf edges yield strong responses, there is potentially a lot of noise when the active contour model is required to converge onto stem edges alone.

The snake's total energy $E$ is described mathematically as follows:

$$E(\vec{v}) = E_{img}(\vec{v}) + E_{int}(\vec{v}) + E_{ext}(\vec{v}) \tag{5.1}$$

where the vector $\vec{v}$ contains the contour points.

The values for $E_{img}(\vec{v})$ are taken from an input image (e.g. edges or vesselness), and $E_{ext}(\vec{v})$ is set to zero because there is no predefined region of interest in the image. The internal energy is defined as (for example in Laptev et al. (2000)):

$$E_{int}(\vec{v}) = \frac{1}{2}\int_0^1 \left(\alpha(s)\left|\frac{\partial\vec{v}(s,t)}{\partial s}\right|^2 + \beta(s)\left|\frac{\partial^2\vec{v}(s,t)}{\partial s^2}\right|^2\right) ds \tag{5.2}$$

where $\alpha$ is a first-order elasticity function and affects the snake length;
$\beta$ is a second-order bending function and affects the snake smoothness;
$s$ is the normalised distance along the snake's length; and
$t$ is the current iteration number of the snake's position (Kass et al., 1987).

The internal energy of the snake can be discretised to:

$$E_{int}(i) = \alpha_i\frac{|v_i - v_{i-1}|^2}{h^2} + \beta_i\frac{|v_{i-1} - 2v_i + v_{i+1}|^2}{h^4} \tag{5.3}$$

where $h$ is the discretisation step size and $i$ is the step number along the snake's length.

Figures 5.1 and 5.2 demonstrate iterations of an active contour model on a sample image. The input image (or image forces function) is required to exhibit a strong response to the principal feature (i.e. stem edges). Hence, the input image used in this evaluation was the vesselness image of Figure 4.18(d), blurred with a Gaussian filter ($\sigma = 1$) and scaled between 0 and 255. Constant bending ($\alpha$) and elasticity ($\beta$) coefficients were empirically chosen so that the resulting contour had smooth curvature and evenly spaced points.

Active contour models may be used to track features in video sequences, since a contour's final position in one frame may be used as the initial estimate of the contour's position in the next frame. Figure 5.1 shows iterations of a manually-chosen initial contour of arbitrary points offset to the left of the manually-discerned main stem. The contour points were contrained to move towards the bottom right of the image, a simplification that did not affect the evaluation of the contour's ability to settle on significant image features. The contour settled onto the main stem despite a small occlusion in the main stem, five contour points from the bottom of the contour. Automation of

contour initialisation is expected to be achievable by using line segment endpoints and interpolated line points, identified automatically by an image processing algorithm such as that described in Chapter 4.

However, Figure 5.2 is an example of the contour failing to converge on the expected image feature. Whilst this final contour was not grossly erroneous (it did partly converge onto the expected contour), such small contour deviations were not necessarily predictable or typical. Therefore, whilst the active contour technique did show promise, further algorithm development was not pursued since reliable operation of the snake could not be guaranteed using the basic implementation adopted.

(a) (b) (c)

Figure 5.1: Active contour model iterations for main stem segment of vesselness transformation of Sample Image 1 (Figure 4.4), with filled circles indicating contour points: (a) initial contour; (b) after 5 iterations; and (c) final position of snake, after 17 iterations, which closely matches main stem.

### 5.2.2 Matching line parameters

For tracking of points such as candidate nodes, the pixel is parameterised with its x- and y-coordinates. Tracking of line segments, such as candidate branches, requires

(a) (b) (c)

Figure 5.2: Active contour model iterations for branch segment of vesselness transformation of Sample Image 1, with filled circles indicating contour points: (a) initial contour; (b) after 5 iterations; and (c) final position of snake, after 19 iterations, which does not follow expected branch contour.

extra parameters. Deriche & Faugeras (1990) demonstrate that a line segment's midpoint, length and perpendicular distance to the origin constitute the minimum parameters required to match line segments from one frame to the next, and if necessary a noise-removing filter (such as the Kalman filter, described below) is applied to each parameter. Figure 5.3 shows typical results for matching line segments from frame-to-frame, where line segments across frames were declared to be matched if the difference in parameters of both line segments was below a threshold.

In the sample images of Figure 5.3, frequent inaccurate matching of lines was evident since line segment parameters were not predictably inconsistent across frames, despite the line segments forming quite reliable candidate node positions. This was because individual branches were frequently detected as a series of smaller disjointed lines, with variation from one frame to the next in both the number and location of joints. Similar results were obtained for the other sample images of Figure 4.4.

Noise filtering on a feature's position may potentially be used to improve tracking results by estimating variation in detected feature position. A commonly-used filter is the Kalman filter, which is a recursive time-domain filter that assumes there are noise components in both the true and measured positions of an object (Kalman, 1960). Another definition of the Kalman filter is an optimal estimator of the true states of a dynamical process given measurements of those states corrupted with additive zero-mean Gaussian noise (Corke, 2008). The line segment tracking method of Deriche & Faugeras (1990) uses the Kalman filter to improve accuracy in predicting the next frame's value for each line parameter. However, since reconstructing disjointed lines into whole branches was an unnecessary complexity for measuring a plant's internode length, further development of this method was not pursued.

## 5.3 Tracking candidate node positions

Tracking algorithms involve finding a match for detected features over a sequence of frames based on continuity in the feature's motion, i.e. by assuming there are small changes in the feature's position and velocity from one frame to the next. Jain et al. (1995) describe algorithms where smooth trajectories are iteratively searched for within the set of data points. However, the method does not specifically cater for multiple responses to features of interest within a single frame.

Mery & Filbert (2002) describe an algorithm based on the hypothesis that true data points could be reliably tracked while noisy points could not. Their method could reliably track feature points on a fixed-path object from image sequences with up to 500 noisy points per frame. However, their application was in an assembly-line environment where the plane of motion of the object was exactly known and employed in their algorithm implementation.

In the present application, the hypothesis that only correctly identified points can be tracked is valid (Section 4.13), and *a priori* knowledge of the camera enclosure travel

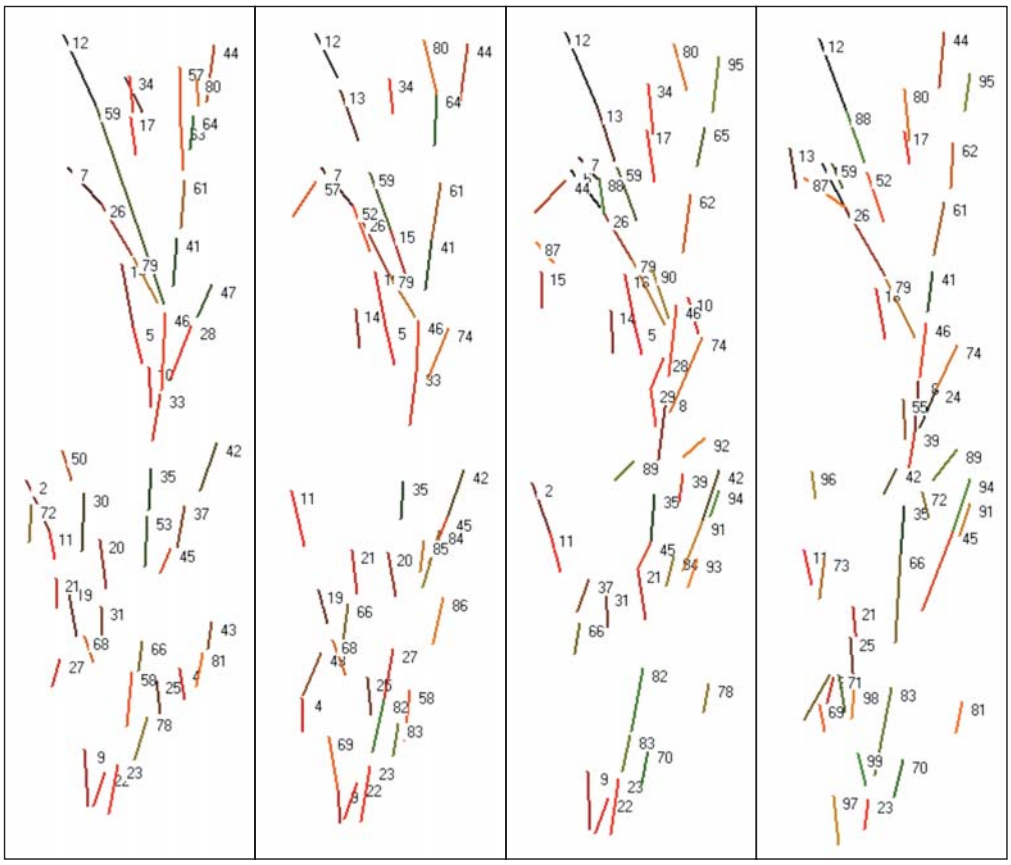

(a) (b) (c) (d)

Figure 5.3: Matching of line segments detected in Image Sequence 1 (Figure 4.4), based on minimising parameter differences in successive frames: (a) frame 29; (b) frame 30 (which corresponds to Sample Image 1); (c) frame 31; and (d) frame 32.

speed (Figure 5.4), plant spacing and current node positions could potentially be combined to enable prediction (i.e. pre-emption) of node positions in future frames. However, it was anticipated that the accumulation of positional uncertainty ensuing from inaccurate node identification and prediction could be avoided by grouping candidate nodes at the end of a whole sequence, as described in the next section. Hence, the techniques of this section's discussion were not implemented in code.

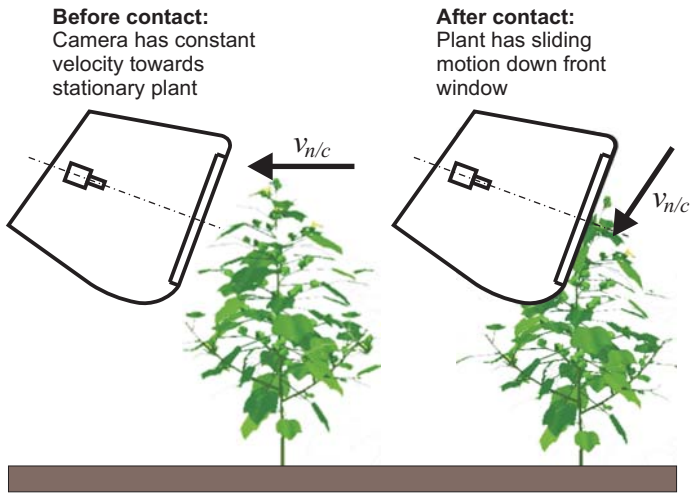


Figure 5.4: Velocity of the plant nodes with respect to the camera ($v_{n/c}$) before and after the camera enclosure contacts the plant.

## 5.4 Grouping candidate node positions

Grouping[1] candidate nodes is distinguished here from matching, since in this section node trajectories are formed by considering clustering[1] patterns in the candidate node data for the whole sequence. Potential for applying grouping algorithms existed because from visual inspection of detected nodes for a sequence (such as the graphs of Figures 4.25 and 4.26), nodes were detected reliably throughout an image sequence with sparse false positives. The techniques described below were applied to the candidate node data accumulated for the whole image sequence. The candidate node positions were stored as pixel y-coordinate $y$ versus frame number $t$ (both integer).

### 5.4.1 Morphological dilation

Node trajectories were formed by grouping a candidate node with any other candidate node within thresholds $\pm\Delta t$ and $\pm\Delta y$ in distance. The process was implemented using a morphological dilation (Serra, 1982) such that each candidate node position (represented as a pixel in $y$-$t$ space) was replaced with a rectangle of size $2\Delta t \times 2\Delta y$

[1]The terms 'grouping' and 'clustering' are used with their general English meanings rather than with any form of specific mathematic definition.

(left-aligned and vertically-centred on the pixel). The resulting connected components formed node trajectories.

The formation of continuous node trajectories required that the threshold $\pm\Delta t$ be large enough to span multiple frames with occlusions, while $\pm\Delta y$ was required to be large enough to exceed frame-to-frame vertical node movement. The value of $\pm\Delta y$ typically ranged from 1 to 15 pixels, depending on how close the camera enclosure was to the plant and how fast the camera enclosure was moving. Further work could potentially have enabled calculation of the value of $\pm\Delta y$ as a function of camera enclosure travel speed and distance between the camera and the plant, in much the same way as pre-emption of node positions (Section 5.3) was expected to operate. However, a limitation of the method was that the thresholds were sensitive to plant-to-plant variations in geometry, such as the length of occlusions and the proximity of false positive candidate nodes to true positive candidate nodes. This caused the automatic trajectory extraction to be unreliable across multiple plants and hence the method was not suitable for automatic measurement in the field.

### 5.4.2 Data point mesh spacing

Plots of candidate nodes automatically detected from image sequences typically featured a dataspace in which there were regions of both closely-packed and sparsely-distributed candidate nodes (e.g. Figure 5.5(a) and (b) for Image Sequence 1). The groups of closely-packed nodes were visually discernible and typically occurred around manually identified node trajectories (Figure 5.5(a)). Hence, automatic grouping of closely-packed candidate nodes was a potential method of forming candidate node trajectories. An algorithm that has been developed to mimic the human behaviour of visual grouping is described in Papari & Petkov (2005), where a 'group' of points in a set is described as a subset containing points that are much closer geometrically to each other than to the other points in the set. The method of Papari & Petkov (2005) evaluates the relative closeness of data points by computing edge lengths of a Delaunay Triangulation (Preparata & Shamos, 1985) of the data points.

Delaunay Triangulation is a meshing method that is commonly used in finite element analysis and function interpolation. For the current application, the set $S$ of data points $x$ for the meshing was given by the candidate nodes for the sequence. A Delaunay Triangulation for the candidate nodes of Image Sequence 1 is shown in Figure 5.6(a).

Papari & Petkov (2005) define a length criterion for determining geometric closeness of data points as follows. For a mesh line between data points $p$ and $q$, the function $\xi(p,q)$ is the length $pq$ normalised with the distance $d(p,q)$ between $p$ and $p$'s nearest connected neighbour $x$, i.e.:

$$\xi(p,q) = \frac{d(p,q)}{\min\limits_{x \in S} \{d(p,x)\}} \tag{5.4}$$

This same calculation is repeated for the $q$ endpoint of the line, i.e. $\xi(q,p)$. The length criterion is a threshold on the geometric mean of $\xi(p,q)$ and $\xi(q,p)$. Groups identified by this method are illustrated in Figure 5.6(b), which by visual inspection corresponded well to the true node trajectories.

The aspect ratio for visual representation of node position versus frame number was important for the automatic grouping algorithm, as it was for visual perception of trajectory membership across an image sequence. Graphs of node y-position versus frame number with equal vertical and horizontal scales were skewed in the vertical direction, since y-coordinates were in the range 1 to 700 while frame number only ranged from 1 to typically 80. This makes separate node trajectories difficult to discern visually. Figure 5.7 shows the Delaunay Triangulation for the candidate node data with different aspect ratios, where the triangles are elongated horizontally for the lower scaling factors on node y-position. Hence, before computing the Delaunay Triangulation of the data points, the node y-coordinates were scaled by $80 \div 700 \approx \frac{1}{9}$ to yield more proportioned data ranges. This is comparable with the aspect ratio of the graphs in Figure 5.5, where the node y-coordinates were scaled by $\frac{1}{13}$ relative to the x-axis.

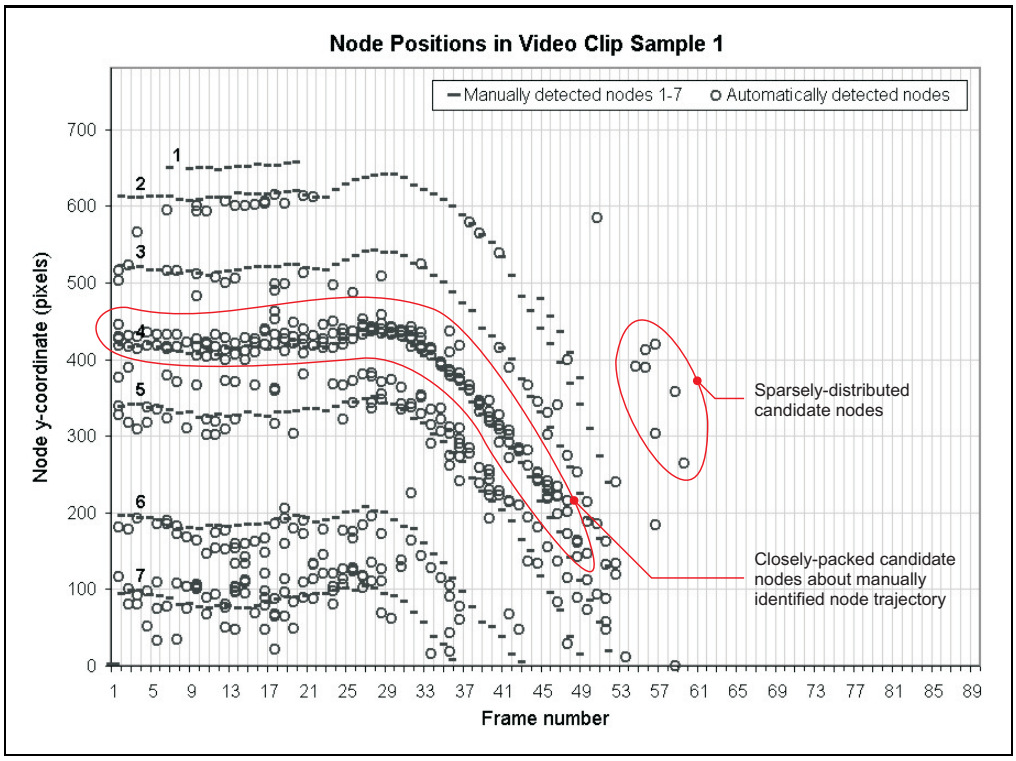


(a)

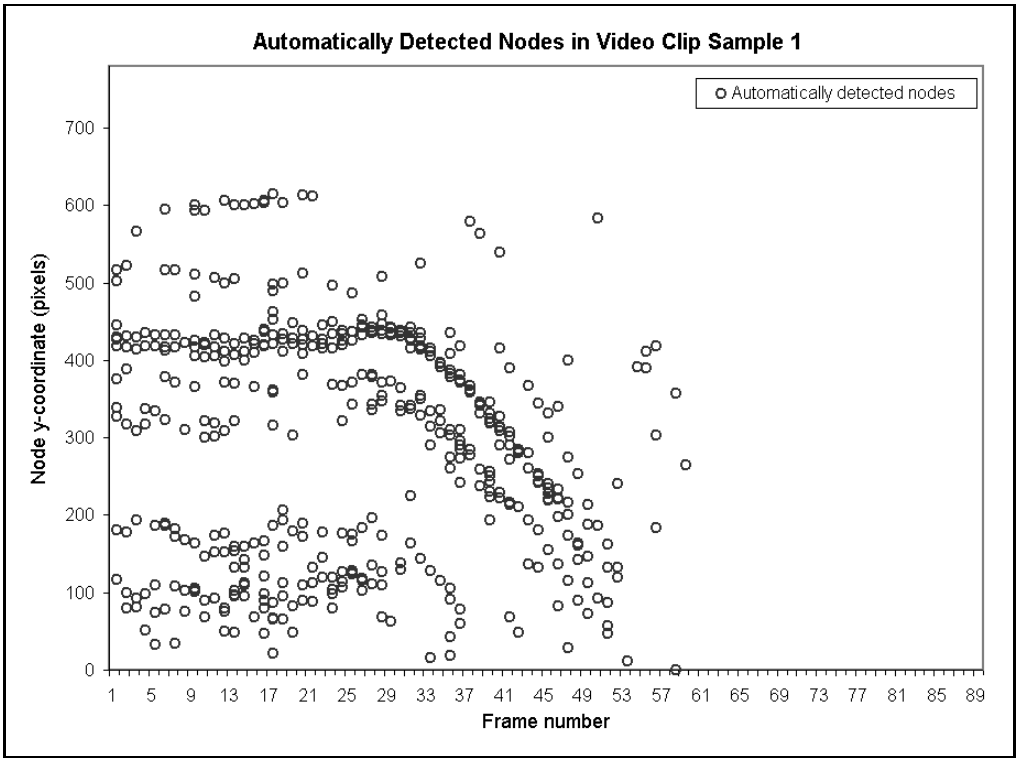


(b)

Figure 5.5: Automatically detected nodes for Image Sequence 1: (a) automatically detected nodes superimposed on manually detected nodes; and (b) automatically detected nodes.

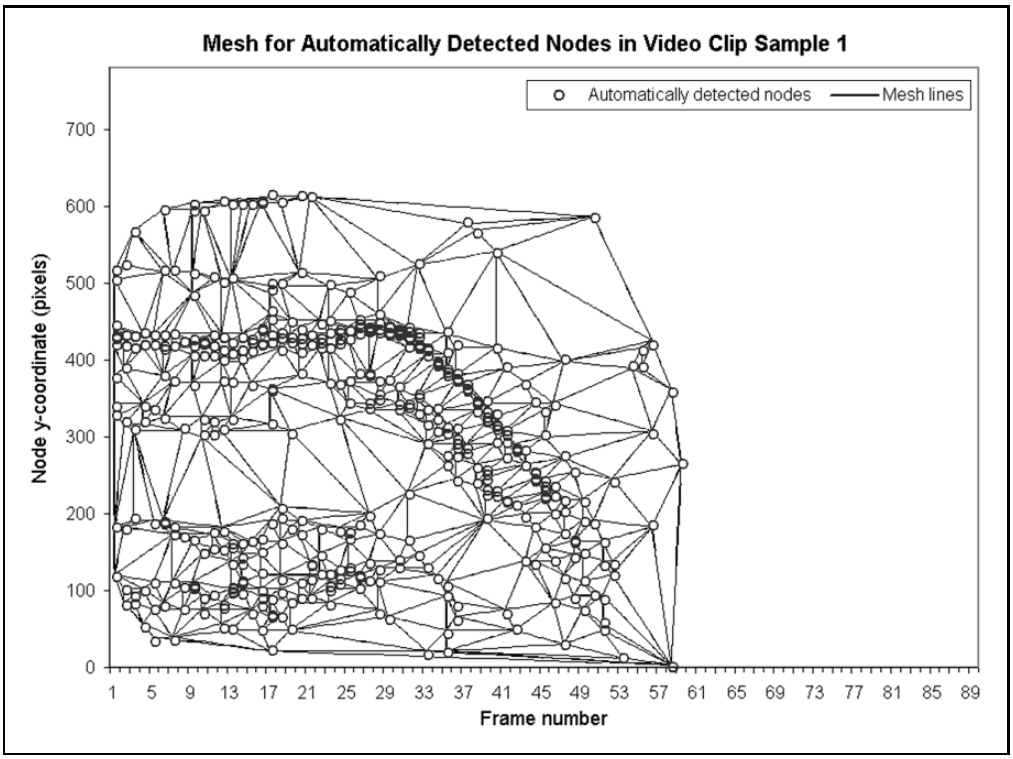


(a)

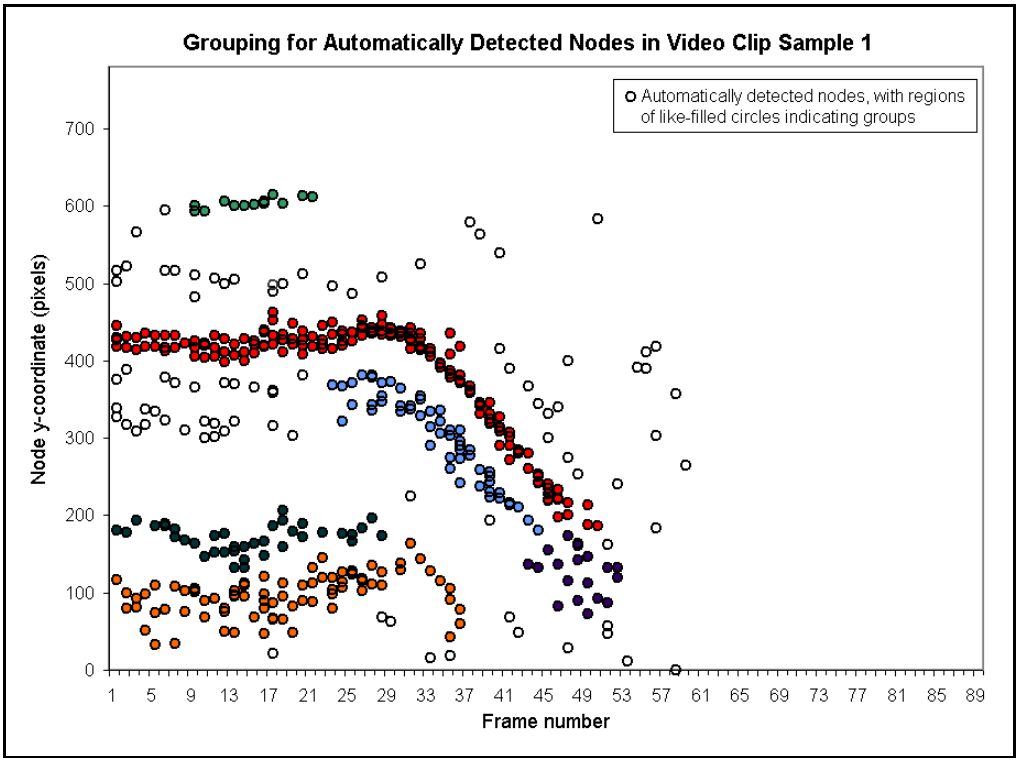


(b)

Figure 5.6: Automatic grouping of candidate nodes for Image Sequence 1: (a) Delaunay Triangulation of automatically detected nodes of Figure 5.5(b); and (b) candidate node grouping according to the method of Papari & Petkov (2005).

## 5.5 Calculation of internode length from node trajectories

The final step in calculating internode length was to generate an automatic process to identify the maximum distance between adjacent node trajectories. A smooth, continuous, single-pixel-thick trajectory was formed for each node group (identified by the process of Section 5.4.2) by replacing the detected candidate nodes in each frame with a single average detected node position. The average node position was then smoothed across the whole sequence to form candidate node trajectories, using a passive (i.e. gain between zero and one) low pass filter of the form (also known as an exponential moving average):

$$y_{smooth}[t] = \alpha \cdot y_{smooth}[t-1] + (1-\alpha) \cdot y[t] \tag{5.5}$$

where $y_{smooth}[t]$ is the smoothed node position at time $t$;

$y[t]$ is the averaged node position at time $t$; and

$\alpha$ is a smoothing factor between zero and one, chosen to yield smooth looking trajectories ($\alpha = 0.2$).

Adjacent nodes determinations (Figure 5.8) were required to be identified from the data space $y$-$t$ of smoothed node positions. Stylised node trajectories corresponding to Image Sequences 1 to 4 are included in Figure 5.9 (based on node detection results of Figures 4.25 and 4.26). Grey-shaded regions of Figure 5.9 indicate frames for which candidate node data is available for adjacent candidate node trajectories, thus enabling internode measurements between those adjacent candidate node trajectories.

The algorithm steps for determining maximum internode distance between adjacent node trajectories is explained below with reference to Figure 5.9. Pseudocode for the process is included in Appendix D.2.2.

1. Each pair of adjacent node determinations in adjacent frames formed a vertical trapezium with width $\Delta t = 1$ in $y$-$t$ space (Figure 5.8). Stepwise progression through node positions for the complete image sequence yielded trapeziums with common properties which could then be grouped to form the regions A–F of Figure 5.9. 'Successive' node trajectories were separated from non-successive

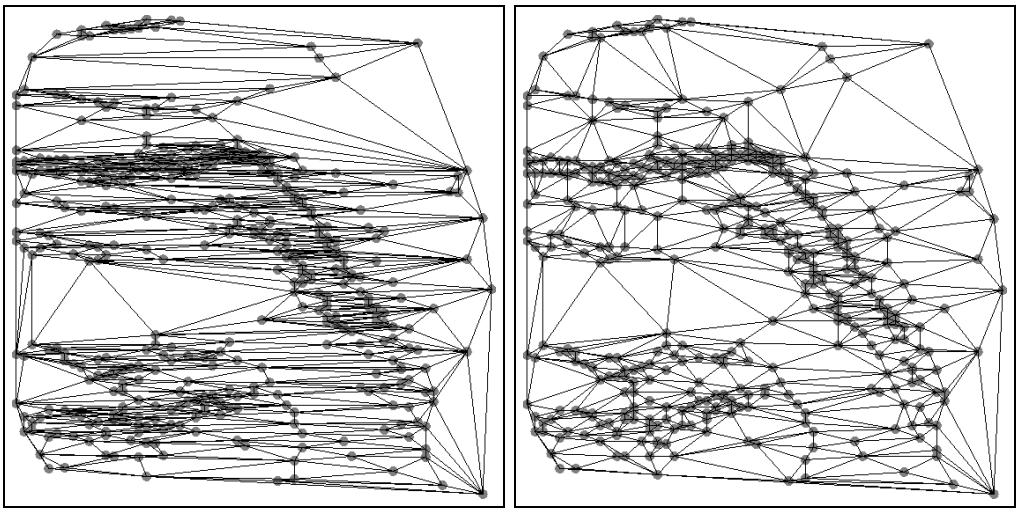

(a) (b)

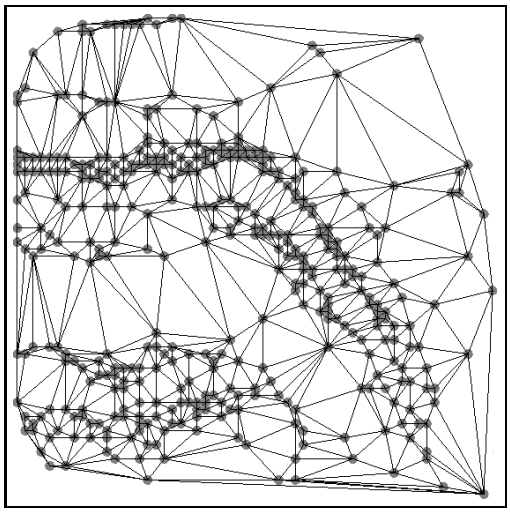

(c)

Figure 5.7: Delaunay Triangulation of candidate node data points of Image Sequence 1 for different y-scales, with a relative x-scale of 1: (a) 1; (b) $\frac{1}{4}$; and (c) $\frac{1}{9}$. The triangulations are rendered into square images in this figure.

trajectories by removing those trapeziums which featured a longer vertical edge than the neighbouring trapeziums. In Figure 5.9 trapeziums corresponding to adjacent but not successive pairs of node trajectories are represented with a hatched fill.

2. The maximum $\Delta y$ for each grey-shaded region of Figure 5.9 corresponds to the maximum internode distance between each pair of detected successive node trajectories. These maximum $\Delta y$ values were used in Equation 4.1 to calculate internode distance in millimetres.

## 5.6 Conclusions

Node trajectories were required to be formed from candidate node positions to enable internode distance measurement for an image sequence. However, line segment tracking was found to introduce unnecessary complexity to the node trajectory identification task, whilst candidate node tracking was expected to introduce positional errors into identified node trajectories.

A grouping algorithm that made use of the high concentration of candidate nodes detected close to the position of true node trajectories was adopted (Papari & Petkov, 2005). This method was successful at identifying node trajectories in Image Sequences 1 to 4. Regions of overlap between adjacent detected node trajectories were successfully determined for Image Sequences 1 to 4 using a stepwise process. The algorithm's performance at measuring internode distance is evaluated in the next chapter.

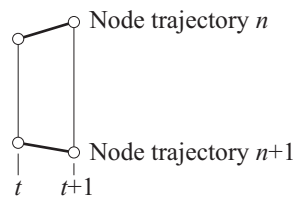


Figure 5.8: Trapezium in $y$-$t$ space representing adjacent nodes detected at times $t$ and $t+1$.

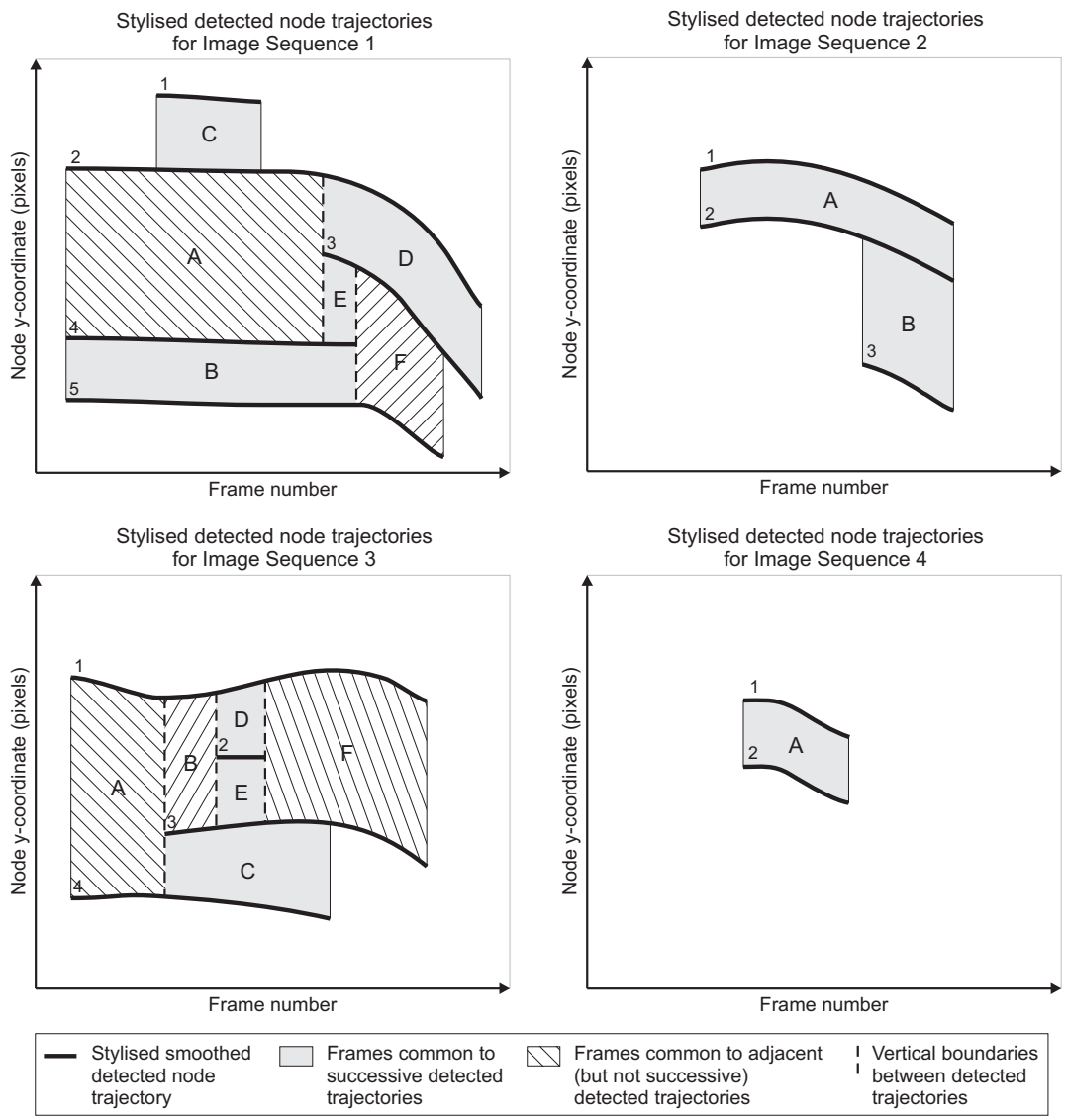


Figure 5.9: Graphical representation of the algorithm used to distinguish pairs of successive node trajectories from pairs of non-successive node trajectories. The shaded regions labeled with the letters A–F correspond to frames common to adjacent node trajectories. The labels 1–5 correspond to detected trajectories.

# Chapter 6

# Evaluation of performance

## 6.1 Introduction

Image processing algorithms for automatic internode length measurement have thus far been evaluated on images from the four sequences described in Chapters 4 and 5. However, other data sets were collected with varying environmental and agronomic factors, and apparatus configurations. This chapter presents an evaluation of the performance of the system under a range of conditions and identifies some current limitations of use of the measurement technique.

## 6.2 Field data collection

The machine vision system was used to collect video footage of cotton plants during crop flowering of the 2005/06 and 2006/07 Australian cotton growing seasons. System repeatability was evaluated by collecting three replications of video sequences for every treatment. Treatments included camera enclosure orientation ('Orientation' in Table 6.1) and speed for along row operation (which comprised greater plant density than across row operation). The different data sets are listed in Table 6.1. Apparatus

calibration between data sets consisted of verifying the height and pitch angle of the camera enclosure (as described in Section 3.6). A damp cloth was used to clean dust from the window at the front of the camera enclosure before data collection.

Table 6.1: Data sets for evaluation of the measurement technique.

| Data Set | Number of plants | Cultivar | Age (WAP*) | Date (Season) | Evaluation |
|---|---|---|---|---|---|
| 1 | 14 | Sicot 80B | 10 | 08-02-06 (2005/06) | Orientation |
| 2 | 16 | Sicot 289B | 11 | 21-02-06 (2005/06) | Orientation |
| 3 | 10 | Sicot 71B | 9 | 30-01-06 (2005/06) | Orientation |
| 4 | 10 | Deltapine 408B | 9 | 30-01-06 (2005/06) | Orientation |
| 5 | 13 | Sicot 608B | 11 | 02-02-07 (2006/07) | Speed, night, depth of field |

*weeks after planting

### 6.2.1 Fieldwork for 2005/06 season

Data Sets 1 to 4 were collected with a different cotton cultivar featured in each data set (Table 6.1). The following camera enclosure orientation test was carried out on each data set with the manually conveyed camera enclosure, using natural lighting, an enclosure travel speed of 0.30 m/s and the Sony camcorder (Chapter 3) for image capture:

1. Camera enclosure orientation (Figure 6.1)
    - camera enclosure approach angles of 0° and 180°, with yaw angle of 0°
    - camera enclosure approach angles of 0° and 180°, with yaw angle of 45°

### 6.2.2 Fieldwork for 2006/07 season

Data Set 5 was collected using the automatically conveyed camera enclosure. The following operational tests were undertaken:

1. Day/night and illumination for camera enclosure approach angles of both 0° and 180° (Sony camcorder)
    - daytime natural sunlight illumination

- daytime illumination using white LEDs
- night time illumination using white LEDs
- night time illumination using 850 nm LEDs
- night time illumination using 940 nm LEDs

2. Narrow depth of field for camera enclosure approach angles of both 0° and 180° (Prosilica firewire camera)

3. Camera enclosure speeds of 0.10, 0.20, 0.25 and 0.30 m/s along 30 m of the row (Sony camcorder; Figure 6.1)

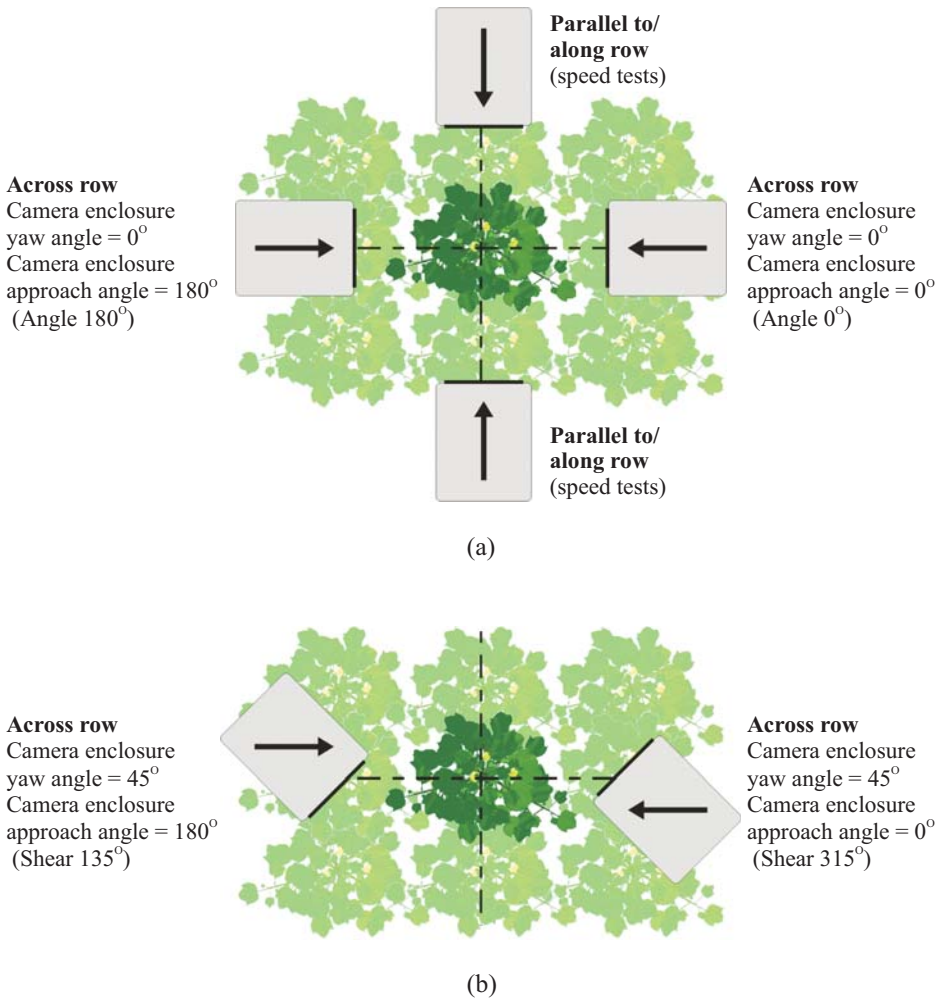


Figure 6.1: Tested camera enclosure orientations: (a) across and along row, with yaw angle of 0°; and (b) across row, with yaw angle of 45°. Angle 0°, Angle 180°, Shear 135° and Shear 315° are labels for the orientation treatments.

## 6.3 Overall system performance

The measurement technique is evaluated on Data Set 1 as an overall indication of system performance because the algorithm was developed using frames from this data set and hence, should be most favourable for measurement. From the 168 video sequences of the fourteen plants, 95 internode lengths were automatically detected which equates to an average measurement rate of one internode length per 1.75 plants. The 95 internode length measurements and their corresponding manual measurements (as described in Section 4.2) are graphed in Figure 6.2. The 95% confidence interval on the regression equation yields the following, which is not significantly different from $y = x$ at the 0.05 level of significance:

$$y = -0.5\,(\pm 6.3) + 1.006\,(\pm 0.085)\,x. \tag{6.1}$$

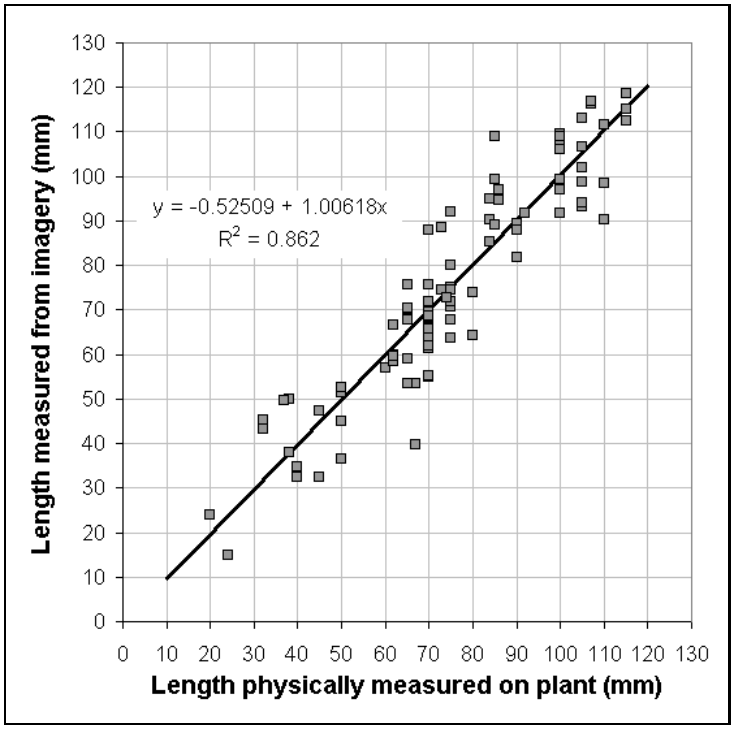


Figure 6.2: Comparison of internode length measurement by automatic image processing and manual field measurement (regression line shown).

The 95 automatic internode length measurements were obtained across a total of 39 physical internodes. Of those 39 internodes, 17 yielded automatic measurements for

$\geq$3 replications, i.e. 17 internodes were usable for standard error calculations. The standard errors on each of those 17 internodes ranged from 1.1 mm to 5.7 mm, with an average of 3.0 mm. Absolute errors ranged from 0.1 mm to 27.4 mm, with a mean absolute error of 6.9 mm and a median of 5.3 mm. The detection rate on any particular plant varied from zero to three internode lengths using the current algorithm.

Automatically measured values for internode length were not significantly different from the manually measured values, despite the field observation that some plants did not completely flatten against the transparent panel at the front of the camera enclosure. The number and quality of measurements varied between replicates primarily as a result of leaves causing occlusion of the main stem for some replicates and not for others. This was determined from visual inspection of the video. There is no bias in the distribution of measurements due to the best estimate of the internode distance being taken as the maximum distance between detected node trajectories (Section 5.5).

The overall system results indicated that the variation in both detection rate and measurement accuracy between replicates was high. However, the effect of different treatments was expected to be more identifiable from variation in the number of measurements made, rather than from variation in the quality of those measurements. Therefore, number of measurements made was identified as an appropriate dependent variable for subsequent evaluations.

## 6.4 Evaluation of apparatus operational factors

### 6.4.1 Camera enclosure orientation versus internode position

In Data Set 1, three replications of video data were collected for each plant with a camera enclosure approach angle of 0° or 180°, for yaw angles of either 0° or 45° (Table 6.2). An analysis of variance (Gomez & Gomez, 1984)(Table 6.3) on this data showed that there was a significant ($P \leq 0.05$) difference in the number of internode

lengths detected with respect to different internode positions (i.e. Internode 0-1, 1-2, ..., 4-5, Figure 4.2) and a significant ($P \leq 0.10$) interaction between the internode position detected and camera enclosure orientation. However, there was no significant difference in the number of internode lengths detected for different camera enclosure orientations. This suggests that the camera's orientation relative to the sun's position during data collection of Data Set 1 had no effect on the number of measurements made by the vision system and that the shearing versus bending motion of the plant induced by the camera enclosure orientation did not influence node detection in the imagery.

Comparison of the mean number of internode lengths detected (Table 6.4) showed that the most commonly detected internode positions were Internodes 2-3 and 3-4. By inspection of analysed images, these internode positions were commonly adjoined by long petioles or branches that were readily detected by the image processing algorithms. At the other end of the scale, the least-detected internode positions were Internodes 4-5 and 0-1. By inspection of analysed images, Internode 0-1 was frequently occluded by the node's adjoining leaf, since the node's petiole was comparatively short and theadjoining leaf was physically closer to the main stem. Node 5 commonly fell out-of-frame, which precluded Internode 4-5 from being automatically measured. A different camera enclosure design would be required to enable lower within-canopy movement to view the lower internodes, because of the more rigid branching structure closer to the ground. There was no interaction between number of internode lengths detected and camera enclosure orientation for Internodes 0-1, 1-2 and 4-5 (Table 6.5). However, camera enclosure orientation did impact on the number of measurements detected at Internodes 2-3 and 3-4 (Table 6.5).

Mean absolute errors of internode length measurement for the different camera enclosure orientations and internode positions are presented in Table 6.6. Quality of measurement is considered for camera enclosure orientation treatments to determine whether the shearing rather than bending motion of the plant associated with varying camera enclosure orientations (as described in the discussion of the camera enclosure yaw angle in Section 3.6) affected the fixed object plane assumption. The missing data in

Table 6.2: Number of internode lengths detected for different camera enclosure orientations (Figure 6.1) and different internode positions for Data Set 1, with three replications.

| Internode position | Replicate | Number of internode lengths | | | |
|---|---|---|---|---|---|
| | | Angle 0° | Angle 180° | Shear 135° | Shear 315° |
| Internode 0-1 | I | 1 | 1 | 0 | 0 |
| | II | 0 | 2 | 0 | 0 |
| | III | 0 | 0 | 0 | 0 |
| Internode 1-2 | I | 1 | 4 | 2 | 2 |
| | II | 1 | 0 | 1 | 1 |
| | III | 1 | 2 | 0 | 0 |
| Internode 2-3 | I | 6 | 2 | 3 | 1 |
| | II | 4 | 4 | 4 | 3 |
| | III | 2 | 5 | 1 | 1 |
| Internode 3-4 | I | 2 | 0 | 3 | 3 |
| | II | 6 | 1 | 2 | 2 |
| | III | 3 | 0 | 2 | 1 |
| Internode 4-5 | I | 3 | 0 | 2 | 2 |
| | II | 1 | 2 | 2 | 2 |
| | III | 0 | 0 | 1 | 0 |

Table 6.3: Analysis of variance for the detected internode position and camera enclosure orientation ('Orientation') treatments.

| Source of variation | Sum of squares | Degrees of freedom | Mean square | Computed $f$ | Critical $f$ | |
|---|---|---|---|---|---|---|
| | | | | | 5% | 10% |
| Internode position | 47.67 | 4 | 11.92 | 8.03** | 2.61 | 2.09 |
| Orientation | 7.65 | 3 | 2.55 | $1.72^{ns}$ | 2.84 | 2.23 |
| Interaction | 33.93 | 12 | 2.83 | 1.91* | 2.00 | 1.71 |
| Error | 59.33 | 40 | 1.48 | | | |
| Total | 148.58 | 59 | | | | |

** = significant at 5% level, * = significant at 10% level, $^{ns}$ = not significant.

Table 6.6 prevented an analysis of variance for interaction effects between all camera enclosure orientations and internode positions. However, an analysis of variance for all orientation treatments of Internode 2-3 (Table 6.7) and for three of the orientation treatments for Internodes 2-3 and 3-4 (Table 6.8) revealed no significant differences in mean absolute error in internode length measurements between treatments. Hence, the measurement system did not yield significantly different accuracies for the shearing and bending motions of the camera enclosure over the plant.

Table 6.4: Least significant differences for all possible pairs of detected internode positions.

| Internode position | Mean number of internode lengths*† |
|---|---|
| Internode 2-3 | 3.00 |
| Internode 3-4 | 2.08 |
| Internode 1-2 | 1.25 |
| Internode 4-5 | 1.25 |
| Internode 0-1 | 0.33 |

*Averaged across four camera enclosure orientations and three replications.
†Any two means connected by the same vertical line are not significantly different at the 1% level of significance.

Table 6.5: Least significant differences for comparing pairs of camera enclosure orientation means at the same internode position.

| Internode position | Mean number of internode lengths*† | | | |
|---|---|---|---|---|
| | Angle 0° | Angle 180° | Shear 135° | Shear 315° |
| Internode 0-1 | $0.33^{a}$ | $1.00^{a}$ | $0.00^{a}$ | $0.00^{a}$ |
| Internode 1-2 | $1.00^{a}$ | $2.00^{a}$ | $1.00^{a}$ | $1.00^{a}$ |
| Internode 2-3 | $4.00^{a}$ | $3.67^{ab}$ | $2.67^{ab}$ | $1.67^{b}$ |
| Internode 3-4 | $3.67^{a}$ | $0.33^{b}$ | $2.33^{bc}$ | $2.00^{c}$ |
| Internode 4-5 | $1.33^{a}$ | $0.67^{a}$ | $1.67^{a}$ | $1.33^{a}$ |

*Averaged across three replications.
†Superscripts indicate significant differences ($P \leq 0.1$) across rows.

Table 6.6: Mean absolute errors in internode lengths measured for different camera enclosure orientations and different internode positions for Data Set 1, with three replications.

| Internode position | Replicate | Mean absolute error in internode lengths (mm) | | | |
|---|---|---|---|---|---|
| | | Angle 0° | Angle 180° | Shear 135° | Shear 315° |
| Internode 0-1 | I | 4.00 | 11.90 | - | - |
| | II | - | 4.55 | - | - |
| | III | - | - | - | - |
| Internode 1-2 | I | 1.20 | 6.83 | 5.20 | 13.07 |
| | II | 13.40 | - | 11.20 | 3.00 |
| | III | 7.40 | 1.80 | - | - |
| Internode 2-3 | I | 7.13 | 8.95 | 7.20 | 10.70 |
| | II | 4.30 | 13.83 | 7.50 | 2.93 |
| | III | 6.20 | 4.50 | 2.60 | 2.00 |
| Internode 3-4 | I | 7.00 | - | 5.47 | 3.17 |
| | II | 8.74 | 11.40 | 2.95 | 4.37 |
| | III | 6.68 | - | 5.25 | 8.20 |
| Internode 4-5 | I | 2.37 | - | 9.70 | 4.55 |
| | II | 19.60 | 7.10 | 7.90 | 0.40 |
| | III | - | - | 13.40 | - |

Table 6.7: Analysis of variance for all the camera enclosure orientation ('Orientation') treatments of Internode 2-3 (Table 6.6).

| Source of variation | Sum of squares | Degrees of freedom | Mean square | Computed $f$ | Critical $f$ (5%) |
|---|---|---|---|---|---|
| Orientation | 27.95 | 3 | 9.32 | $0.69^{ns}$ | 4.07 |
| Error | 108.45 | 8 | 13.56 | | |
| Total | 136.40 | 11 | | | |

$^{ns}$ = not significant.

Table 6.8: Analysis of variance for the Angle 0°, Shear 135° and Shear 315° orientation ('Orientation') treatments of Internodes 2-3 and 3-4 (Table 6.6).

| Source of variation | Sum of squares | Degrees of freedom | Mean square | Computed $f$ | Critical $f$ (5%) |
|---|---|---|---|---|---|
| Internode position | 0.09 | 1 | 0.09 | $0.01^{ns}$ | 4.75 |
| Orientation | 8.77 | 2 | 4.39 | $0.62^{ns}$ | 3.89 |
| Interaction | 5.93 | 2 | 2.97 | $0.42^{ns}$ | 3.89 |
| Error | 85.05 | 12 | 7.09 | | |
| Total | 99.84 | 17 | | | |

$^{ns}$ = not significant.

### 6.4.2 Illumination – day versus night

Data Set 5 featured video collected in daylight with and without artificial lighting, and at night with visible and near infrared (850 and 940 nm) lighting. The number and position of internode lengths detected for different lighting conditions (Figure 6.3) are displayed in Table 6.9. An analysis of variation (Table 6.10) shows there was a significant difference in the number of internode lengths detected with respect to different lighting conditions, but there was no interaction between lighting conditions and camera enclosure orientation. Natural afternoon sunlight and 850 nm night time illumination yielded the most number of measurements (Table 6.11).

The number of internode lengths detected at 940 nm and with white LEDs, day or night, were not significantly different. The white LED illumination was not as effective at producing internode length results at night time as the 850 nm illumination. By inspection of analysed images, the white LED illumination did not produce uniform illumination of the plant in front of the camera enclosure, due to leaves casting shadows on branches. On the other hand, the 850 nm illumination was more effective at

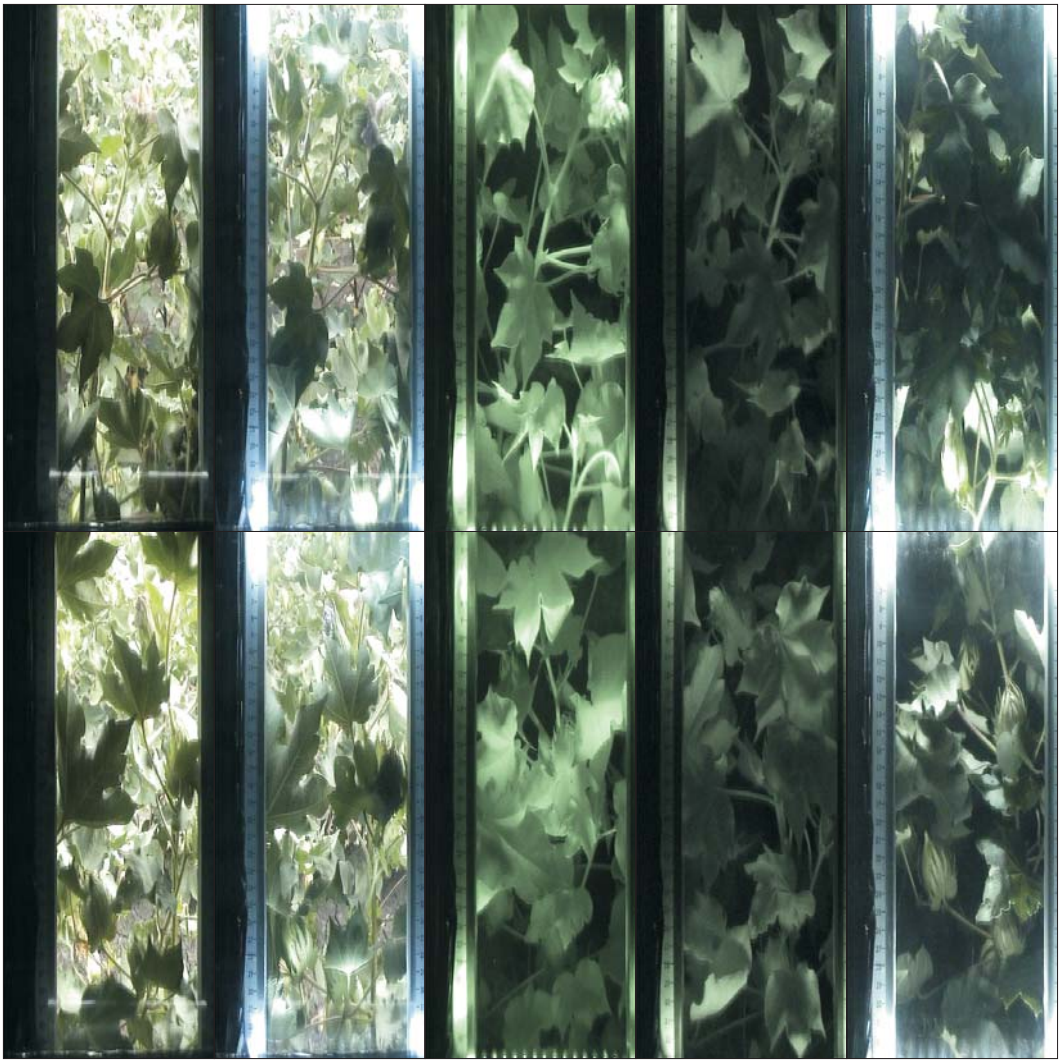

(a) (b) (c) (d) (e)

Figure 6.3: Images of a single plant from Data Set 5, showing different lighting sources: (a) afternoon sunlight; (b) white LEDs in daylight; (c) 850 nm LEDs at night; (d) 940 nm LEDs at night; and (e) white LEDs at night. *Top row*: Camera enclosure approach angle of 0°; *bottom row*: camera enclosure approach angle of 180°.

illuminating the plant in front of the transparent panel with high contrast from the background. The 940 nm imagery had lower contrast than the 850 nm imagery. This was most likely due to the lower CCD image sensor spectral sensitivity at the higher wavelength.

Table 6.9: Number of internode lengths detected for different lighting conditions and camera enclosure orientations ('Orientation') at day and night for Data Set 5, with three replications.

| Orientation | Replicate | Number of internode lengths | | | | |
|---|---|---|---|---|---|---|
| | | Afternoon sunlight | White LEDs in daylight | 850 nm LEDs at night | 940 nm LEDs at night | White LEDs at night |
| Angle 0° | I | 7 | 1 | 2 | 1 | 1 |
| | II | 2 | 1 | 5 | 2 | 3 |
| | III | 4 | 2 | 6 | 2 | 2 |
| Angle 180° | I | 1 | 1 | 5 | 1 | 2 |
| | II | 5 | 2 | 3 | 2 | 1 |
| | III | 2 | 3 | 9 | 4 | 0 |

Table 6.10: Analysis of variance for the detected internode position, camera enclosure orientation ('Orientation') and lighting treatments as set out in Table 6.9.

| Source of variation | Sum of squares | Degrees of freedom | Mean square | Computed $f$ | Critical $f$ (5%) |
|---|---|---|---|---|---|
| Orientation | 0.00 | 1 | 0.00 | $0.00^{ns}$ | 4.35 |
| Illumination | 53.53 | 4 | 13.38 | 4.41* | 2.86 |
| Interaction | 9.67 | 4 | 2.42 | $0.77^{ns}$ | 2.86 |
| Error | 60.67 | 20 | 3.03 | | |
| Total | 123.87 | 29 | | | |

* = significant at 5% level, $^{ns}$ = not significant.

### 6.4.3 Illumination – shadow and sun angle effects

The vision system was trialed on five cotton cultivars to determine whether the crop cultivar caused significant differences in measurement system performance. However, extra variables of time of day and crop row direction also affected this evaluation, since the cotton rows of Data Sets 1 and 5 were oriented east-west, and north-south for Data Sets 2 to 4 (Table 6.12). Therefore, the camera was either facing or turned away from the sun in Data Sets 2 to 4, while in Data Sets 1 and 5 the camera was always perpendicular to the sunlight direction. The average number of internode lengths detected for each data set are displayed in Table 6.13 and typical images in Figure 6.4. An analysis of variance is set out in Table 6.14.

Data Set 1 featured soft cloud cover and a camera direction perpendicular to the sun-

Table 6.11: Least significant differences for all possible pairs of illumination conditions.

| Illumination condition | Mean number of internode lengths*† |
|---|---|
| 850 nm LEDs at night | 5.00 |
| Afternoon sunlight | 3.50 |
| 940 nm LEDs at night | 2.00 |
| White LEDs in daylight | 1.67 |
| White LEDs at night | 1.50 |

*Averaged across two camera enclosure orientations and three replications.
†Any two means connected by the same vertical line are not significantly different at the 10% level of significance.

light and yielded the most number of internode measurements. However, Data Sets 2 and 3 were both collected around solar noon. These sets yielded the least number of internode measurements (Table 6.15) with the image background appearing overexposed compared to the foreground, regardless of the camera direction. Data Set 4 was captured in the morning. In this case, the sequences captured with the camera facing west (i.e. sun behind the camera) yielded more results than when the sun was in front of the camera (Table 6.16).

Table 6.12: Daytime data collection hours and camera direction for Data Sets 1 to 5.

| Data Set | Time of day | Camera direction (Angle 0°/Angle 180°) | Cultivar |
|---|---|---|---|
| 1 | 2.00–3.00pm | North/south | Sicot 80B |
| 2 | 12.00–1.00pm | East/west | Sicot 289B |
| 3 | 1.30–2.30pm | East/west | Sicot 71B |
| 4 | 8.30–9.30am | East/west | Deltapine 408B |
| 5 | 3.00–4.00pm | North/south | Sicot 60B |

(a) (b) (c) (d) (e)

Figure 6.4: Images from Data Sets 1 to 4, showing different sunlight conditions and varieties: (a) Data Set 1; (b) Data Set 2; (c) Data Set 3; (d) Data Set 4; and (e) Data Set 5. *Top row*: Camera enclosure approach angle of 0°; *bottom row*: camera enclosure approach angle of 180°.

Table 6.13: Average number of internode lengths detected for different sunlight conditions and camera enclosure orientations ('Orientation'), with three replications.

| Orientation | Replicate | Average number of internode lengths detected per plant | | | | |
|---|---|---|---|---|---|---|
| | | Data Set 1 | Data Set 2 | Data Set 3 | Data Set 4 | Data Set 5 |
| Angle 0° | I | 0.93 | 0.38 | 0.10 | 0.40 | 0.54 |
| | II | 0.86 | 0.13 | 0.00 | 0.10 | 0.15 |
| | III | 0.43 | 0.13 | 0.00 | 0.10 | 0.31 |
| Angle 180° | I | 0.50 | 0.13 | 0.40 | 0.40 | 0.08 |
| | II | 0.64 | 0.06 | 0.10 | 0.50 | 0.38 |
| | III | 0.50 | 0.06 | 0.10 | 0.60 | 0.15 |

Table 6.14: Analysis of variance for sunlight condition and camera enclosure orientation ('Orientation') treatments.

| Source of variation | Sum of squares | Degrees of freedom | Mean square | Computed $f$ | Critical $f$ (5%) |
|---|---|---|---|---|---|
| Orientation | 0.00 | 1 | 0.00 | $0.00^{ns}$ | 4.35 |
| Sunlight condition | 1.07 | 4 | 0.27 | 11.18* | 2.87 |
| Interaction | 0.28 | 4 | 0.07 | 2.97* | 2.87 |
| Error | 0.48 | 20 | 0.02 | | |
| Total | 1.83 | 29 | | | |

* = significant at 5% level, $^{ns}$ = not significant.

Table 6.15: Least significant differences for all possible pairs of sunlight conditions.

| Sunlight condition | Mean number of internode lengths*† |
|---|---|
| Data Set 1 | 0.64 |
| Data Set 4 | 0.35 |
| Data Set 5 | 0.27 |
| Data Set 2 | 0.15 |
| Data Set 3 | 0.12 |

*Averaged across two camera enclosure orientations and three replications.
†Any two means connected by the same vertical line are not significantly different at the 5% level of significance.

Table 6.16: Least significant differences for comparing pairs of camera enclosure orientation means for the same sunlight condition.

| Sunlight condition | Mean number of internode lengths*† | |
|---|---|---|
| | Angle 0° | Angle 180° |
| Data Set 1 | $0.74^a$ | $0.55^a$ |
| Data Set 2 | $0.21^a$ | $0.08^a$ |
| Data Set 3 | $0.03^a$ | $0.20^b$ |
| Data Set 4 | $0.20^a$ | $0.50^b$ |
| Data Set 5 | $0.33^a$ | $0.20^a$ |

*Averaged across three replications.
†Superscripts indicate significant differences ($P \leq 0.5$) across rows.

The cotton varieties tested were heliotropic (Section 2.1.1). This may have reduced the number of automatic internode length measurements for the north-south oriented rows as the sun was behind the camera and the leaves tended to be facing the camera rather than be randomly oriented and hence, caused more stem occlusions (stylised representation in Figure 6.5 and photograph in Figure 6.6). However, on the opposite side of the plant, detection rates were still not as high as for Data Set 1 (camera facing north/south) since the plant's background was overexposed from the sun being in front of the camera. Internode length detection was less successful in sunlight conditions in which stem regions were frequently washed out by bright or overexposed background canopy (e.g. Figure 6.4(b) to (d)). However, the variation in sunlight conditions prevented conclusions to be drawn about varietal differences in system performance. Under natural lighting conditions, the best results were obtained on partially cloudy days, such that the sunlight was diffused, with the camera facing north or south.

### 6.4.4 Depth of field (DOF)

A narrow DOF was hypothesised to yield more internode length results than an infinite DOF system by rendering the background foliage less salient than the in-focus foreground, thus reducing false positive candidate node detection. In Data Set 5, a narrow DOF was achieved by increasing the camera's aperture and compensating the increased amount of incoming light with a shorter exposure time (Chapter 3). The exposure time was chosen such that contrast was discernible within the darker foreground foliage, without the brighter background canopy washing out the darker parts of the image. This trade-off resulted in an image in which the foreground foliage still appeared dark (Figure 6.7(b)), but was overcome to an extent by adjusting the image contrast (Figure 6.7(c)). However, by visual inspection of Figure 6.7(c), the images still lacked the contrast between foreground and background that is apparent in Figure 6.7(a).

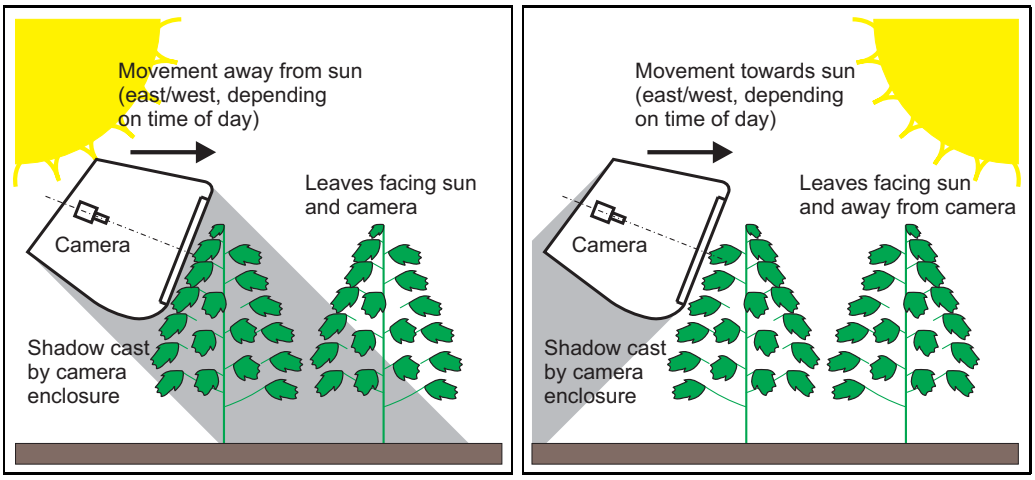


(a) (b)

Figure 6.5: Stylised representation of shadow and heliotropism effects of sun position when the camera faces: (a) away from the sun; and (b) towards the sun.

Figure 6.6: Photo of Data Set 2 canopy, showing leaves oriented towards the sun.

(a) (b) (c)

Figure 6.7: Images captured simultaneously of a single plant from Data Set 5, showing effect of a narrow depth of field: (a) image captured from Sony DV camcorder (CCD image sensor), with infinite depth of field; (b) image captured from Prosilica firewire camera (CMOS image sensor), with lensing for a narrow depth of field; and (c) contrast enhanced version of image (b).

The foreground of the narrow DOF image appears blurry because during lens setup, a focus distance was chosen to accentuate a difference in sharpness between the foreground and background (which is apparent in Figure 6.7(c)). It was observed that when the lens was adjusted such that the foreground plant was sharp and in focus, the background was not noticeably more blurred than the foreground. This suggests that the distance between the foreground and background in the present vision system is too small to obtain a noticeable DOF effect when the foreground is in focus.

Application of the image processing algorithms to the contrast enhanced narrow DOF images yielded internode length results that were significantly less reliable than the infinite DOF system (Table 6.17). This may be due to the reduced image contrast of the narrow DOF images.

Table 6.17: Number of internode lengths detected for different depth of field conditions and camera enclosure orientations ('Orientation') for Data Set 5 (daytime), with three replications.

| Orientation | Replicate | Number of internode lengths | |
|---|---|---|---|
| | | Infinite DOF | Narrow DOF |
| Angle 0° | I | 7 | 2 |
| | II | 2 | 1 |
| | III | 4 | 0 |
| Angle 180° | I | 1 | 0 |
| | II | 5 | 2 |
| | III | 2 | 0 |

### 6.4.5 Enclosure travel speed

The effect of speed with the camera enclosure travelling parallel to the row direction (Figure 6.1) was evaluated on Data Set 5 by calculating the mean absolute error and number of internode length measurements for different speeds (Table 6.18). The number of plants detected refers to the number of plants for which internode length measurements were automatically detected. The range of speeds evaluated correspond to expected speeds for various operation modes of the sensing system, i.e. on an LMIM or some other ground-based vehicle such as a tractor (Figure 1.4 in Section 1.3).

At the highest internode length detection rate (0.10 m/s travel speed), the machine vision system detected internode lengths for plants on an average 3.3 m apart (Table 6.18). This average distance between plants increased to 15 m at a camera enclosure speed of 0.25 m/s, and at 0.30 m/s the camera enclosure was moving too fast to detect any internode length measurements. An analysis of variance showed that the travel speed of 0.30 m/s obtained significantly inferior results ($P \leq 0.5$) to the other speeds. The image processing algorithm required a minimum of 10 frames to form a node trajectory

(at 25 frames per second, this is equivalent to 0.4 seconds). However, by observation of the image processing results for the images collected at 0.25 and 0.30 m/s, the nodes were rarely detected for more than 10 sequential frames.

Average plant spacing along a row is approximately 0.1 m so the maximum internode length detection rate is once per thirty-third plant, even at the slowest tested travel speed of the camera enclosure. However, the expected fastest speed of a LMIM tower is 2–3 m/min, or 0.03–0.05 m/s, which is less than half the slowest tested speed of the camera enclosure. Hence, decreasing the camera enclosure travel speed to match that of an irrigation machine (even for tractor-mounted operation) would be expected to increase the number of internode length measurements obtained by the automatic system.

Table 6.18: Internode length results for different camera enclosure speeds along row for 30 m for Data Set 5.

| Speed along row (m/s) | Replicate | Number of plants detected | Average distance between detected plants (m) | Number of internode lengths detected | Mean absolute error (mm) |
|---|---|---|---|---|---|
| 0.10 | I | 12 | 2.6 | 15 | 5.6 |
| | II | 11 | 2.8 | 12 | 6.1 |
| | III | 8 | 3.7 | 11 | 7.2 |
| 0.20 | I | 7 | 4.1 | 11 | 7.2 |
| | II | 8 | 3.4 | 13 | 8.9 |
| | III | 11 | 2.4 | 18 | 5.2 |
| 0.25 | I | 2 | 15.0 | 2 | 10.5 |
| | II | 2 | 15.0 | 2 | 9.4 |
| | III | 1 | - | 1 | 8.9 |
| 0.30 | I | 0 | - | 0 | - |
| | II | 0 | - | 0 | - |
| | III | 0 | - | 0 | - |

## 6.5 Evaluation of agronomic factors

### 6.5.1 Crop size and cultivar

Video footage of different cotton varieties was collected for the purpose of evaluating varietal differences in image processing results (Section 6.4.3). However, the sunlight

variation between data sets prevented direct cultivar-specific conclusions from being drawn. Other manual comparisons of the data sets enabled identification of varietal differences which may influence image processing results under controlled lighting conditions (Table 6.19).

Table 6.19: Differences identified between plants of evaluated cotton varieties.

| Data Set | Cultivar | Average plant height (mm) | Ground cover | Stem colour | Reported growth habit* |
|---|---|---|---|---|---|
| 1 | Sicot 80B | 907 | 90% | Green/red | Vigorous |
| 2 | Sicot 289B | 753 | 80% | Green | Vigorous |
| 3 | Sicot 71B | 589 | 50% | Green | Compact |
| 4 | Deltapine 408B | 739 | 70% | Green/red | Compact |
| 5 | Sicot 60B | 592 | 65% | Green/red | Compact |

*From cotton variety guides published by CSD (2007) and Deltapine (2007).

Stem colour was a function of crop age and/or crop size, since young stems were green, turning red with exposure to the sun. Compact varieties have a more determinate growth habit and more bolls, while vigorous varieties have a more indeterminate or rank (excessive vegetative) growth habit.

## 6.6 Conclusions and potential improvements

The evaluations presented in this chapter have led to the following conclusions:

- automatically measured values for internode length were not significantly different from the values manually measured on the plants and did not exhibit measurement bias despite the maximum distance between detected node trajectories being used as the best estimate for internode distance;
- Internodes 2-3 and 3-4 were most commonly detected by the automatic system;
- night time infrared images provided as many internode length measurements as the corresponding daytime measurements (in favourable sunlight conditions);
- sunlight perpendicular to the camera yielded significantly more measurements than sunlight in front or behind the camera; and

- camera enclosure speeds up to 0.20 m/s along the crop row yielded internode length measurements with the current image processing algorithms and hardware. However, slowing the travel speed significantly increased the number of internode measurements obtained.

The most significant factors limiting the number of internode measurements obtained were found to be the sunlight angle and intensity. Hence, ideally the camera enclosure should be modified to effectively block out the sunlight and enable internode length measurement under artificial illumination regardless of the ambient sunlight. The camera should be oriented to avoid facing heliotropic leaves to reduce occlusion of stems.

# Chapter 7

# Real-time implementation

## 7.1 Rationale

The vision system has been shown to measure internode length successfully in the field (Chapter 6). However, the vision system is intended (Section 2.3) to sense the plant condition for real-time irrigation control, i.e. whilst mounted on a large mobile irrigation machine (LMIM), from which some control action could be decided upon and transmitted to the relevant nozzles of the irrigation machine. Hence, acceptable real-time performance is required to meet this objective.

Other potential applications of the measurement capacity developed include identification of crop deficiencies and disease, ground truthing of other remotely sensed data and to assist the autonomous placement of other plant sensors. In each case, the requirements for on-the-go operation of the vision system encompass automatic conveyance of the camera enclosure, real-time software execution and integration with post-processing or management actions. This chapter provides a theoretical evaluation of the potential for real-time implementation of the vision system under potential operating conditions.

## 7.2 Automated conveyance of camera enclosure

Autonomous mechanical operation of the vision system has been demonstrated using the infield apparatus for automated conveyance of the camera enclosure across the plant rows (Chapter 3). Across row movement of the camera enclosure was evaluated for this research because plant spacing across rows was considerably less dense than along the row. A single camera enclosure travelling at 0.30 m/s across the rows (e.g. when mounted on the LMIM gantry) would travel 36 m in 2 minutes (a typical time-frame for an LMIM movement of 1 m). Hence, the camera enclosure would not be expected to travel an entire LMIM span and maintain a measurement spatial resolution of 1 $m^2$. The camera enclosure speed evaluation (Section 6.4.5) established that along row measurement was also possible.

## 7.3 Real-time software execution

The final image processing algorithm (Chapters 4 and 5) had an unoptimised execution time of approximately 400 ms per frame on an Intel Celeron 1.40 GHz processor, using the high level programming language Borland Delphi 6.0 on a Windows XP operating system. However, the software had a significant graphical user interface (GUI) component. Removal of the GUI and optimised executable code would be expected to reduce the code execution time per frame, such that frame processing rate would approach the capture rate of 25 frames per second (fps). Further speed improvements may be achieved by using an operating system optimised for real-time applications and by parallel processing.

Conventional embedded systems based on microprocessors are limited because the CPU structure means that instructions are executed sequentially (Nelson, 2000). Giusto et al. (2001) indicates methods of estimating real-time software execution for CPU-based embedded systems. Vision systems can be accelerated using field programmable gate arrays (FPGAs)(Figure 7.1) which consist of programmable logic that runs in parallel.

FPGA implementations of image processing algorithms exploit parallelisms and achieve speed improvements of 8 to 800 times over CPU systems (Draper et al., 2003).

An itemised list of the image processing steps for candidate node detection is displayed in Table 7.1, with labels a–c (as applicable) indicating processes that can occur concurrently under each step. The FPGA execution speeds were estimated by summing together the execution times for constituent operations of each of the image processing steps and using time estimates from the sources listed. Hence, an approximate total execution time for the algorithm, given by summing the maximum execution time for each step in Table 7.1, is 46 ms which corresponds to a frame rate of 21 fps.

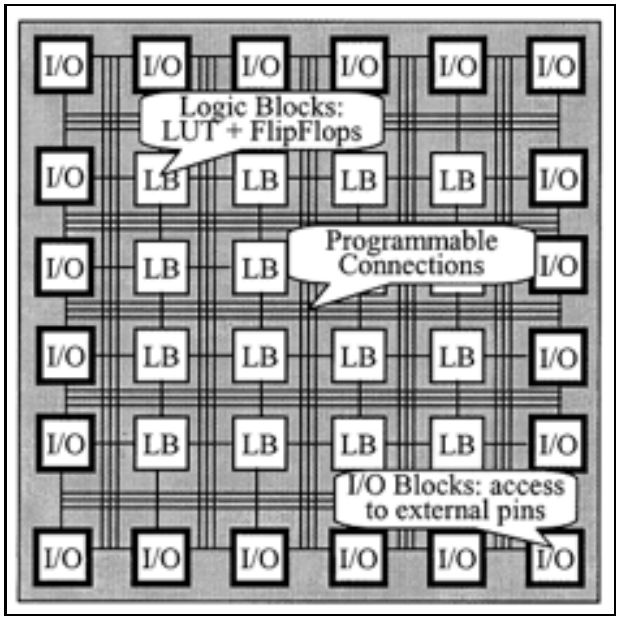


Figure 7.1: Conceptual diagram of an FPGA. The LUT (lookup table) contents and grid lines are reprogrammable. The IO pins are connected to external sources such as memory chips or image buffers. Source: Draper et al. (2003).

Table 7.1: Image processing steps for individual frames (Section 4.12).

| Image processing step* | Description of required operations | Estimated FPGA execution time per frame (ms)** and reference |
|---|---|---|
| **1. For each pixel, calculate partial second-order derivatives:** | | |
| a. Gaussian kernel $G_{x'y'}$ | $5 \times 5$ kernel convolution | 20 (Draper et al., 2000) |
| b. Gaussian kernel $G_{x''}$ | As for Step 1.a. | As for Step 1.a. |
| c. Gaussian kernel $G_{y''}$ | As for Step 1.a. | As for Step 1.a. |
| **2. For each pixel, calculate vesselness and location of centre point:** | | |
| a. Calculate vesselness | Fixed mathematical operations | 3 (Draper et al., 2000) |
| b. Calculate centre points | As for Step 2.a. | As for Step 2.a. |
| **3. For each pixel, identify branch segments:** | | |
| a. Connected components and shape properties | Bounding box, area | 10 (Amir et al., 2005) |
| **4. For centre points in each shape (branch segment), fit lines:** | | |
| a. Fit lines | Fixed mathematical operations and conditional branching | 3 (Draper et al., 2000) |
| b. Calculate Hough transform parameters | Fixed mathematical operations | 10 (Tagzout et al., 2001) |
| **5. For each line, estimate a candidate node position:** | | |
| a. Calculate node positions | Fixed mathematical operations and conditional branching | 3 (Draper et al., 2000) |

* Labels a–c indicate sub-components which can occur concurrently under each step.
** Based on 30 MHz clock.

## 7.4 Interfacing with post processing and control actions

### 7.4.1 Variable-rate irrigation control

The vision sensor may be used with a variable-rate centre pivot or lateral move irrigation machine to vary water output in response to sensed plant irrigation requirements. Such a variable-rate system would potentially require data from a variety of other environmental sensors (e.g. soil moisture sensors, remote sensing images and meteorological conditions) and would need a decision support system to integrate the data and determine the irrigation amount as described in Section 1.5 (also Smith et al. (2007) and McCarthy et al. (2008)).

Using the IEEE 802.15.4 wireless standard (with a transmission rate of 250 kb/s) and

transmitting a 50-byte data packet consisting of internode distance and GPS data, the vision sensor system would be able to log internode length data to a central database. This data would be used by the decision support system to calculate the irrigation amount and issue a command for a particular irrigation amount to be applied at the appropriate GPS location. Table 7.2 sets out the estimated execution times for these operations. This analysis suggests that the camera enclosure must be physically mounted such that the acquired images are at least six seconds ahead of the variable-rate irrigation application.

Table 7.2: Estimated post processing execution time for steps required to generate variable-rate irrigation command.

| Step | Process | Estimated execution time (ms) |
|---|---|---|
| 1 | Time for one pass of camera enclosure over plant (across row) | 3000 |
| 2 | Wireless transmission of each data packet (internode distance and GPS data) from imaging system | 2 |
| 3 | Decision support system accesses database and calculates irrigation amount | 1000 |
| 4 | Wireless transmission of command for irrigation amount to irrigation machine | 2<br>2 |
| 5 | Variable-rate nozzle response time | 2000 |
| | **Total estimated time for control sequence** | 6004 ms |

### 7.4.2 Other potential post processing and control applications

The vision system is capable of infield identification of sub-plant features and the potential identification of topological positions of plant structures. This has possible uses beyond irrigation control including (Chapter 8):

- Use as part of a sensor for nutrient deficiencies for the purpose of variable-rate nutrient application. If the system identifies leaves at specific locations on a plant, the addition of a second imaging device (Camera 2 of Figure 7.2) with differing spectral characteristics will permit identification of symptomatic discolouration of individual leaves associated with nutrient deficiencies. In this case, test discolouration patterns could be stored on-board such that external database access is not required.

- Automatic guidance for sensors (e.g. infrared thermometers) which require precise placement to target individual leaves. Placement of the sensor to the required mechanical position may take of order one or two seconds which would permit its use for real-time sensing and control application.

- Correlation between ground-based plant growth measurements (taken with the automated vision system) and management zones identified in remote sensing images to enable a physiological interpretation and/or ground truthing of the remotely sensed images.

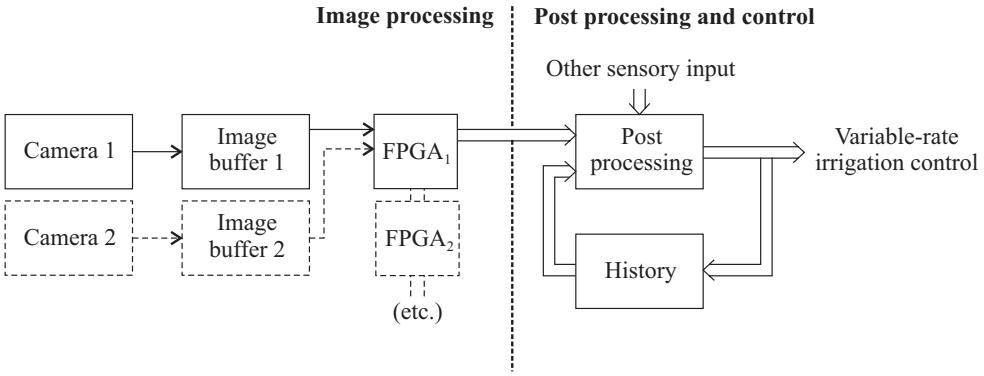


Figure 7.2: Conceptual block diagram of real-time imaging system (left hand side) and associated variable-rate irrigation control (right hand side). (Camera 2, Image buffer 2, etc. indicate potential system expansion, if required.)

## 7.5 Conclusions

The estimated frame rate for algorithm execution on a FPGA implementation was 21 fps. Although this does not meet the standard video frame rate of 25 fps, reducing the video frame rate and travel speed of the camera enclosure (as suggested in Section 6.4.5) would provide a margin for computational requirements. Hence, it is concluded that integration of the sensing system with a real-time irrigation controller is achievable.

# Chapter 8

# Conclusions and further work

A vision sensing system has been designed and evaluated for on-the-go measurement of cotton plant internode length. The data from this sensor can be used to indicate crop water stress and is suitable for potential integration with an automatic variable-rate irrigation controller on a LMIM.

In this chapter, Sections 8.1 to 8.3 describe the conclusions from this research with respect to the objectives set out in Section 2.3. Section 8.4 contains recommendations for further development of the research.

## 8.1 Plant-based vision sensing of cotton

*Objective 1. Develop a robust monitoring platform for non-destructive machine vision sensing of individual cotton plants under commercial conditions.*

*AND*

*Objective 2. Develop an image processing algorithm for the identification of internode length and other plant geometric properties.*

Field measurement of internode length was achieved (Chapter 5) using a moving, plant-

contacting camera enclosure (Chapter 3). The enclosure was effective at manipulating foliage such that the main stem and branches became visible as the enclosure moved over the plant. The maximum distance between node trajectories was found to correlate strongly with conventional manual measurements of internode length (Chapter 6). The presence of occlusions and other foliage edges between successive main stem nodes prevented reliable internode length measurement in individual frames (Chapter 4), but was overcome by analysing candidate node positions in a sequence of images (Chapter 5).

## 8.2 Practical implementation of infield vision sensing of individual plants

*Objective 3. Evaluate the performance of the machine vision system under a range of crop and environmental conditions expected in commercial application.*

Internodes 2-3 and 3-4 were most frequently detected by the vision system (Chapter 6). These internode lengths are useful from a plant physiology viewpoint, since younger internodes are still growing and responding to plant stresses, whereas Internodes 4-5 and older have ceased growing and are a purely historical indication of plant stress.

The number of internode lengths measured by the automatic image processing algorithms was influenced by the ambient lighting conditions (Chapter 6). Favourable sunlight conditions (diffused sunlight perpendicular to the camera) resulted in an average of one internode length per plant being automatically detected. Night time infrared imagery performed as well as the preferred daylight conditions (Section 6.4.2).

Automated conveyance of the camera enclosure across the plant rows was achieved using a quad-axis motorised drive system (Chapter 3). Along row sensing was less reliable at automatic internode length detection than measurements across the rows (Section 6.4.5) but this is expected to be improved by reducing the camera enclosure speed to reflect the maximum LMIM speed (2–3 m/min).

## 8.3 Application to irrigation management

*Objective 4. Assess the potential to use the machine vision system for real-time control of irrigation application.*

The system detected one internode length per 1.75 plants for across row measurements (at an enclosure speed of 0.30 m/s), and one internode length per 3.3 m for along row measurements (at an enclosure speed of 0.10 m/s) (Section 6.4.5). However, the detection rate on any particular plant varied from zero to three internode lengths using the current algorithm. Average plant spacing along the row is 10 plants/m so to achieve a measurement spatial resolution of 1 $m^2$ for across row measurements the vision system operation could be modified to measure more plants in each row. This could be achieved by multiple passes of the camera enclosure or by increasing the width of the camera enclosure and transparent panel to measure more than one plant per crop row per sequence.

The vision system's ability to measure the rate of plant growth and the onset of water stress was not evaluated because variations in daylight conditions prevented individual plants from being measured on multiple days. However, with additional imaging devices and image processing algorithms, other plant-based water stress/growth indicators such as nodes above white flower are potentially measurable using the camera enclosure (Section 8.4.1). The automatic internode length algorithm was also shown to be able to be run in real-time at 21 frames per second making it suitable for on-the-go measurement in conjunction with an irrigation machine.

## 8.4 Recommended further work

### 8.4.1 Potential approach for measurement of nodes above white flower

The number of nodes above white flower (NAWF) is a significant parameter for assessing cotton plant growth. It typically ranges from eight or nine at the start of the cotton

flowering season, to five or six nodes at cutout (Oosterhuis, 1990). To assess the NAWF, an additional camera would need to be installed into the camera enclosure to view those (lower) nodes that are above the white flower but that are currently not able to be viewed by the primary camera, i.e. nodes 7–10 in the sample image sequences Chapter 4. The additional camera would not be required to measure precise geometry, but rather node positions, since the unit of measurement for nodes above white flower is number of nodes.

Machine vision detection of a cotton plant's flowers requires colour or shape detection or both. Due to the variable position and orientation of both flowers and leaves, shape is not necessarily a reliable property to distinguish the two structures. Similarly, standard RGB image sensor channels are not guaranteed to differentiate flowers from leaves since both plant materials may appear overexposed in all channels in direct sunlight. However, preliminary field investigations found that a red filter was effective at differentiating yellow flowers from both sunlit and shaded green leaves from plant top views (Figure 8.1), since green leaves have a high green and low red reflectance while yellow or white flowers have a high green and high red reflectance. Hence, a simple threshold on a red-filtered image is expected to yield candidate white flowers for individual frames. This suggests that an additional (low resolution) camera would also be required to specifically obtain red images for flower detection, since the node detection algorithm uses the green channel of the image.

The image processing algorithm for flower detection would be expected to be similar to the node detection algorithm, where candidate flowers are detected in individual frames and then accepted or rejected at the sequential image analysis stage. Since only first position flowers are required to be detected, only the image area surrounding the main stem need be searched for white flowers. Node 'ownership' of flowers could be obtained by comparing candidate flower trajectories with candidate node trajectories.

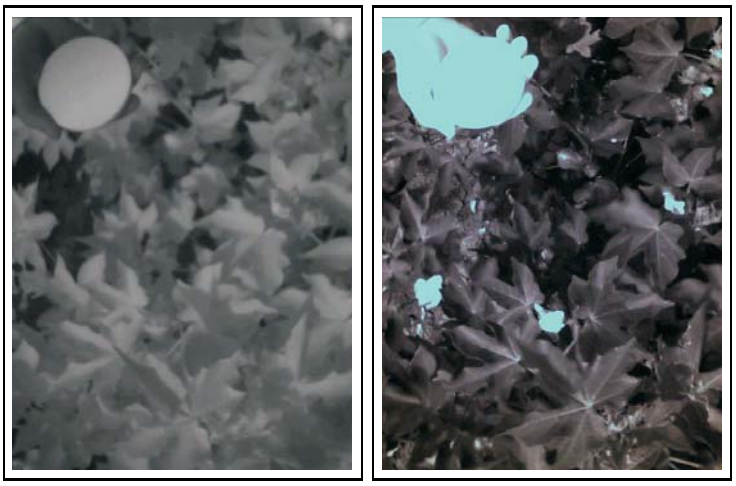

(a) (b)

Figure 8.1: Top view of a cotton plant with yellow flowers, captured simultaneously with narrow band filters of: (a) 940 nm; and (b) 670 nm. The circular panel at the top left is a white reference and the bright regions of image (b) correspond to white flowers on the cotton plant.

### 8.4.2 System enhancement

The following recommendation is considered high priority for regular research use of the vision system in its present configuration.

- Design a hood and lighting scheme for daytime operation of the camera enclosure to improve performance of the image processing algorithms under a range of sunlight conditions.

Potential research and development areas to increase the node detection rate of the vision system are below.

- Increase the width of the camera enclosure to enable measurement of more than one plant per row for across row measurements. For example, increase the width of camera enclosure Mark 4 (Table 3.1 in Section 3.2), but maintain the enclosure's vertical section geometry (Figure 3.4(d)) and use a wider angle camera lens for video acquisition. Modification of the image processing algorithm is expected to be necessary to detect and track multiple plants in a single video sequence.

- Incorporate algorithms for adaptive height control of the camera enclosure so that plants of different size or age may be automatically measured in the field. For the present research the height of the camera enclosure was manually adjusted for different plant sizes (Section 3.7 and 3.8). However, the automated infield chassis had motorised height control (Section 3.8).

- Investigate potential algorithm developments such as modeling of plant structure to reduce node detection computation for each frame and colour clustering methods such as that described in Neto, Meyer & Jones (2006) to segment vegetation pixels corresponding to different plant materials (Meyer, 2008).

- Investigate techniques by which node positions from the top of the plant are automatically counted or identified. This may potentially be achieved by improving node detection rates so the top five nodes are reliably detected or by relating internode position to some other plant physiological factor such as the size of the node's subtending leaf.

Other research opportunities to extend the vision system's field use include the following.

- Evaluate any modifications/enhancements to the vision system in different cotton cultivars and operating conditions, including day, night and dawn/dusk.

- Investigate the vision system's applicability to other field crops.

- Investigate the extent to which the contact between the camera enclosure and the plant affects plant growth characteristics.

- Examine methods for automatic cleaning of the apparatus, in particular the window at the front of the camera enclosure, to enable extended periods of field use.

### 8.4.3 Post-processing considerations

Potential applications for the vision system in precision agriculture are listed below.

- Compare automatic internode length measurements with aerial or satellite imagery (for example) to investigate spatial variability of plant water stress for irrigation management.
- Integrate the vision system with a LMIM and real-time controller to demonstrate application for irrigation control under field conditions.

# References


Adamchuk, V., Hummel, J., Morgan, M. & Upadhyaya, S. (2004), 'On-the-go soil sensors for precision agriculture', *Computers and Electronics in Agriculture* **44**(1), 71–91.

Adamsen, F., Coffelt, T., Nelson, J., Barnes, E. & Rice, R. (2000), 'Method for using images from a color digital camera to estimate flower number', *Crop Science* **40**, 704–709.

Amir, A., Zimet, L., Sangiovanni-Vincentelli, A. & Kao, S. (2005), 'An embedded system for an eye-detection sensor', *Computer Vision and Image Understanding* **98**, 104–123.

Andersen, H., Reng, L. & Kirk, K. (2005), 'Geometric plant properties by relaxed stereo vision using simulated annealing', *Computers and Electronics in Agriculture* **49**, 219–232.

Australian Bureau of Statistics (2006), *Water Account, Australia 2004-2005*, ABS Catalogue No. 4610.0, Commonwealth of Australia.

Australian Bureau of Statistics (2008), *Water Use on Australian Farms 2005-2006*, ABS Catalogue No. 4618.0, Commonwealth of Australia.

Bacci, L., Vincenzi, M. D., Rapi, B., Arca, B. & Benincasa, F. (1998), 'Two methods for the analysis of colorimetric components applied to plant stress monitoring', *Computers and Electronics in Agriculture* **19**, 167–186.

Bakic, V. (1996), *The MR-RIPL 2.0 user's guide*. Viewed 26 October 2006, `http://rootimag.css.msu.edu/MR-RIPL/MR-RIPL-2.0_guide_HTML`.

Bjurstrom, H. & Svensson, J. (2002), Assessment of grapevine vigour using image processing, Electrical engineering, Linkoping University. Master's thesis.

Bourland, F., Oosterhuis, D., Tugwell, N., Cochran, M. & Danforth, D. (1997), Interpretation of cotton growth curves generated by COTMAN, Special report 181, University of Arkansas Agricultural Experiment Station, Fayetteville, Arkansas.

Bowman, W. (1989), 'The relationship between leaf water status, gas exchange, and spectral reflectance in cotton leaves', *Remote Sensing of the Environment* **30**(392), 249–255.

Bramley, R. & Hamilton, R. (2004), 'Understanding variability in winegrape production systems: 1. Within vineyard variation in yield over several vintages', *Australian Journal of Grape and Wine Research* **10**, 32–45.

Breda, N. (2003), 'Ground-based measurements of leaf area index: a review of methods, instruments and current controversies', *Journal of Experimental Botany* **54**(392), 2403–2417.

Cantrell, R. (2005), 'The world of cotton', *Pflanzenschutz-Nachrichten Bayer* **58**(1), 77–92.

Carter, G. & Miller, R. (1994), 'Early detection of plant stress by digital imaging within narrow stress-sensitive wavebands', *Remote sensing and environment* **50**, 295–302.

Casady, W., Singh, N. & Costello, T. (1996), 'Machine vision for measurement of rice canopy dimensions', *Transactions of the ASAE* **39**(5), 1891–1898.

Chaerle, L., Hulsen, K., Hermans, C., Strasser, R., Valcke, R., Hfte, M. & van der Straeten, D. (2003), 'Robotized time-lapse imaging to assess in-planta uptake of

phenylurea herbicides and their microbial degradation', *Physiologia Plantarum* **118**(4), 613–619.

Chanwimaluang, T. & Fan, G. (2003), An efficient blood vessel detection algorithm for retinal images using local entropy thresholding, *in* 'Proceedings of the 2003 IEEE International Symposium on Circuits and Systems, Bangkok'.

Chi, Y., Chien, C. & Lin, T. (2002), 'Leaf shape modeling and analysis using geometric descriptors derived from Bezier curves', *Transactions of the ASAE* **45**(6), 175–185.

Chien, C. & Lin, T. (2002), 'Leaf area measurement of selected vegetable seedlings using elliptical Hough transform', *Transactions of the ASAE* **45**(5), 1669–1677.

Chien, C. & Lin, T. (2005), 'Non-destructive growth measurement of selected vegetable seedlings using orthogonal images', *Transactions of the ASAE* **48**(5), 1953–1961.

Chien, C., Wang, C., Yeh, C. & Lin, T. (2004), Plant seedling measurement and graphical reconstruction using multiple orthogonal-view images, *in* 'Proceedings of the 2nd International Symposium on Machinery and Mechatronics for Agriculture and Biosystems Engineering'.

Colaizzi, P., Barnes, E., Clarke, T., Choi, C., Waller, P., Haberland, J. & Kostrzewski, M. (2003), 'Water stress detection under high frequency sprinkler irrigation with water deficit index', *Journal of Irrigation and Drainage Engineering* **129**(1), 36–43.

Computronics Corporation Ltd. (2002), *Farmscan*, Bentley, Western Australia. Viewed 3 March 2005, `http://www.farmscan.net`.

Corke, P. (2008). Science Leader, Sensor Network Systems, CSIRO, *pers. comm.* 11 October.

CSD (2007), *Cotton Seed Distributors Variety Guide*. Viewed 10 March 2008, `http://www.csd.net.au`.

Das, V. (2004), *Photosynthesis*, Science Publishers, Inc, Enfield, New Hampshire.

Deltapine (2007), *Deltapine Australia Products*. Viewed 10 March 2008, `http://www.deltapine.com.au`.

Deriche, R. & Faugeras, O. (1990), 'Tracking line segments', *Lecture Notes in Computer Science* **427**, 259–268.

Draper, B., Beveridge, J., Bohm, A., Ross, C. & Chawathe, M. (2003), 'Accelerated image processing on FPGAs', *IEEE Transactions on Image Processing* **12**(12), 1543–1551.

Draper, B., Najjar, W., Bohm, W., Hammes, J., Rinker, B., Ross, C., Chawathe, M. & Bins, J. (2000), Compiling and optimizing image processing algorithms for FPGAs, *in* 'Fifth IEEE International Workshop on Computer Architectures for Machine Perception', pp. 222–231.

Du, J., Wang, X. & Zhang, G. (2007), 'Leaf shape based plant species recognition', *Applied Mathematics and Computation* **185**, 883–893.

Duda, R. & Hart, P. (1972), 'Use of the Hough transformation to detect lines and curves in pictures', *Communications of the ACM* **15**(1), 11–15.

Dunn, M., Billingsley, J. & Bell, D. (2006), 'Vision based macadamia yield assessment', *Sensor Review* **26**, 312–317.

Edan, Y., Rogozin, D., Flash, T. & Miles, G. (2000), 'Robotic melon harvesting', *IEEE Transactions on Robotics and Automation* **16**(6), 831–834.

Ehleringer, J. & Hammond, S. (1987), 'Solar tracking and photosynthesis in cotton leaves', *Agricultural and Forest Meteorology* **39**, 25–35.

Ehret, D., Lau, A., Bittman, S., Lin, W. & Shelford, T. (2001), 'Automated monitoring of greenhouse crops', *Agronomie* **21**(1), 403–414.

Evans, R., Benham, B. & Trooien, T., eds (1997a), *National Irrigation Symposium: Proceedings of the 4th Decennial Symposium*, American Society of Agricultural Engineers, Phoenix, Arizona.

Evans, R., Buchleiter, G., Sadler, E., King, B. & Harting, G. (1997b), Controls for precision irrigation with self-propelled systems, *in* Evans et al. (1997a), pp. 322–331.

Ewing, R. & Horton, R. (1999), 'Quantitative color image analysis of agronomic images', *Agronomy Journal* **91**, 148–153.

Fleisher, D., Rodriguez, L., Both, A., Cavazzoni, J. & Ting, K. (2006), Advanced life support systems in space, *in* 'CIGR Handbook of Agricultural Engineering Volume VI Information Technology', pp. 339–354.

Foley, J. & Raine, S. (2001), Centre pivot and lateral move machines in the Australian cotton industry, Publication 1000176/1, National Centre for Engineering in Agriculture, USQ, Toowoomba.

Foley, J. & Raine, S. (2002), 'Overhead irrigation in the Australian cotton industry', *The Australian Cottongrower* **23**(1), 40–44.

Frangi, A., Niessen, W., Vincken, K. & Viergever, M. (1998), 'Multiscale vessel enhancement filtering', *Lecture Notes in Computer Science* **1496**, 130–137.

Gausman, H., Allen, W., Escobar, D., Rodriguez, R. & Cardenas, R. (1971), 'Age effects of cotton leaves on light reflectance, transmittance, and absorptance and on water content and thickness', *Agronomy Journal* **63**, 465–469.

Geiger, D. (2004), Extending the utility of machine based height sensors to spatially monitor cotton growth, Biological and agricultural engineering, Texas A & M University. Master's thesis.

Gibson, P. & Power, C. (2000), *Introductory Remote Sensing: Digital Image Processing and Applications*, Routledge, London.

Giusto, P., Martin, G. & Harcourt, E. (2001), Reliable estimation of execution time of embedded software, *in* 'Proceedings of the Conference on Design, Automation and Test in Europe', IEEE Press, pp. 580–589.

Goldhamer, D. & Fereres, E. (2004), 'Irrigation scheduling of almond trees with trunk diameter sensors', *Irrigation Science* **23**(1), 11–19.

Gomez, K. & Gomez, A. (1984), *Statistical Procedures for Agricultural Research*, John Wiley & Sons.

Hearn, A. (1994), The principles of cotton water relations and their application in management, *in* G. Constable & N. Forrester, eds, 'Challenging the Future: Proceedings of the world cotton research conference', CSIRO, Australia, p. 66.

Hemming, J., Golbach, F. & Noordam, J. (2005), Reverse volumetric intersection (RVI), a method to generate 3D images of plants using multiple views, *in* 'Computer-Bildanalyse in der Landwirtschaft'.

Hemming, J. & Rath, T. (2002), 'Image processing for plant determination using the Hough transform and clustering methods', *Gartenbauwissenschaft* **67**(1), 1–10.

Hemming, J., van Henten, E., van Tuijl, B. & Bontsema, J. (2005), A leaf detection method using image sequences and leaf movement, *in* van Straten et al. (2005), pp. 765–772.

Hladuvka, J. & Groller, E. (2002), 'Exploiting the Hessian matrix for content-based retrieval of volume-data features', *The Visual Computer* **18**, 207–217.

Hobbs & Holder LLC (2005), *Hobbs & Holder*, Ashburn, Georgia. Viewed 13 March 2005, `http://www.betterpivots.com`.

Huck, M. & Klepper, B. (1977), 'Water relation of cotton. II. Continuous estimates of plant water potential from stem diameter measurements', *Agronomy Journal* **69**, 593–597.

Humphries, S. & Simonton, W. (1993), 'Identification of plant parts using color and geometric image data', *Transactions of the ASAE* **36**(5), 1493–1500.

Hyyppa, J., Kelle, O., Lehikoinen, M. & Inkinen (2001), 'A segmentation-based method to retrieve stem volume estimates from 3-d tree height models produced by laser scanners', *IEEE Transactions on Geoscience and Remote Sensing* **39**(5), 969–975.

Ishida, M. (2004), 'Automatic thresholding for digital hemispherical photography', *Canadian Journal of Forest Research* **34**(11), 2208–2216.

Ivanov, N., Boissard, P., Chapron, M. & Andrieu, B. (1995), 'Computer stereo plotting for 3-D reconstruction of a maize canopy', *Agricultural and Forest Meteorology* **75**, 85–102.

Jackson, R. & Ezra, C. (1985), 'Spectral response of cotton to suddenly induced water stress', *International Journal of Remote Sensing* **6**(1), 177–185.

Jain, R., Kasturi, R. & Schunck, B. (1995), *Machine Vision*, McGraw-Hill, Inc, Sydney.

Jimenez, A., Ceres, R. & Pons, J. (2000), 'A survey of computer vision methods for locating fruit on trees', *Transactions of the ASAE* **43**(6), 1911–1920.

Johnson Hake, S., Kerby, T. & Hake, K. (1996), *Cotton production manual*, Division of Agriculture and Natural Resources. ANR Publication 3352.

Jonckheere, I., Fleck, S., Nackaerts, K., Muys, B., Coppin, P., Weiss, M. & Baret, F. (2004), 'Review of methods for in situ leaf area index determination Part I. theories, sensors and hemispherical photography', *Agricultural and Forest Meteorology* **121**(1–2), 19–35.

Jones, H. (2004), 'Irrigation scheduling: advantages and pitfalls of plant-based methods', *Journal of Experimental Botany* **55**(407), 2427–2436.

Jones, H., Stoll, M., Santos, T., de Sousa, C., Chaves, M. & Grant, O. (2002), 'Use of infrared thermography for monitoring stomatal closure in the field: application to grapevine', *Journal of Experimental Botany* **53**(378), 2249–2260.

Kacira, M. & Ling, P. (2001), 'Design and development of an automated and non-contact sensing system for continuous monitoring of plant health and growth', *Transactions of the ASAE* **44**(4), 989–996.

Kacira, M., Ling, P. & Short, T. (2002), 'Machine vision extracted plant movement for early detection of plant water stress', *Transactions of the ASAE* **45**(4), 1147–1153.

Kalman, R. (1960), 'A new approach to linear filtering and prediction problems', *Transactions of the ASME - Journal of Basic Engineering* **82**, 35–45.

Kaminuma, E., Heida, N., Tsumoto, Y., Yamamoto, N., Goto, N., Okamoto, N., Konagaya, A., Matsui, M. & Toyoda, T. (2004), 'Automatic quantification of morphological traits via three-dimensional measurement of *Arabidopsis*', *The Plant Journal* **38**, 358–365.

Kass, M., Witkin, A. & Terzopoulos, D. (1987), 'Snakes: active contour models', *International Journal of Computer Vision* **1**(4), 321–331.

Kawollek, M. & Rath, T. (2005), Machine vision for three-dimensional modelling of *Gerbera jamesonii* for automated robotic harvesting, *in* van Straten et al. (2005).

Khan, U. (2003), 'Monitoring the growth and development of cotton plants using main stem node counts', *Asian Journal of Plant Sciences* **2**(8), 593–596.

Kim, Y. & Ling, P. (2001), 'Machine vision guided sensor positioning system for leaf temperature assessment', *Transactions of the ASAE* **44**(6), 1941–1947.

King, B. & Wall, R. (1998), 'Supervisory control and data acquisition system for site-specific center pivot operation', *Applied Engineering in Agriculture* **14**(2), 135–144.

Kise, M. & Zhang, Q. (2006), Reconstruction of a virtual 3D field scene from ground-based multi-spectral stereo imagery, ASAE Meeting Paper No. 063098, ASAE, Sacramento, California, ASAE.

Klepper, B., Browning, V. & Taylor, H. (1971), 'Stem diameter in relation to plant water status', *Plant Physiology* **48**, 683–685.

Kondo, N. & Ting, K. (1998), 'Robotics for plant production', *Artificial Intelligence Review* **12**(1–3), 227–243.

Kramer, P. & Boyer, J. (1995), *Water Relations of Plants and Soils*, Academic Press, San Diego.

Kurata, K. & Yan, J. (1996), 'Water stress estimation of tomato canopy based on machine vision', *Acta Horticulturae* **440**, 389–394.

Landivar, J., Cothren, J. & Livingston, S. (1996), Development and evaluation of the average five internode length technique to determine time of mepiquat chloride application, *in* 'Proceedings of the Beltwide Cotton Conferences', Vol. 2, National Cotton Council, Memphis, Tennessee, pp. 1153–1156.

Lang, A. (1973), 'Leaf orientation of a cotton plant', *Agricultural Meteorology* **11**, 37–51.

Laptev, I., Mayer, H., Lindeberg, T., Eckstein, W., Steger, C. & Baumgartner, A. (2000), 'Automatic extraction of roads from aerial images based on scale space and snakes', *Machine Vision and Applications* **12**(1), 23–31.

Larmore, L. (1965), *Introduction to Photographic Principles*, 2nd edn, Dover Publications, Inc., New York.

Leinonen, I. & Jones, H. (2004), 'Combining thermal and visible imagery for estimating canopy temperature and identifying plant stress', *Journal of Experimental Botany* **55**(401), 1423–1431.

Lu, Z. & Neumann, P. (1999), 'Water stress inhibits hydraulic conductance and leaf growth in rice seedlings but not the transport of water via mercury-sensitive water channels in the root', *Plant Physiology* **120**, 143–151.

Magnus, J. R. & Neudecker, H. (1999), *Matrix Differential Calculus With Applications in Statistics and Econometrics*, 2nd edn, John Wiley & Sons.

McCarthy, A., Raine, S. & Hancock, N. (2008), Towards evaluation of adaptive control systems for improved site-specific irrigation of cotton, *in* 'Irrigation Australia National Conference', Melbourne.

McCarthy, C., Hancock, N. & Raine, S. (2007), On-the-go machine vision sensing of cotton plant geometric parameters: first results, *in* J. Billingsley & R. Bradbeer, eds, 'Mechatronics and Machine Vision in Practice', Springer.

McDonald, T. & Chen, Y. (1990), 'Application of morphological image processing in agriculture', *Transactions of the ASAE* **33**(4), 1345–1352.

McKenzie, D., ed. (1998), *SOILpak for cotton growers*, 3rd edn, NSW Agriculture.

Mery, D. & Filbert, D. (2002), 'Automated flaw detection in aluminum castings based on the tracking of potential defects in a radioscopic image sequence', *IEEE Transactions on Robotics and Automation* **18**(6), 890–901.

Meyer, G. (2008). Science Leader, Sensor Network Systems, CSIRO, *pers. comm.* 15 September.

Meyer, G., Hindman, T., Jones, D. & Mortensen, D. (2004), 'Digital camera operation and fuzzy logic classification of uniform plant, soil, and residue color images', *Transactions of the ASAE* **20**(4), 519–529.

Meyer, W. & Walker, S. (1981), 'Leaflet orientation in water-stressed soybeans', *Agronomy Journal* **73**(6), 1071–1074.

Milroy, S., Goyne, P. & Larsen, D. (2002), Cotton information sheet: irrigation scheduling of cotton, Technical report, Australian Cotton Cooperative Research Centre.

Moriana, A. & Fereres, E. (2002), 'Plant indicators for scheduling irrigation of young olive trees', *Irrigation Science* **21**(2), 83–90.

Murase, H., Nishiura, Y. & Mitani, K. (1997), 'Environmental control strategies based on plant responses using intelligent machine vision technique', *Computers and Electronics in Agriculture* **18**(2), 137–148.

Nelson, A. (2000), Implementation of image processing algorithms on FPGA hardware, Electrical engineering, Vanderbilt University. Master's thesis.

Neto, J., Meyer, G. & Jones, D. (2006), 'Individual leaf extractions from young canopy images using Gustafson-Kessel clustering and a genetic algorithm', *Computers and Electronics in Agriculture* **51**(1–2), 68–85.

Neto, J., Meyer, G., Jones, D. & Samal, A. (2006), 'Plant species identification using Elliptic Fourier leaf shape analysis', *Computers and Electronics in Agriculture* **50**(2), 121–134.

Nobis, M. & Hunziker, U. (2005), 'Automatic thresholding for hemispherical canopy-photographs based on edge-detection', *Agricultural and Forest Meteorology* **128**(2), 243–250.

Noh, H., Zhang, Q., Han, S., Shin, B. & Reum, D. (2005), 'Dynamic calibration and image segmentation methods for multispectral imaging crop nitrogen deficiency sensors', *Transactions of the ASAE* **48**(1), 393–401.

Noordam, J., Hemming, J., van Heerde, C., Golbach, F., van Soest, R. & Wekking, E. (2005), Automated rose cutting in greenhouses with 3D vision and robotics: analysis of 3D vision techniques for stem detection, *in* van Straten et al. (2005).

Oosterhuis, D. (1990), Growth and development of a cotton plant, *in* 'Nitrogen Nutrition in Cotton: Practical Issues', Cooperative Extension Service, University of Arkansas.

Pan, Z., Hu, W., Guo, X. & Zhao, C. (2004), An efficient image-based 3D reconstruction algorithm for plants, *in* 'The 2004 International Conference on Computational Science and its Applications', Assisi, Italy, pp. 751–760.

Papari, G. & Petkov, N. (2005), 'Algorithm that mimics human perceptual grouping of dot patterns', *Lecture Notes in Computer Science* **3704**, 497–506.

Perry, C. & Pocknee, S. (2004), 'Precision irrigation controls to optimize water application', *International Water & Irrigation* **24**(3), 20–23.

Peters, R. & Evett, S. (2004), 'Modeling diurnal canopy temperature dynamics using one-time-of-day measurements and a reference temperature curve', *Agronomy Journal* **96**, 1553–1561.

Praat, J., Bollen, F. & Irie, K. (2004), New approaches to the management of vineyard variability in New Zealand, *in* 'The 12th Australian Wine Industry Technical Conference, Managing Vineyard Variation (Precision Viticulture)', Australian Wine Industry, Melbourne, pp. 24–30.

Prenger, J., Ling, P., Hansen, R. & Keener, H. (2005), 'Plant response-based irrigation control system in a greenhouse: system evaluation', *Transactions of the ASAE* **48**(3), 1175–1183.

Preparata, F. P. & Shamos, M. I. (1985), *Computational Geometry: An Introduction*, Springer.

Quan, L., Tan, P., Zeng, G., Yuan, L., Wang, J. & Kang, S. (2006), 'Image-based plant modeling', *ACM Transactions on Graphics* **25**(3), 599–604.

Raine, S. & Foley, J. (2002), 'Comparing systems for cotton irrigation', *The Australian Cottongrower* **23**(4), 30–35.

Room, P. & Hanan, J. (1995), Virtual cotton: a new tool for research, management and training, *in* 'Challenging the Future: Proceedings of the World Cotton Research Conference I', CSIRO, Melbourne, pp. 40–44.

Rovira-Mas, F., Zhang, Q. & Reid, J. (2005), 'Creation of three-dimensional crop maps based on aerial stereoimages', *Biosystems Engineering* **90**(3), 251–259.

Sadler, E., Bauer, P., Busscher, W. & Millen (2000b), 'Site-specific analysis of a droughted corn crop: II. Water use and stress', *Agronomy Journal* **92**, 403–410.

Sadler, E., Camp, C., Evans, D. & Millen, J. (2002), 'Corn canopy temperatures measured with a moving infrared thermometer array', *Transactions of the ASAE* **45**(3), 581–591.

Sadler, E., Camp, C., Evans, D. & Usrey, L. (1997a), A site-specific irrigation system for the southeastern USA coastal plain, *in* Evans et al. (1997a), pp. 337–344.

Sadler, E., Evans, R., Buchleiter, G., King, B. & Camp, C. (2000a), Design considerations for site-specific irrigation, *in* 'Proceedings of the 4th Decennial National Irrigation Symposium', Phoenix, Arizona, pp. 304–315.

Sato, Y., Nakajima, S., Atsumi, H., Koller, T., Gerig, G., Yoshida, S. & Kikinis, R. (1997), '3D multi-scale line filter for segmentation and visualization of curvilinear structures in medical images', *Lecture Notes in Computer Science* **1205**, 213–222.

Schumann, A. & Zaman, Q. (2005), 'Software development for real-time ultrasonic mapping of tree canopy size', *Computers and Electronics in Agriculture* **45**(1), 25–40.

Seginer, I., Elster, R., Goodrum, J. & Reiger, M. (1992), 'Plant wilt detection by computer-vision tracking of leaf tips', *Transactions of the ASAE* **35**(5), 1563–1567.

Serra, J. (1982), *Image Analysis and Mathematical Morphology*, Academic Press, London.

Sezgin, M. & Sankur, B. (2004), 'Survey over image thresholding techniques and quantitative performance evaluation', *Journal of Electronic Imaging* **13**(1), 146–165.

Shearer, S. & Holmes, R. (1990), 'Plant identification using color co-occurrence matrices', *Transactions of the ASAE* **33**(6), 2037–2044.

Shimizu, H. & Heins, R. (1995), 'Computer-vision-based system for plant growth analysis', *Transactions of the ASAE* **38**(3), 959–964.

Shiraishi, M. & Sumiya, H. (1996), 'Plant identification from leaves using quasi-sensor fusion', *Transactions of the ASME* **118**(3), 382–387.

Shrestha, D. & Steward, B. (2003), 'Automatic corn plant population measurement using machine vision', *Transactions of the ASAE* **46**(2), 559–565.

Shrestha, D. & Steward, B. (2005), 'Shape and size analysis of corn plant canopies for plant population and spacing sensing', *Applied Engineering in Agriculture* **21**(2), 295–303.

Simonton, W. (1990), 'Automatic geranium stock processing in a robotic workcell', *Transactions of the ASAE* **33**(6), 2074–2080.

Singh, S. & Montemerlo, M. (1997), Recent results in the grading of vegetative cuttings using computer vision, *in* 'Proceedings of the IEEE-RSJ International Conference on Intelligent Robots and Systems Innovative Robots for Real-World Applications'.

Smith, R., Raine, S., McCarthy, A. & Hancock, N. (2007), Managing spatial and temporal variability in irrigated agriculture through adaptive control, *in* 'Challenge Today, Technology Tomorrow', Society Engineering in Agriculture National Conference, Adelaide.

Stabile, M. (2005), Site-specific strategies for cotton management, Master's thesis, Texas A & M University.

Steger, C. (1996), 'Extracting curvilinear structures: a differential geometric approach', *Lecture Notes in Computer Science* **1064**, 630–641.

Steward, B., Tian, L., Nettleton, D. & Tang, L. (2004), 'Reduced-dimension clustering for vegetation segmentation', *Transactions of the ASAE* **47**(2), 609–616.

Tagzout, S., Achour, K. & Djekoune, O. (2001), Hough transform algorithm for FPGA implementation, *in* 'IEEE Workshop on Signal Processing Systems', pp. 384–393.

Takakura, T., Shimomachi, T. & Takemasa, T. (2002), Non-destructive detection of plant health, Acta Horticulturae 578, International Society for Horticultural Science, pp. 303–306.

Takizawa, H., Ezaki, N. & Mizuno, S. (2005), Measurement of plants by stereo vision for agricultural applications, *in* 'Proceedings of the Seventh IASTED Internal Conference: Signal and Image Processing'.

Tang, L., Tian, L. & Steward, B. (2000), 'Color image segmentation with genetic algorithm for in-field weed sensing', *Transactions of the ASAE* **43**(4), 1019–1027.

Tang, L., Tian, L. & Steward, B. (2003), 'Classification of broadleaf and grass weeds using Gabor wavelets and an artificial neural network', *Transactions of the ASAE* **46**(4), 1247–1254.

Tarbell, K. & Reid, J. (1991), 'A computer vision system for characterizing corn growth and development', *Transactions of the ASAE* **34**(5), 2245–2255.

Teague, T., Vories, E., Tugwell, N. & Danforth, D. (1999), Using the COTMAN system for early detection of stress: Triggering irrigation based on square retention and

crop growth, *in* 'Proceedings of the 1999 Cotton Research Meeting and Summaries of Cotton Research in Progress', University of Arkansas Agricultural Experiment Station, Fayetteville, Arkansas, pp. 46–55.

Theis, M., Pfeifer, N., Winterhalder, D. & Gorte, B. (2004), 'Three-dimensional reconstruction of stems for assessment of taper, sweep and lean based on laser scanning of standing trees', *Scandinavian Journal of Forest Research* **19**(6), 571–581.

Tian, L. & Slaughter, D. (1998), 'Environmentally adaptive segmentation algorithm for outdoor image segmentation', *Computers and Electronics in Agriculture* **21**, 153–168.

Tumbo, S., Salyani, M., Whitney, J., Wheaton, T. & Miller, W. (2002), 'Investigation of laser and ultrasonic ranging sensors for measurements of citrus canopy volume', *Applied Engineering in Agriculture* **18**(3), 367–372.

University of Arkansas Division of Agriculture (2005), *COTMAN*, Fayetteville, Arkansas. Viewed 12 March 2005, `http://www.uark.edu/depts/cotman/`.

van Henten, E. & Bontsema, J. (1995), 'Non-destructive crop measurements by image processing for crop growth control', *Journal of Agricultural Engineering Research* **61**, 97–105.

van Henten, E., Hemming, J., van Tuijl, B., Kornet, J., Meuleman, J., Bontsema, J. & van Os, E. (2002), 'An autonomous robot for harvesting cucumbers in greenhouses', *Autonomous Robots* **13**(3), 241–258.

van Straten, G., Bot, G., van Meurs, W. & Marcelis, L., eds (2005), *Proceedings of the International Conference on Sustainable Greenhouse Systems*, Acta Horticulturae 691, International Society for Horticultural Science.

Vrindts, E. & de Baerdemaeker, J. (1997), Optical discrimination of crop, weed and soil for on-line weed detection, *in* J. Stafford, ed., 'Precision Agriculture 1997, Volume II: Technology, IT and Management', BIOS Scientific Publishers Limited, Oxford, pp. 533–544.

Waksman, A. & Rosenfeld, A. (1997), 'Assessing the condition of a plant', *Machine Vision and Applications* **10**(1), 35–41.

Wang, N., Zhang, N., Dowell, F., Sun, Y. & Peterson, D. (2001), 'Design of an optical weed sensor using plant spectral characteristics', *Transactions of the ASAE* **44**(2), 409–419.

Wang, Z., Heinemann, P., Sommer III, H., Walker, P., Morrow, C. & Heuser, C. (1998), 'Identification and separation of micropropagated sugarcane shoots based on the Hough transform', *Transactions of the ASAE* **98**, 4105–1535.

Wei, J. & Salyani, M. (2004), 'Development of a laser scanner for measuring tree canopy characteristics: Phase 1. Prototype development', *Transactions of the ASAE* **47**(6), 2101–2107.

Wilhoit, J., Kutz, L., Fly, D. & South, D. (1994), 'PC-based multiple camera machine vision systems for pine seedling measurements', *Transactions of the ASAE* **10**(6), 841–847.

Williams, L. & Ayars, J. (2005), 'Grapevine water use and the crop coefficient are linear functions of the shaded area measured beneath the canopy', *Agricultural and Forest Meteorology* **132**, 201–211.

Woebbecke, D., Meyer, G., Von Bargen, K. & Mortensen, D. (1995), 'Color indices for weed identification under various soil, residue, and lighting conditions', *Transactions of the ASAE* **38**(1), 259–269.

Yatapanage, K. & So, H. (2001), 'The relationship between leaf water potential and stem diameter in sorghum', *Agronomy Journal* **93**(6), 1341–1343.

Zeng, G., Birchfield, S. & Wells, C. (2006), 'Detecting and measuring fine roots in minirhizotron images using matched filtering and local entropy thresholding', *Machine Vision and Applications* **17**, 265–278.

Zhang, J., Sokhansanj, S., Wu, S., Fang, R., Yang, W. & Winter, P. (1998), 'A transformation technique from RGB signals to the Munsell system for color analysis of tobacco leaves', *Transactions of the ASAE* **19**, 155–166.

Zhang, N., Wang, M. & Wang, N. (2002), 'Precision agriculture – a worldwide overview', *Computers and Electronics in Agriculture* **36**(2–3), 113–132.

# Appendix A

# Glossary

The following terms are relevant to plant stress and cotton growth and development, followed by a generic diagram of cotton plant structure (Figure A.1).

**Allometry.** The study of the change in proportions of parts of an organism as a result of growth.

**Biomass.** The total mass of living matter in a given unit volume of environmental area.

**Boll.** *Cotton:* The name given to cotton's fruit.

**Cutout.** *Cotton:* The end of vegetative growth that generally coincides with nodes above white flower (NAWF) equal to five or six; plant then focuses on boll development.

**Dendrometer.** An instrument to measure tree diameter.

**Growth rate.** Change in height with respect to change in number of main stem nodes.

**Heat units.** *Cotton:* Also day-degrees or DD; a cumulative linear function of daily minimum and maximum temperatures used to express cotton's development (starting at planting) in terms of temperature; significant because cotton's development is strongly influenced by temperature.

**Heliotropism.** The adjustment of leaf angle and leaf azimuth to the changes in the position of the solar beam (Meyer & Walker, 1981). *Paraheliotropism* indicates leaf movement to minimise sunlight interception while *diaheliotropism* indicates leaf movement to maximise sunlight interception (Das, 2004).

**Internode length.** Distance between successive nodes on a branch or stem. Agronomists use the distance between the fourth and fifth nodes as an indicator of water stress. If the fourth-to-fifth internode length is greater than approximately 70 mm the plant is exhibiting too much vegetative growth.

**Leaf area index (LAI).** The ratio of the total one-sided green leaf area per unit ground surface area; defines the area that interacts with solar radiation.

**Leaf water potential.** A measure in megaPascals (MPa) of the amount of tension a leaf is applying on its water content, with more negative tensions indicating higher stress.

**Lint.** *Cotton:* Cotton fibres.

**Node.** Position at which a branch or leaf develops on the main stem.

**Nodes above white flower (NAWF).** *Cotton:* The number of main stem nodes above the highest first-position (closest to main stem) white flower. As vegetative growth decreases, flowering progresses up the plant and NAWF decreases, hence NAWF is an indicator of both vegetative and reproductive growth.

**Shedding.** *Cotton:* A process by which a cotton plant drops fruit; this may be a result of the plant adjusting its fruit load to match the quantity of resources available (susceptibility varies with fruit age), or the process may be the result of factors such as insect damage.

**Square.** *Cotton:* A fruiting bud.

**Target development curve.** The desired value of a particular crop attribute plotted throughout the crop's growth. A comparison of measured crop data and the target

development curve may be used to draw conclusions about the crop's performance and aid in management decisions.

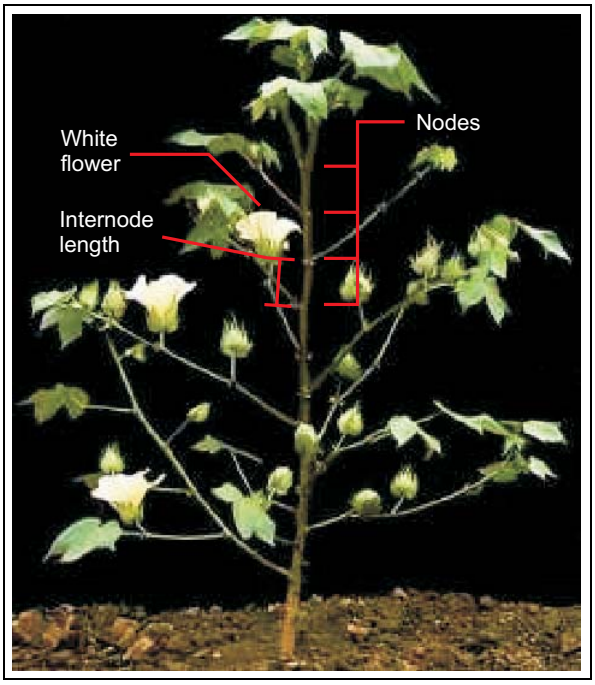


Figure A.1: A cotton plant with significant attributes labeled and partially defoliated for ease of visualising the branching structure. Each node on the main stem and on each branch would usually have a subtending leaf.

# Appendix B

# Field apparatus implementation details

This appendix comprises the sections listed below.

**Appendix B.1** lists component values for the circuit implementation of the LED illumination of camera enclosure Mark 4 (Section 3.5.2).

**Appendix B.2** contains overall dimensions of the automated infield chassis (Section 3.8).

**Appendix B.3** illustrates the mechanical implementation of the translational and rotational degrees of freedom for the automated infield chassis (Section 3.8).

**Appendix B.4** contains a schematic circuit diagram for motor control on the automatic infield chassis (Section 3.8.2).

## B.1 LED illumination for camera enclosure Mark 4

The circuit diagram for the LED illumination is in Figure B.1(a), where the blocks denoted 'top' and 'bottom' refer to the two separate LED arrays on the top and bottom horizontal edges of the camera enclosure window, respectively. The circuit diagram in Figure B.1(b) represents the connections required for each group of three LEDs in an array. Six such circuits were required to be connected in parallel to generate an array of 18 LEDs. Table B.1 displays the component values for the white, 850 nm and 940 nm LEDs, as well as a reference website for supply of the LEDs.

Only one type of LED circuit was activated at a time for standard operation of the camera enclosure (via power switches SW1–SW3, which feature in Figure 3.6(b)).

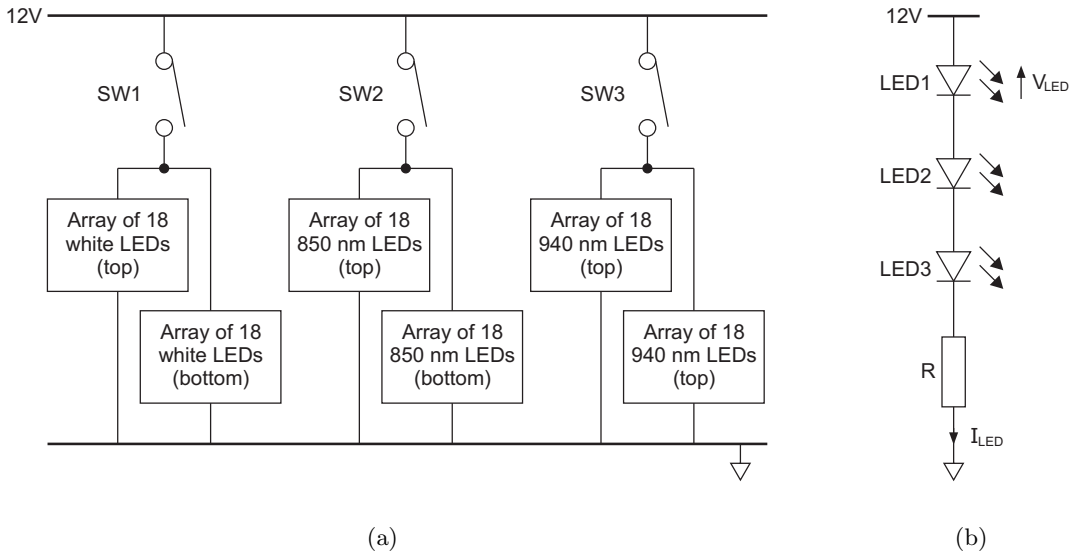


Figure B.1: Schematic electrical circuit for LED illumination: (a) connections for all three types of LEDs; and (b) part of an individual LED array.

Table B.1: Electronic component values for LED arrays.

| LED type | $V_{LED}$ (V) | $I_{LED}$ (mA) | R (Ω) | LED specifications | Supplier |
|---|---|---|---|---|---|
| White | 3 | 50 | 60 | 5 mm, 20°, 12000 mcd | www.goodwillsales.com |
| 850 nm | 2 | 100 | 60 | 5 mm, 14° | www.allthings.com.au |
| 940 nm | 2 | 100 | 60 | 5 mm, 20° | www.allthings.com.au |

## B.2 Overall dimensions of automated infield chassis

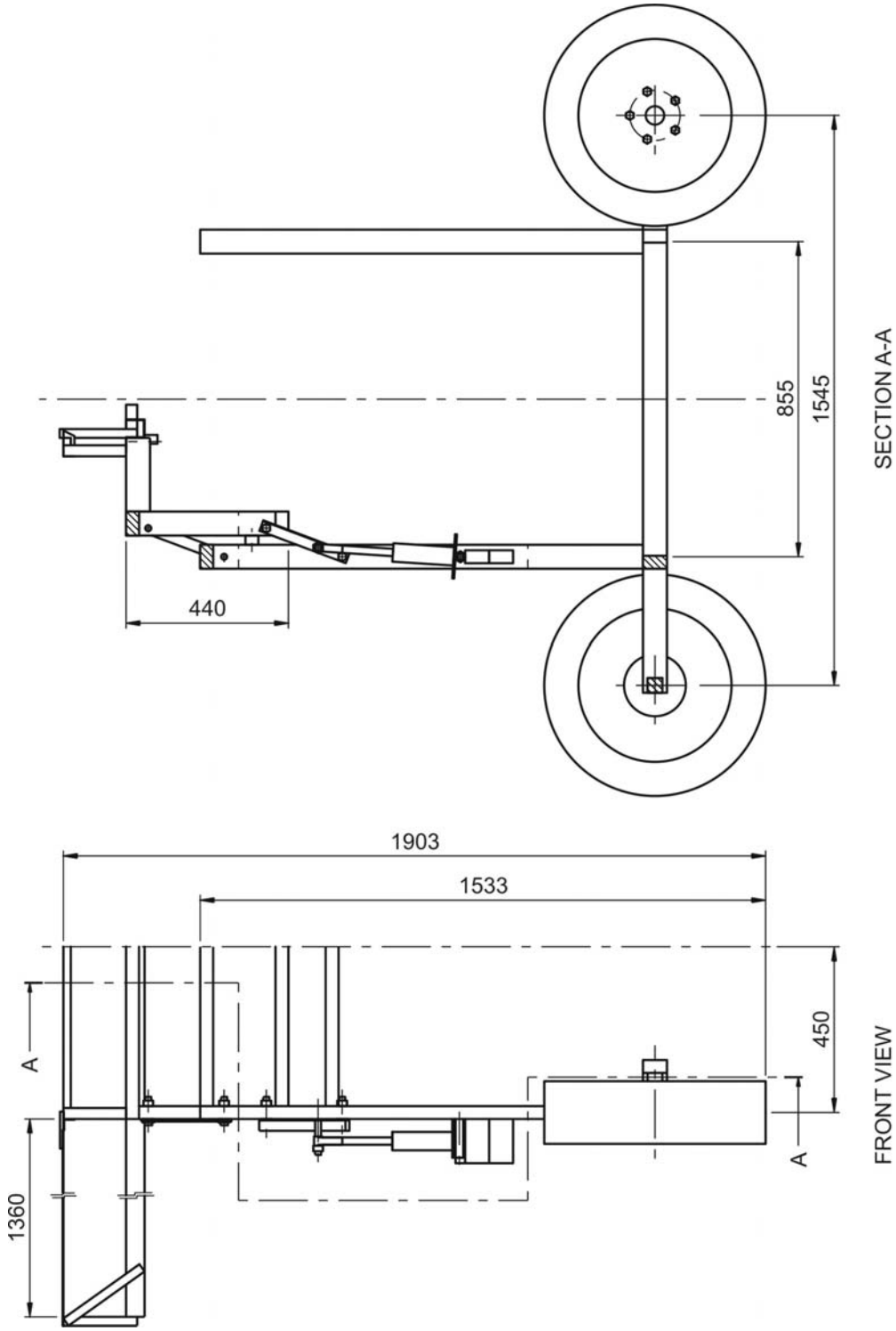


Figure B.2: Schematic diagram of automated infield chassis, with overall dimensions (in mm).

## B.3 Overall dimensions of quad-axis drive system for automated infield chassis

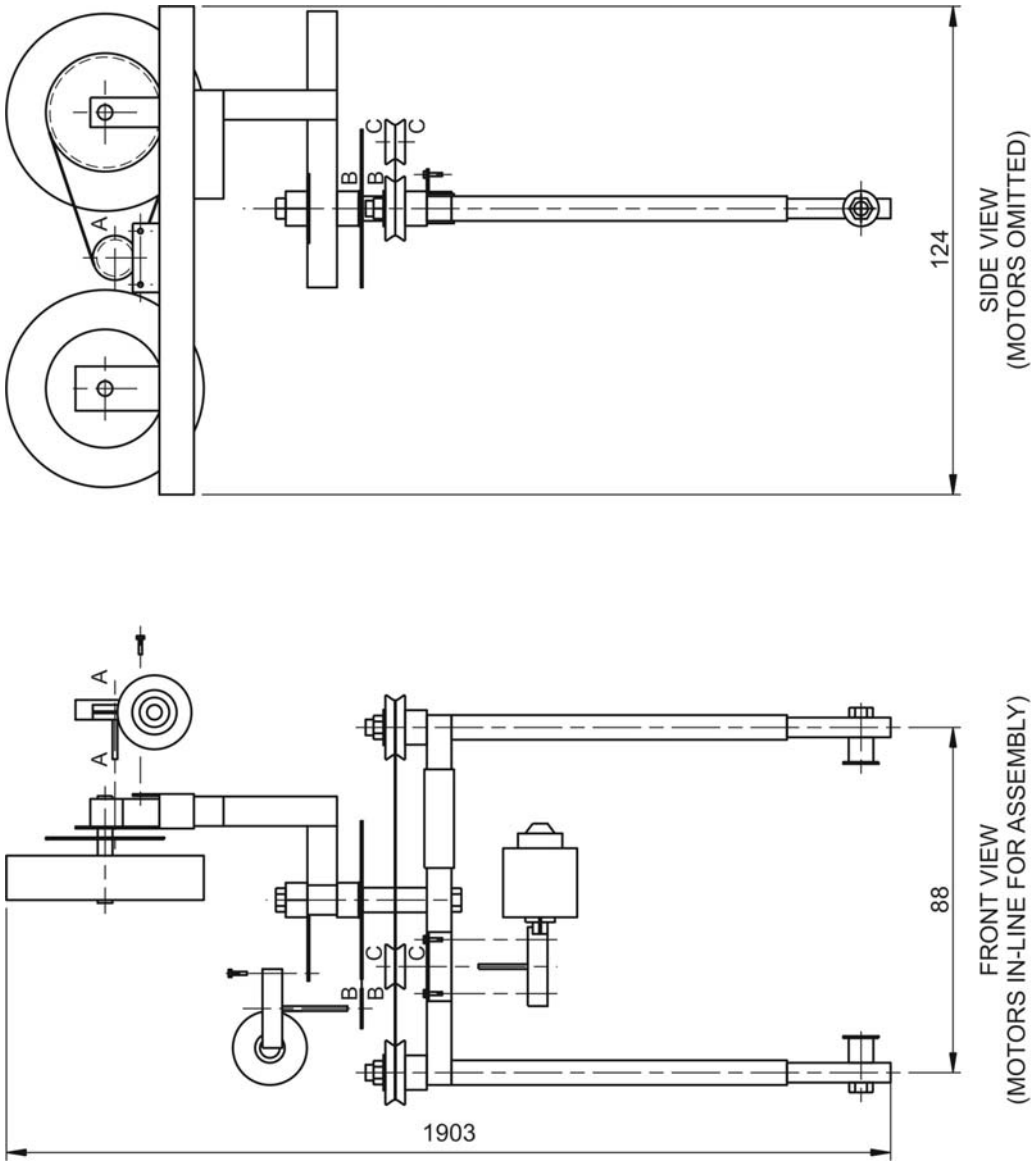


Figure B.3: Schematic diagram of quad-axis drive system, with overall dimensions (in mm).

## B.4 Motor control circuit for camera enclosure conveyance

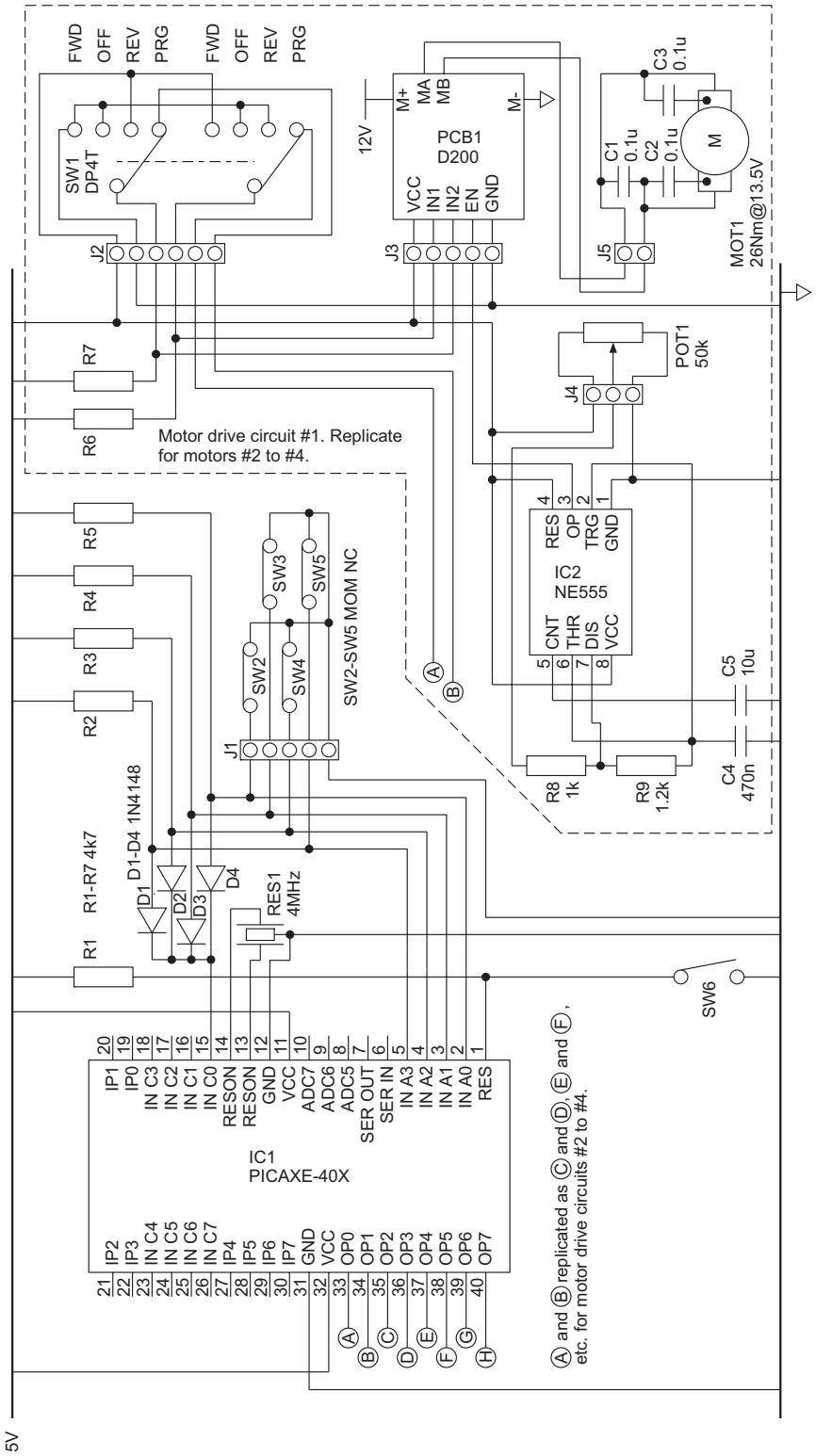


Figure B.4: Schematic diagram of motor control circuit. D200 (PCB1) is a low-cost H-bridge motor driver rated at 12V 60A with appropriate heat sinks, available from www.tecel.com.

# Appendix C

# Spectral differences in plant materials

A preliminary investigation of plant spectral properties was conducted to determine the potential for discriminating stems and other cotton plant foliage based on narrowband spectral differences. This approach was not pursued as discussed in Section 4.6.1, but the spectral responses are included here for reference.

Stems and fruit have a higher moisture content than leaves, and as such exhibit a lower reflectance in the water absorption wavelengths around 970 nm (Figure C.1). Hyperspectral data (Figure C.2) was collected at the cotton field site using an ASD FieldSpec Handheld Spectrometer (www.asdi.com) for 30 samples each of big and small bolls, flowers, leaves and stems. By comparison with the results in Figure C.1, cotton stems and bolls exhibit characteristic stem and fruit curves including the water absorption band at 970 nm (however some cotton plant stems had a red tinge which is evident in the graph). The near infrared reflectance properties of the cotton plant materials potentially enable a differential two-waveband vision system (850 and 970 nm, for example) to differentiate stems and leaves.

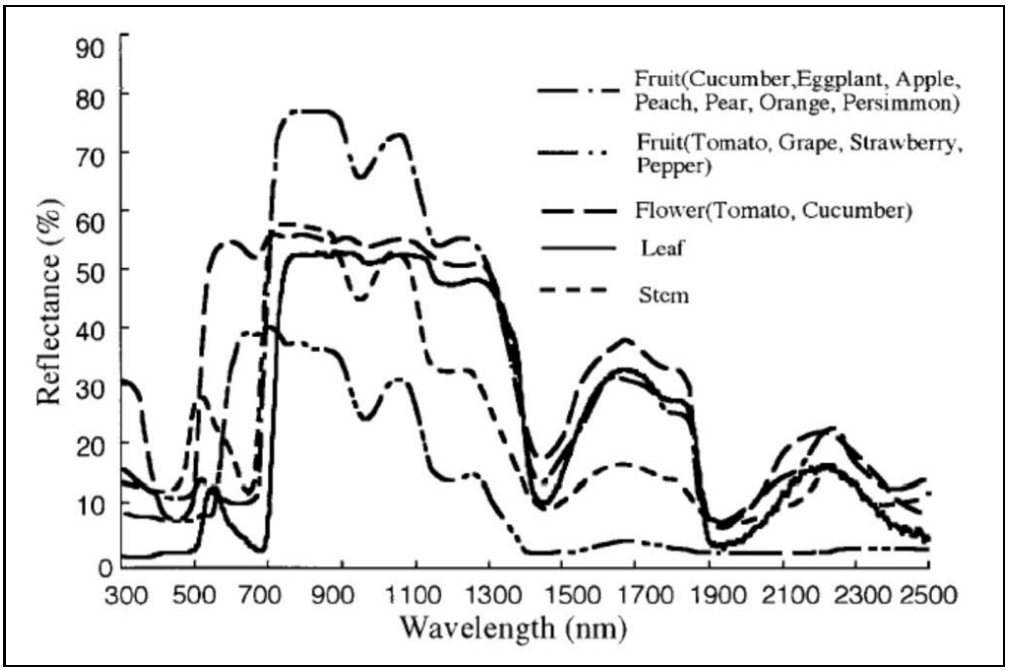


Figure C.1: Spectral response (300–2500 nm) of plant materials. Source: Kondo & Ting (1998).

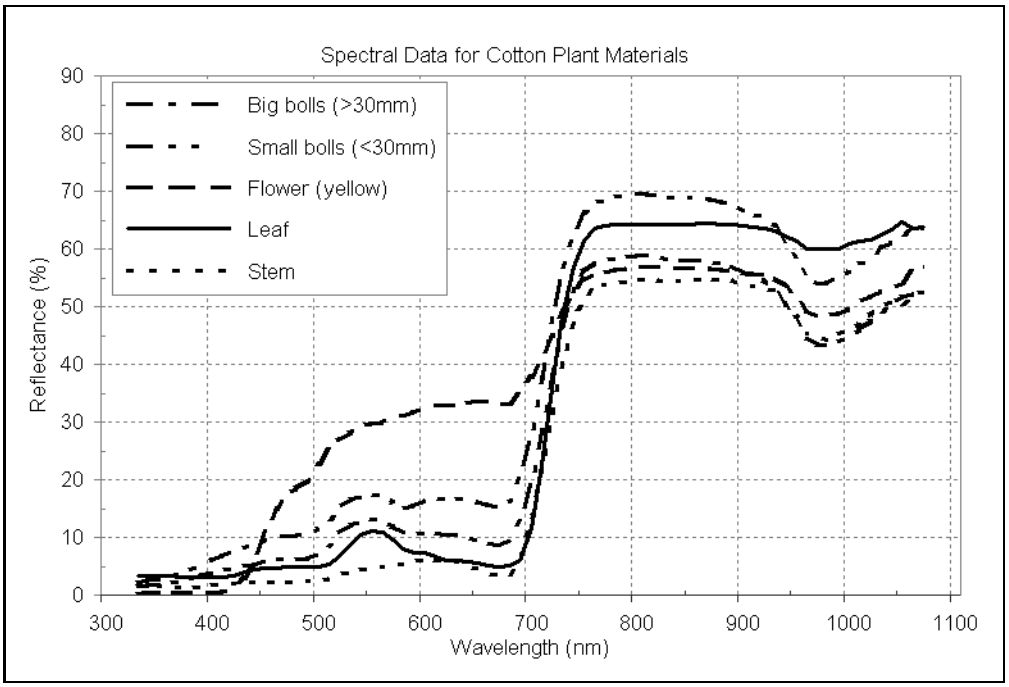


Figure C.2: Spectral response (325–1075 nm) of cotton plant materials.

# Appendix D

# Algorithm details

This appendix contains details of edge detection algorithms evaluated for the task of node detection and pseudocode listings for processes in the developed algorithm.

**Appendix D.1** describes the Sobel, adaptive thresholding and Canny methods of edge detection that were evaluated in Section 4.7.

**Appendix D.2** contains excerpt pseudocode listings for the automatic node and node trajectory detection algorithms. Appendix D.2.1 describes the process that selectively projects line segments to the identified main stem to contribute a candidate node position (Section 4.11.4) and Appendix D.2.2 describes the process that identifies adjacent regions of detected node trajectories to enable calculation of internode distances (Section 5.5).

## D.1 Edge detection algorithms

### D.1.1 Sobel edge operator

The Sobel edge operator is the magnitude of the gradient of a pixel. The horizontal and vertical convolution masks that calculate the pixel's horizontal and vertical gradients ($s_x$ and $s_y$, respectively) from a $3 \times 3$ neighbourhood centred on the pixel are:

$$s_x = \begin{bmatrix} -1 & 0 & 1 \\ -2 & 0 & 2 \\ -1 & 0 & 1 \end{bmatrix} \quad \text{and} \quad s_y = \begin{bmatrix} 1 & 2 & 1 \\ 0 & 0 & 0 \\ -1 & -2 & -1 \end{bmatrix} \tag{D.1}$$

### D.1.2 Edges by adaptive thresholding

Adaptive thresholding flags a pixel as a non-background pixel (i.e an edge pixel) if the pixel's intensity is greater than the average intensity of the pixel's $n \times n$ neighbourhood (where $n$ is a positive integer).

### D.1.3 Canny edge detection

An outline of the algorithm for Canny edge detection is as follows (from Jain et al. (1995)):

1. Smooth the image with a Gaussian filter of window size $w$.
2. Compute the gradient magnitude and orientation using finite-difference approximations for the partial derivatives.
3. Apply nonmaxima suppression to the gradient magnitude.
4. Use the double thresholding algorithm (denote thresholds as $t_{low}$ and $t_{high}$) to detect and link edges.

## D.2 Pseudocode for processes in the node and node trajectory detection algorithms

### D.2.1 Filtering the lines that are used to obtain candidate nodes

In the following pseudocode, lines detected from the hop-along algorithm are filtered to determine which lines will be used to form candidate node positions (Section 4.11.4). The line's start and end points, length and orientation are stored in memory and are used for evaluating the criteria listed below. 'Discard' is implemented simply as an array which contains a flag for each detected line indicating whether the line has failed any of the criteria tested.

```
for all line segments that have not been discarded
    // keep only long lines
    if current line does not exceed a length threshold then
        discard current line
        go to next line segment
    end if

    // remove extra lines that are obviously part of the same branch
    if angle between current line and previous line is less than a
    threshold, and the lines have an end point in common then
        discard top-most line
        if top-most line is current line then
            go to next line segment
        end if
    end if

    // remove lines that are possibly responses to the main stem
    if angle between current line and main stem is less than a
    threshold then
```

```
    discard current line
    go to next line segment
end if

// remove lines that cross over the main stem
if both ends of the current line extend beyond a threshold distance
on either side of the main stem then
    discard current line
    go to next line segment
end if

// only keep lines that form an acute angle when intersected with
// the main stem
if bottom end of current line is further from the main stem than
the top end of the current line then
    discard current line
    go to next line segment
end if

// project the line to the main stem to obtain candidate node
find the simultaneous solution to the current line and the main
stem

// remove lines that form candidate nodes outside the image area
if the solution lies outside the image area then
    discard current line
    go to next line segment
end if

// remove lines that need to be projected a long distance to the
// main stem
```

```
    if the distance between the solution and the current line end point
    exceeds a threshold then
        discard current line
        go to next line segment
    end if

    // save the candidate node position, it passes all the tests
    store solution
next
```

### D.2.2 Identifying successive trajectories from smoothed node positions

Following the grouping of candidate node positions into node trajectories, each group of nodes was smoothed into a single y-coordinate for each frame number. Regions of common frames between adjacent node trajectories were required to be identified from this information.

A pair of node positions occurring in the same frame and belonging to adjacent trajectories are represented as trapeziums in which the left edge of the trapezium corresponds to the first frame (and node y-coordinates) in which the pair of adjacent nodes were detected, and the right edge of the trapezium corresponds to the last frame (and node y-coordinates) in which the pair of adjacent nodes were detected (Section 5.5). The maximum and final heights of the trapezium are updated whenever the right edge of the trapezium is updated.

The following pseudocode achieves the task of returning the frame numbers and node y-coordinates of successive node trajectories.

```
// group a sequence of vertically-aligned candidate node positions into
// trapeziums (or regions of overlap between adjacent trajectories)
for all frame numbers from start of sequence to end
```

```
    for all pixel y-coordinates from top of image to bottom
        if a node position is found then
            store point
            increment y-coordinate until another node position is found
            if another node position is found then
                for all adjacent trajectories already detected
                    if end points of already detected adjacent
                    trajectories align with current pair of node
                    positions then
                        set the current pair of node positions to be
                        the new end points of the already detected
                        adjacent trajectories
                    end if
                next
                if no aligned adjacent trajectories were found then
                    set the current pair of node positions to be a new
                    adjacent trajectory
                end if
            end if
        end if
    next
next

// remove thin trapeziums (adjacent trajectories that only span a
// small number of frames)
for all trapeziums
    if width of trapezium is less than a threshold then
        discard trapezium
    end if
next
```

```
// remove trapeziums that correspond to adjacent trajectories that are
// already represented
for all trapeziums that have not been discarded
    for all other trapeziums that have not been discarded
        if the current trapezium shares a vertical edge with another
        trapezium then
            discard the taller trapezium
        end if
    next
    // remove adjacent trajectories that only occur at the end of the
    // sequence
    if the trapezium is located within a threshold number of frames
    of the end of the sequence then
        discard trapezium
    end if
next
sort trapeziums in order of ascending minimum y-coordinate

// now need to find a series of vertically-aligned trapeziums since
// some horizontally-displaced trapeziums may have been detected,
// i.e. group series of detected internode positions that occur within
// a specified number of frames of each other
for all trapeziums that have not been discarded
    for all trapezium groups already assigned
        if current trapezium is aligned vertically with trapezium
        group then
            add current trapezium to trapezium group
        end if
        if no aligned trapezium groups were found then
             set the current trapezium to be part of a new trapezium
             group
```

```
        end if
    next
next

// use left-most trapezium group (earliest occurring series of
// adjacent node trajectories) to calculate internode lengths
use the maximum heights of the trapeziums in the left-most trapezium
group for internode length calculations
```